Multi-scale Structure Analyses of Magnetopause Kelvin-Helmholtz Waves: Applications of Four-spacecraft to MHD Simulations and Cluster and MMS Observations

Submitted by Rungployphan Kieokaew to the University of Exeter
as a thesis for the degree of
Doctor of Philosophy in Mathematics
In February 2019

I certify that all material in this thesis which is not my own work has been identified and that no material has previously been submitted and approved for the award of a degree by this or any other University.

Signature: .....

Abstract

Magnetopause Kelvin-Helmholtz (KH) waves involve complex magnetic and flow structures that facilitate solar wind plasma transport. These plasma structures are resolved in 3-D with four-spacecraft forming a tetrahedral configuration.

This thesis considers applications of the Magnetic Curvature Analysis (MCA) and vorticity analysis techniques to characterise in-situ KH waves. The techniques are applied onto 2.5-D magnetohydrodynamics (MHD) simulations of the waves on the dusk-side magnetopause using the varying (regular) tetrahedron size of the virtual probes to interpret four-spacecraft observations with a certain tetrahedron size. The main results of this analysis are (1) the characterisation of the KH vortex regions using the magnetic curvature and flow vorticity and (2) the dependence of the four-spacecraft measures on the spacecraft tetrahedron size. In particular, the negative vorticity, developed next to the positive vorticity of the vortex core, on the dusk-side magnetopause pertains to rolled-up vortex and reminisces of rolled-up vortex history. The dependence of the MCA properties on the tetrahedron size can be attributed to non-linear spatial variations of the magnetic structures that could be resolved by nested spacecraft tetrahedrons. Cluster and MMS are the four-spacecraft missions that are probing the Earth's magnetospheric environments in multi-scales. Both results are confirmed using Cluster observations, though other properties that can be linked to the excitation of the KH instability and non-linear KH development are also deduced. Applications of the techniques on small-scale structures observed by MMS are illustrated during KH events, featuring mid-latitude reconnection, a Flux Transfer Event, and a magnetic island.

This thesis contributes to our understanding of multi-scale structures of the magnetopause KH waves that could shed light on how KH-associated mechanisms operate to allow solar wind plasma entries. For a comprehensive understanding of the KH phenomenon, a cross-scale coverage of KH observations would be desirable.

Acknowledgements

My PhD has brought challenges, yet it has been valuable years in my life where I explored, experimented, and succeeded. This journey could not happen without those who saw my potential and gave me the opportunity. I am grateful for the financial support from the College of Engineering, Mathematics, and Physical Sciences (CEMPS) at the University of Exeter. I cannot thank enough my supervisor, Dr Claire Foullon, for her constant encouragement and ambition to push me through the journey. I immensely appreciate her knowledge, mentorship, and efforts to go for an extra mile to help her student.

My visits to Institut de Recherche en Astrophysique et Planétologie (IRAP) at Université de Toulouse in 2016 and 2018 had been valuable times for me to get inputs and have fruitful discussions. I especially thank Dr Benoit Lavraud for hosting me and giving me constructive feedback, and Dr Yoann Vernisse for his numerical codes which greatly reduce my time in processing satellite data. I would also like to thank the CLweb team at IRAP, which provides satellite data and visualisation tools, that help me to proceed in the latter half of this thesis quickly.

I would like to thank Dr Tony Arber at the University of Warwick for numerical codes used in the first half of this study.

I would also like to thank my second supervisor, Prof Mitchell Berger, whom his presence has been welcoming, and my mentor, Dr Ana Rodrigues, who comforted me through hard times.

I am grateful for those I have met who led me to this journey. Prof David Ruffolo at Mahidol University has always been supportive since I met him while I was a high school student. I would especially like to thank Dr Kittipat Malakit for his academic mentorship and brotherly friendship. I would also like to thank Prof Michael Shay at the University of Delaware who gave me the opportunity to conduct a plasma physics research during my undergraduate years.

My family and friends have been a great source of my mental strength. My mother is the most resilient person I know, and she has been very supportive as much as she could. My father had grown seeds for the love of science (and adventures) in me since I was at a young age, though I wish he could live long enough to see how far his daughter has gone. This journey would have been much harder without my best friend, Chawisa Leekuakul, who has turned any misery into

laughs and smiles. I would like to thank my godmothers, Watcharakorn Junrut and Thitikul Kaewsuk, and my relatives who have been the extra supporters for my education. I would also like to thank my friends in Thailand, UK, and abroad, from the Faculty of Science at Mahidol University and from Princess Chulabhorn's College, Phitsanuloke, whom I reached out when I needed help.

I would like to thank friends I have met in Exeter. I would like to thank my girl team, Dr Katya Pyatkova, Dr Prarthana Gowda, and Dr Kimberly Bryan, whom I shared my Ph.D. journey with. I would also like to thank my office friends and GAFD people for being constantly supportive both inside and outside academia. I would like my past and current housemates, Dr Kulchamai Thienkaroachanakul and Dr Kunyapat Thummavichai, in particular, whom their presence has been reassuring and entertaining.

Last but not least, I acknowledge those who helped me through the journey. Your kindness did not go unnoticed and I very much appreciated.

Contents

List of Tables

List of Figures

Abbreviations

EBL	Electron Boundary Layer
FGM	Fluxgate Magnetometer
FPI	Fast Plasma Instrument
FTE	Flux Transfer Event
GS	Grad-Shafranov
GSE	Geocentric Solar Ecliptic coordinate system
GSM	Geocentric Solar Magnetospheric coordinate system
HRO	High Resolution OMNI
IMF	Interplanetary Magnetic Field
ISEE	International Sun-Earth Explorer
KH	Kelvin-Helmholtz
LDFTS	Lower Density and Faster Than Sheath
LLBL	Low-latitude Boundary Layer
MCA	Magnetic Curvature Analysis
MRA	Magnetic Rotation Analysis
MHD	Magnetohydrodynamics
MMS	Magnetospheric Multiscale mission
MPBL	Magnetopause Boundary Layer
MVA	Minimum Variance Analysis
PAD	Pitch Angle Distribution
THEMIS	Time History of Events and Macroscale Interactions during Substorms
TPE	Total Pressure Enhancement
ULF	Ultra Low Frequency
UT	Universal Time
VIR	Vortex Induced Reconnection

Part I

Introduction

Chapter 1

Introduction

This thesis focuses on applications of four-spacecraft techniques on the study of magnetopause Kelvin-Helmholtz (KH) waves. This introductory Chapter gives an overview of the solar wind interactions with the Earth's magnetosphere in Section 1.1. It then introduces the linear theory of the magnetic KH instability in Section 1.2 and magnetopause KH waves in Section 1.3. A brief introduction of the techniques for space plasma analyses is given in Section 1.4. Motivation and outline of the thesis are finally given in Section 1.5.

1.1 Solar Wind Interaction with Terrestrial Environments

The space beyond the Earth is not as empty as it seems. We live under the influence of the Sun that is constantly accelerating particles to high energies which stream out into the solar system and then affect the space environment. The Earth has a geomagnetic field that shields the terrestrial environment from space radiation. Nevertheless, solar wind energetic particles can enter the Earth's magnetic field, which then can affect human activities especially in this modern technological age. These solar wind entries can take place at the Earth's magnetospheric boundary that is formed between the shocked solar wind stream and the terrestrial magnetic field. The solar wind entries can have severe impact on society, disrupting our modern technologies such as power grids and Global Positioning Satellites (GPS). Understanding the physical mechanisms that take place on the Earth's magnetopause contributes to space weather predictions that would have wide socio-economic impacts.

Solar wind interaction with terrestrial space environments have long been postulated to explain observations of aurorae. Interest in this subject was led by two influential papers by *Dungey* [1961] and *Axford and Hines* [1961]. *Dungey* [1961] hypothesised a magnetic reconnection between the southward interplan-

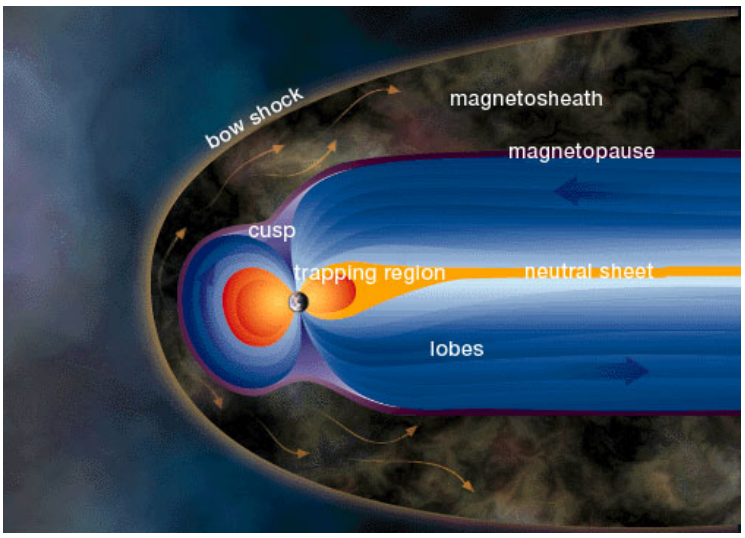

Figure 1.1.1: Schematic illustration of the Earth's magnetosphere under the influence of the solar wind. Image courtesy of ESA.

etary magnetic field (IMF) and the northward geomagnetic field on the dayside. Magnetic reconnection is a process where two oppositely directed magnetic fields in plasma environments rearrange their connections. The rearrangement consequently releases the stored magnetic field energy into acceleration and heating of plasma particles. This process allows the solar wind to enter to the Earth's outer atmosphere which could explain aurorae. *Axford and Hines* [1961] proposed a viscous-like interaction between the Earth's magnetic field and the solar wind. The viscous-like interaction can supply the source of convection (i.e., the motion of the terrestrial magnetic field lines) which can explain many geomagnetic phenomena. A form of viscous-like interaction was suggested to be Kelvin-Helmholtz (KH) instability, a classical shear-flow instability in hydrodynamic and magnetohydrodynamic (MHD) theories, on the flanks of the magnetosphere [*Axford*, 1964]. The dayside reconnection and viscous-like interaction are believed to be the two main drivers of the magnetospheric convection.

The magnetospheric boundary is where various physical mechanisms that allow solar wind entries take place. This magnetospheric boundary is called the ``magnetopause". The magnetopause separates between the shocked solar wind and the Earth's dipole magnetic field as shown in Figure 1.1.1. The location of the magnetopause is determined where the solar wind dynamic pressure and the terrestrial magnetic pressure balance. The shocked solar wind plasma forms a region called ``magnetosheath" that is between the bow shock and the magnetosphere as seen in Figure 1.1.1. At the bow shock, the supersonic solar wind speed abruptly decelerates to a subsonic speed. The magnetosheath plasma is generally dynamic and turbulent and is subject to the upstream solar wind conditions. The IMF is embedded in the solar wind and carried through with the magnetosheath plasma. Behind the magnetopause is a region called the ``magneto-

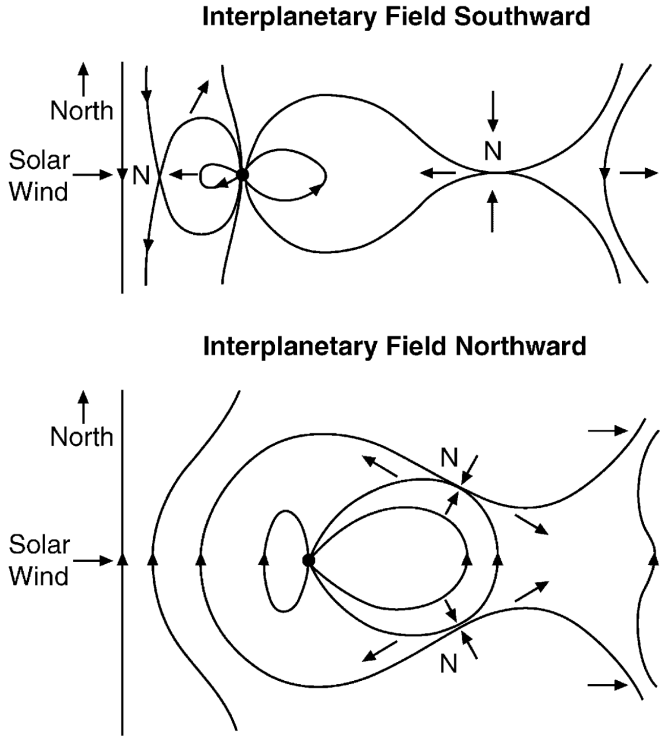

Figure 1.1.2: The Dungey reconnection model during southward IMF (top) and northward IMF (bottom) [*Dungey*, 1961, 1963]. Image courtesy of *Russell* [2001].

sphere" and is dominated by the geomagnetic field (blue region in Figure 1.1.1). The magnetosheath plasma has its most direct access in the `cusp' where the magnetospheric boundary extends deep towards the north and south geomagnetic poles. The stand-off distance of the magnetopause on the dayside is around ten earth radii (R_E). On the nightside, the magnetic field in the magnetosphere extends very far beyond the Earth. This region is called ``magnetotail". The magnetotail contains the neutral sheet that separates the northern lobe and the southern lobe. The magnetospheric boundary is a key region that controls mass, momentum, and energy transfer from the solar wind into the magnetosphere.

The solar wind conditions determine the global structure of the magnetosphere. As suggested by *Dungey* [1961], the magnetopause can be open or closed depending on the IMF orientation as shown in Figure 1.1.2. When the IMF is due south, magnetic reconnection can take place at the dayside and nightside (top panel of Figure 1.1.2). Major solar wind plasma transport is expected under southward IMF conditions. When the IMF is due north, magnetic reconnection can take place near the cusp (bottom panel of Figure 1.1.2), though no major solar wind plasma transport is expected in the model. Satellite observations have revealed more complex magnetopause structures. Adjacent to the magnetopause on the earthward side, there is a region called ``low-latitude boundary layer" (LLBL) where both magnetosheath and magnetospheric plasma populations are found [e.g., *Eastman et al.*, 1976; *Ogilvie et al.*, 1984]. Figure 1.1.3 shows

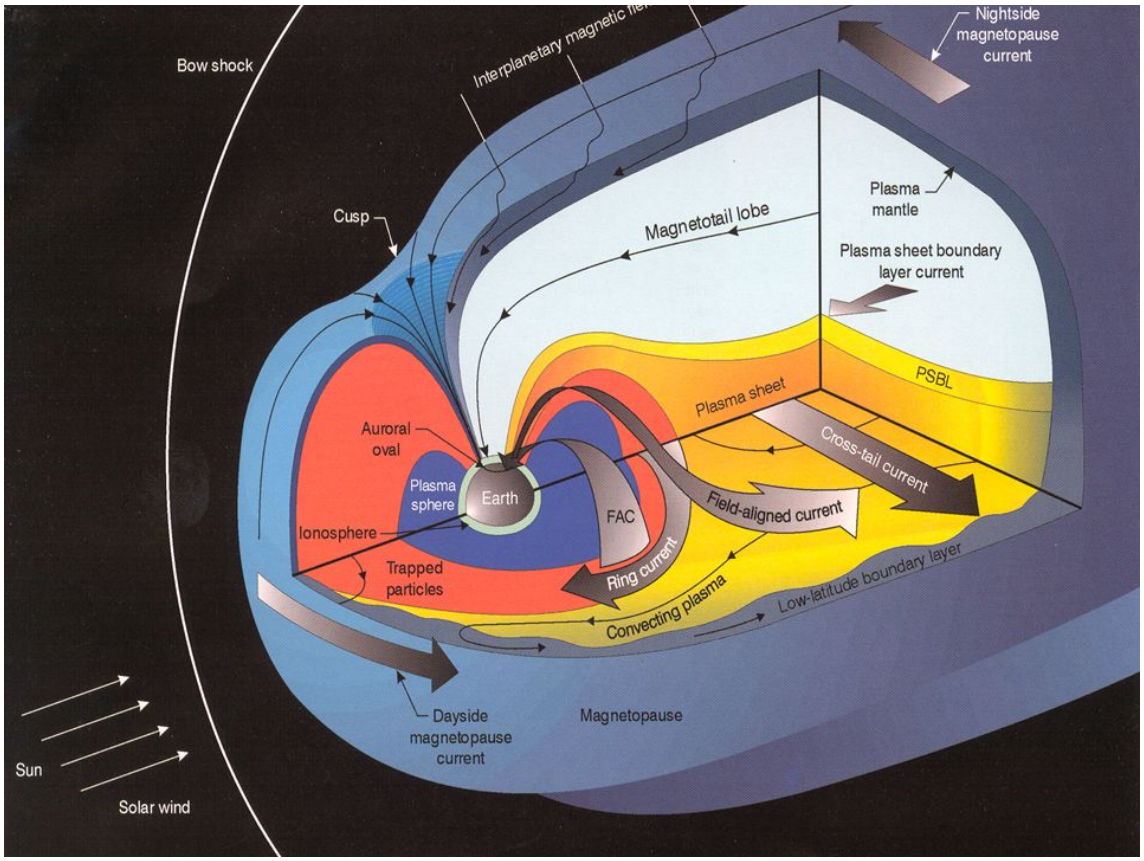

Figure 1.1.3: Schematic illustration of a cutaway 3-D magnetosphere. Image courtesy of *National Research Council* [2003].

a more complex model of a three-dimensional magnetopause which embeds the LLBL that extends from the subsolar point to the flanks in low-latitudes. Since this boundary layer is observed regardless of the IMF orientation [e.g., *Mitchell et al.*, 1987], it indicates solar wind plasma transport even during northward IMF conditions. The LLBL is thicker for northward IMF, while it is thinner for southward IMF; in both cases, it becomes thicker with increasing distance away from the subsolar point [*Mitchell et al.*, 1987]. The absence of major plasma transports during northward IMF conditions leads to an interest in how the LLBL is formed.

When the IMF is due north, the solar wind interactions with the Earth's magnetosphere are less obvious. Various mechanisms of how the LLBL is formed under northward IMF conditions have been proposed. *Sckopke et al.* [1981] explained the variation of the boundary layer thickness to be due to KH instability of the inner edge of the boundary layer. *Song and Russell* [1992] proposed that solar wind plasma enters and contributes to the LLBL formation from high-latitudes. Diffusive entries were also proposed [e.g., *Treumann et al.*, 1995; *Terasawa et al.*, 1997]. The magnetopause and adjacent boundary layer can be in motion due to variations in the solar wind conditions, e.g., in the solar wind dynamic pressure. Indeed, the flank magnetopause is unstable to KH instability due to the solar wind that creates a shear flow while the northward IMF is draped along the magne-

topause. KH instability can cause undulation of the magnetopause that generates quasi-periodic fluctuations consistent with satellite observations [e.g., *Chen et al.*, 1993]. KH instability itself cannot cause the solar wind transport into the magnetosphere; it needs a breaking of the frozen-in law or other related mechanisms. For these reasons, KH instability has gained particular interests for its contribution to the solar wind plasma transport under northward IMF conditions.

Understanding of the solar wind interaction with the terrestrial environment has significantly progressed in the past decades, thanks to abundant observations by many spacecraft missions. In this thesis, we are focusing on magnetopause surface waves that are induced by the KH instability. Magnetopause KH waves have complex structures that are best studied using multi-point observations. Studying structures of these KH waves would contribute to understanding in their roles in the solar wind plasma transport into the magnetosphere.

1.2 Magnetic Kelvin-Helmholtz (KH) Instability

KH instability is a classical instability of hydrodynamics. When two fluids have relative motion between them, the velocity shear interface is unstable to the KH instability. KH instability can also be triggered in MHD system in which a magnetic field is present. *Chandrasekhar* [1961] derived onsets of the magnetic KH instability for various uniform magnetic field configurations in a shear flow system in an ideal incompressible plasma. The most important result is that the magnetic field directing parallel to the shear flow suppresses the KH instability; the magnetic field directing perpendicular to the shear flow does not influence the KH instability. The onset condition of the magnetic KH instability can be written as [*Hasegawa*, 1975]

$$[\mathbf{k}\cdot(\mathbf{V_1}-\mathbf{V_2})]^2 > \frac{n_1+n_2}{\mu_0 m_p n_1 n_2}\left[(\mathbf{k}\cdot\mathbf{B_1})^2+(\mathbf{k}\cdot\mathbf{B_2})^2\right] \tag{1.1}$$

where 1,2 label the two sides of a shear layer, **k** is the wave vector, **V** is the plasma flow velocity, **B** is the magnetic field, n is the plasma number density, m_p is proton mass, and μ_0 is the vacuum permeability. The equation 1.1 applies to an infinitely thin boundary layer. The phase velocity of the KH mode is

$$V_{ph} = \frac{n_1\mathbf{k}\cdot\mathbf{V_1}+n_2\mathbf{k}\cdot\mathbf{V_2}}{k(n_1+n_2)} \tag{1.2}$$

that associates with the real part of the KH dispersion relation, $V_{ph}=\omega/k$, where ω is the wave frequency and k is the wave number. The growth rate of the KH instability, associated with the imaginary part of the dispersion relation, is given by

$$\gamma = \left[\alpha_1\alpha_2[(\mathbf{V_1}-\mathbf{V_2})\cdot\mathbf{k}]^2-\alpha_1(\mathbf{V_{A,1}}\cdot\mathbf{k})^2-\alpha_2(\mathbf{V_{A,2}}\cdot\mathbf{k})^2\right]^{1/2} \tag{1.3}$$

where $\alpha_1 = n_1/(n_1 + n_2)$ and $\alpha_2 = n_2/(n_1 + n_2)$, and $\mathbf{V_{A,1}}, \mathbf{V_{A,2}}$ label the Alfvén speeds on either side of the boundary. Equation 1.3 indicates that the shear layer is always unstable to the instability in the absence of the magnetic field for all non-zero shear flow. Also, the shear layer is always KH-unstable given the magnetic field is perpendicular to the wave vector. In such cases, the growth rate is proportional to the wavenumber, k, and the fastest growing mode occurs for the smallest wavelength ($k = 2\pi/\lambda$). The magnetic field parallel to the flow imposes the magnetic tension forces that destabilise the instability.

For a uniform density (n) and a magnetic field (**B**), the formula 1.1 reduces to

$$(\mathbf{k} \cdot \Delta\mathbf{V})^2 > (\mathbf{k} \cdot \mathbf{V_A})^2 \tag{1.4}$$

where $\Delta\mathbf{V} = (\mathbf{V_1} - \mathbf{V_2})/2$ is the half shear velocity and $\mathbf{V_A} = \mathbf{B}/\sqrt{\mu_0 n m_p}$ is the Alfvén speed. In other words, the KH instability will occur if the half velocity shear in the **k** direction exceeds the Alfvén speed along **k**. The linear stability of the shear flow has also been considered in other aspects, e.g., the influence of a magnetic field profile [*Hughes and Tobias*, 2001].

These theoretical considerations simplify the problems to incompressible plasmas with an infinitely thin shear layer. In the magnetospheric environments, plasmas are compressible and the magnetopause shear layer has finite thickness. There are a number of studies that consider the KH instability in the magnetospheric configuration and take non-ideal MHD effects into account. For example, assuming a 1-D tangential discontinuity with homogeneous plasmas and magnetic fields, compressibility is found to have a stabilising effect such that the KH instability only grows for a limited range of the velocity jump across a shear flow [e.g., *Talwar*, 1964; *Pu and Kivelson*, 1983]. *Ong and Roderick* [1972] studied the stability of the shear layer with a finite thickness when the Alfvén Mach number $M_A \gg 1$. In the incompressible case, they found that a finite thickness of the shear layer stabilises the KH mode for small wavelength perturbations (large wavenumber, k). In the compressible case, the stability of the shear layer of the finite thickness is further stabilised. *Miura and Pritchett* [1982] studied the finite shear layer thickness in a compressible plasma without restricting M_A. Using arbitrary orientation of the uniform magnetic field, velocity flow, and wave vector, they found that the fastest growing modes occur when $k\Delta L \sim$ 0.5 - 1.0, where ΔL is the shear layer thickness, and the only modes with $k\Delta L <$ 2, are KH unstable.

The linear analyses above can tell us in which conditions the shear layer would be unstable to the KH instability. However, they cannot predict consequences once the KH instability has developed. To understand evolution of the KH instability, nonlinear analyses of the instability have been performed by means of numerical simulations; their details will be given in the next section. Once the instability condition is satisfied, the perturbation grows exponentially, causing the

amplitude of the boundary waves to become larger; this phase is known as the `linear stage'. The instability then reaches the `nonlinear stage' when the perturbation growth becomes saturated. At this stage, the boundary waves begin to roll up and form vortical structures. In hydrodynamics, the rolled-up vortex structure is called ``Kelvin's Cat Eye''. In an absence of magnetic fields, this structure is found to be stable and would spin indefinitely in a limit of small viscosity [*Frank et al.*, 1996]. When a weak magnetic field is introduced, it can lead to a dramatic change in the evolution compared to the hydrodynamic regimes [e.g., *Malagoli et al.*, 1996; *Jones et al.*, 1997]. Amongst others, *Ryu et al.* [2000] studied evolution of the nonlinear KH instability in the presence of magnetic fields using 3-D MHD simulations. They found that weak magnetic fields embedded in KH flow can be stretched and twisted as the vortical structure forms. This structure is the main feature of nonlinear KH instability in which its dynamics can be important in various plasma environments.

Magnetic KH instabilities are observed inside and beyond the solar system. They are observed at some planetary magnetospheric boundaries such as those of the Mercury [e.g., *Slavin et al.*, 2008], the Earth (see the next section), and the Saturn [e.g., *Masters et al.*, 2010]. In the solar atmosphere, it is observed in the flank of a coronal mass ejection [*Foullon et al.*, 2011] (see panel (a) of Figure 1.2.1) and a prominence [*Hillier and Polito*, 2018] in the solar corona. The flanks of the heliopause are suggested to be subjected to KH instability using Voyager 1 observations [*Borovikov and Pogorelov*, 2014].

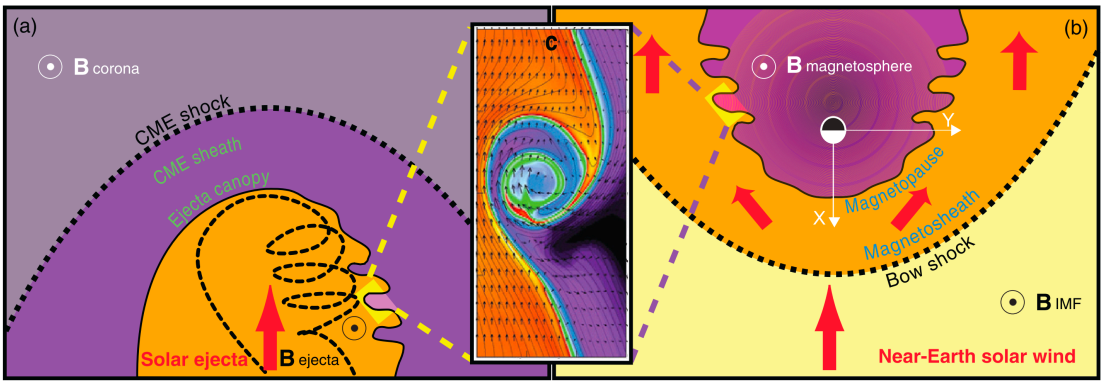

Figure 1.2.1: Illustrations of the KH instability at (a) the coronal mass ejection (CME) and (b) the Earth's magnetosphere on the dawn-side, with (c) a close-up view of the KH vortex from numerical simulations [*Nykyri et al.*, 2006]. (a) The KH instability is induced at the interface between the flank of solar ejecta where the plasma is hot (shown in orange) and the ejecta canopy where the plasma is colder (shown in purple). (b) The KH instability is induced at the interface between the magnetosphere where the plasma is cold (purple) and the magnetosheath where the plasma is hot (orange). One of the main differences between KH instabilities in panels (a) and (b) is the direction of magnetic field **B** relative to the direction of the shear flow (shown as red vectors). Courtesy of *Foullon et al.* [2011].

1.3 Magnetopause KH Waves

Magnetic KH instability was suggested to be responsible for surface waves on the magnetopause that could explain the irregular disturbance seen in magnetic data from a spacecraft by *Dungey and Southwood* [1970]. Early investigations include its association to geomagnetic pulsations observed by ground stations. Magnetic KH waves were proposed to be responsible for ULF wave pulsations in range Pc3 - Pc5. Pc is a notation that is used to classified geomagnetic micropulsations [*Jacobs et al.*, 1964]. Pc3, Pc4, and Pc5 are the pulsations with period ranges of 10 - 45 seconds, 45 -150 seconds, and 150 - 600 seconds, respectively. The discoveries of the magnetopause and the low-latitude boundary layer lead to examinations of the stability of KH waves with conditions specific to the magnetospheric boundary. The LLBL on the flank magnetopause is prone to KH instability under northward IMF conditions (following the KH onset condition in equation 1.1) as shown in Figure 1.3.2. KH instability has been proposed to contribute to the formation of the LLBL [e.g., *Sckopke et al.*, 1981]. Magnetopause surface waves with periodic fluctuations and non-sinusoidal waveforms of possibly a KH origin were observed [e.g., *Hones et al.*, 1981; *Chen et al.*, 1993]. Clear evidence of in-situ magnetopause KH waves was first reported in *Fairfield et al.* [2000]. These KH waves were successfully reproduced and compared with an MHD simulation by *Otto and Fairfield* [2000]; they further suggested that KH waves can mediate mass transport into the magnetosphere via reconnection inside rolled-up KH vortices. Since then, magnetopause KH waves have been extensively studied primarily for their roles in solar wind transport into the magnetosphere under northward IMF conditions.

Various mechanisms of how reconnection takes place in KH waves have been proposed. Using resistive MHD simulations, *Nykyri and Otto* [2001] showed that the vortex motion could cause the magnetic fields to be highly stretched such that multiple current sheets are induced inside rolled-up KH vortices. Reconnection at these current sheets allows the magnetosheath plasma to detach and enter the magnetospheric side. *Nakamura et al.* [2006] illustrated another type of reconnection that can take place in the wave trailing edge (as opposed to inside the rolled-up vortex) when magnetic field components across the shear layer are anti-parallel. *Nakamura et al.* [2008] studied both types of reconnection in KH waves and showed that reconnection at the trailing edge could also lead to direct plasma mixing. They named reconnection at the wave trailing edge as type-I vortex-induced-reconnection (VIR) and that in the rolled-up vortex as type-II VIR as summarised in Figure 1.3.1. Type-II and type-I VIR were confirmed using Cluster observations by *Nykyri et al.* [2006] and *Hasegawa et al.* [2009], respectively. Magnetic islands produced by multiple type-I VIR were shown to enhance plasma mixing via second re-reconnection which incorporates them into the vortex body

[*Nakamura et al.*, 2011, 2013]. These magnetic islands were observed in the trailing edges of KH waves using THEMIS by *Eriksson et al.* [2009].

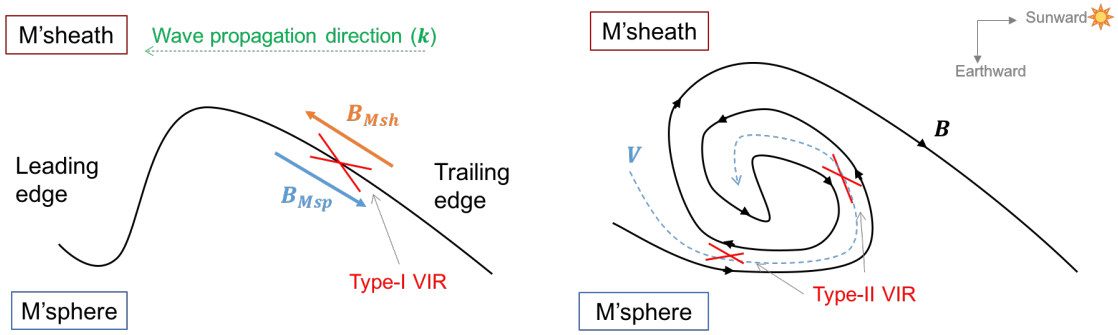

Figure 1.3.1: Schematic illustrations of the reconnection induced by KH waves.

KH waves may also induce remote reconnection away from the equatorial plane. *Bavassano Cattaneo et al.* [2010] identified field-aligned ion populations inside KH vortices in Cluster observations that cannot be explained with the local reconnection. These ion populations signal instead of the lobe reconnection in the southern hemisphere [e.g., *Fuselier et al.*, 1997]. A more complex type of reconnection induced by KH vortices so-called ``double mid-latitude reconnection" was proposed using three-dimensional Hall MHD simulations by *Faganello et al.* [2012a]. Current sheets were shown to develop from torsion of the magnetic fields due to the vortex motion at the equatorial plane and stabilisation of the KH instability at higher latitude planes [e.g., *Faganello et al.*, 2012b; *Borgogno et al.*, 2015; *Ma et al.*, 2017]. Evidence of the mid-latitude reconnection was reported in Time History of Events and Macroscale Interactions during Substorms (THEMIS) [*Faganello et al.*, 2014] and Magnetospheric Multiscale (MMS) [*Vernisse et al.*, 2016] observations.

Other mechanisms operating in the vicinity of KH waves were also proposed to enhance plasma mixing. Turbulence was shown to develop at the KH wave edges via secondary non-linear instabilities which can cause large-scale plasma mixing at the boundary layer [*Matsumoto and Hoshino*, 2004]. Secondary instabilities were also shown to develop due to differential flow along KH wave edges due to parasitic electron dynamics [*Nakamura et al.*, 2004]. *Chaston et al.* [2007] reported evidence of mode conversion from surface waves to kinetic Alfvén waves that suggests a diffusive transport across the magnetopause due to KH waves. Indeed, magnetopause KH waves were postulated to play essential roles during their non-linear stages. Strong evidence of rolled-up KH vortices was first reported by *Hasegawa et al.* [2004] using Cluster observations. Using three-dimensional MHD simulations, *Takagi et al.* [2006] found a distinct plasma population that travels faster than that of the magnetosheath when rolled-up KH vortices are developed. This distinct population has been commonly used as a marker for non-linear KH waves in single- and multi-spacecraft observations [e.g., *Hasegawa et al.*,

2006; *Taylor et al.*, 2012; *Lin et al.*, 2014]. However, this proxy is not unique to rolled-up KH waves as it can be featured by the presence of a plasma depletion layer, formed under northward IMF conditions adjacent to the magnetopause, or the LLBL background flow itself [*Plaschke et al.*, 2014].

When the IMF is due northward, a portion of the dayside and flank magnetopause can be unstable to KH instability. Based on the linear theory in equation 1.1, the boundary layer is most unstable to the KH instability where $\mathbf{k}\cdot\mathbf{B}$ is minimised. This KH-unstable region occupies the low-latitude magnetopause along both dusk and dawn flank magnetopause as seen in panel (a) of Figure 1.3.2. Let us define the IMF clock angle as the clockwise angle of the IMF direction away from the geomagnetic north direction. *Farrugia et al.* [1998] showed theoretically and numerically that, when the IMF is inclined with a positive clock angle as shown in panel (b) of Figure 1.3.2, the KH unstable region is shifted towards the southern hemisphere on the dusk-side (and the northern hemisphere on the dawn-side) and the unstable strip becomes narrower. Moreover, they found that the magnetopause is unstable to short wavelength perturbations and the growth rates are slightly reduced. Therefore, short wavelength waves are generated from the strips for large IMF clock angle, while longer wavelength waves are generated for lower IMF clock angle.

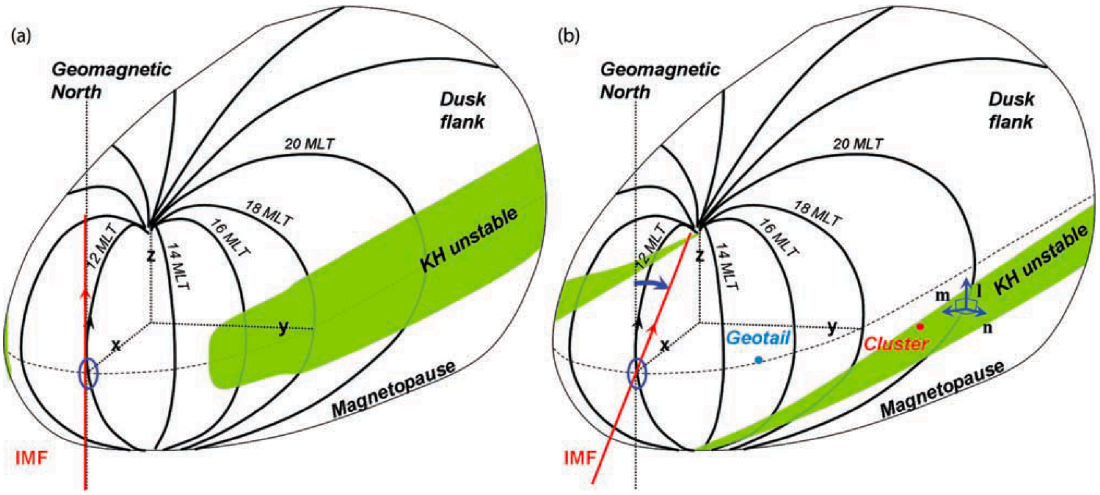

Figure 1.3.2: View of the day-side magnetopause with northward IMF. The green region is the flank magnetopause that is prone to KH instability. Image courtesy of *Foullon et al.* [2008].

Multi-spacecraft observations with large spatial coverage bring about the understanding of KH waves in large-scales. Using Geotail and Cluster that separates with a distance along the dusk-side flank magnetopause as shown in panel (b) of Figure 1.3.2, *Foullon et al.* [2008] characterised evolution of magnetopause KH waves regarding the changes in the adjacent boundary layer thickness, IMF orientation, and geomagnetic latitude. Furthermore, properties of the waves such as wavelength, wavefront steepness, and propagation direction were resolved at

Cluster. They confirmed observationally the dependence of IMF clock angle on the KH wavelength and amplitude proposed by *Farrugia et al.* [1998]. Their results further indicate that these waves were remotely generated on the dayside. The boundary layer thickness is found to impact the amplitude, wavefront steepness, and direction of propagation. This work sets an excellent example in using multi-spacecraft techniques and multi-spacecraft data to obtain spatial properties of magnetopause KH waves.

Magnetopause KH waves generated on the dayside magnetopause propagate tailward along the flanks. The waves can evolve from linear to non-linear stages with distance away from the subsolar point. Using global simulations of KH waves under northward IMF conditions, *Li et al.* [2012] summarised four phases of the spatial development of the KH instability into quasi-stable, exponential growth, linear growth, and nonlinear. These four stages are illustrated in Figure 1.3.3. From their model, the non-linear KH waves were expected beyond the post-terminator.

There are some intrinsic differences between KH waves developed on the dawn-side and dusk-side magnetopause. When the IMF is due north, magnetic field lines on both sides of the magnetopause are pointing northward. Since the magnetosheath plasma flows tailward, it goes in opposite directions for the simulations of the dawn and the dusk sides with respect to the magnetosphere (for the given fixed magnetic field orientations) as shown in panel (b) of Figure 1.2.1. Figure 4.4.1 will illustrate one of simulations on the dusk-side flank magnetopause. The direction of the magnetosheath flow relative to the static magnetosphere consequently affects the sign of the vorticity of the shear layer: the vorticity of the shear layer on the dusk-side is positive while on the dawn-side it is negative as seen from above.

Magnetopause KH waves can also be observed under other IMF orientations. The KH onset condition (equation 1.1) can indeed be satisfied for both southward and northward IMF conditions at the flank magnetopause. Additionally, this condition can be satisfied somewhere else on the magnetopause under various IMF orientations. KH waves under southward IMF conditions are observed [*Hwang et al.*, 2011]; though they were found to be temporally intermittent and spatially irregular. Abundant spacecraft observations also reveal KH detections in other IMF conditions such as dawn-ward (at high-latitudes) [*Hwang et al.*, 2012], radial [*Farrugia et al.*, 2014; *Grygorov et al.*, 2016], and parker-spiral [*Adamson et al.*, 2016]. The analysis of 7 years of THEMIS data revealed that KH waves could occur up to 19% of the time under northward IMF conditions [*Kavosi and Raeder*, 2015]; this should set a lower limit for the ubiquity of the KH waves on the Earth's magnetopause [*Masson and Nykyri*, 2018].

Indeed, KH waves involve multi-scale processes where the free energy is provided in large-scale (MHD scale), transferred into a smaller scale, and dissipated

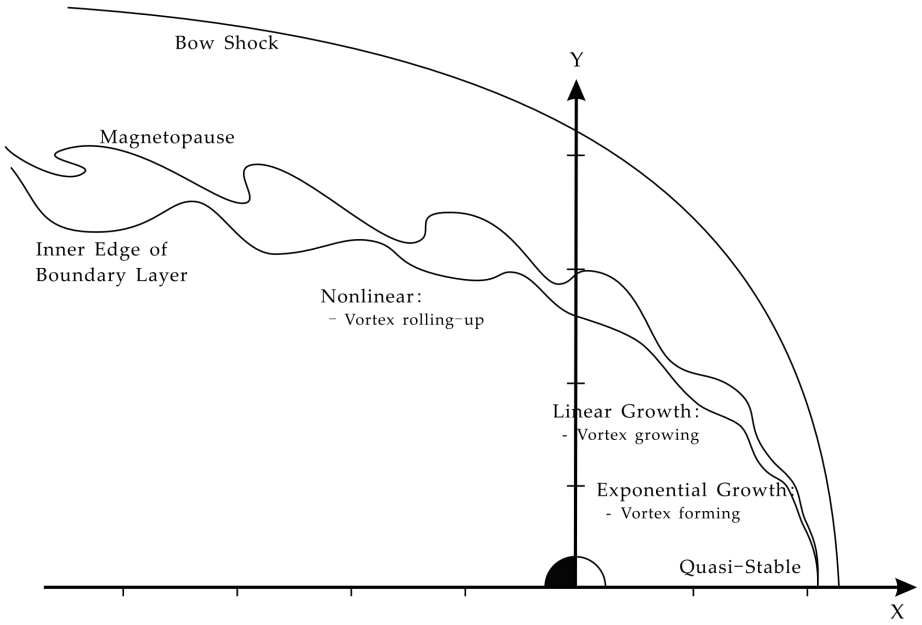

Figure 1.3.3: Spatial development of the KH waves along the flank magnetopause. Image courtesy of *Li et al.* [2012].

in the smallest scale (kinetic scale). *Moore et al.* [2016] provided the first strong evidence of cross-scale energy transport inside a KH vortex from the fluid scale to the ion scale, using an exceptional case of Cluster observations, which allows the investigation of a fundamental problem in space plasmas (see the review by *Retinò* [2016]). Four-spacecraft observations have been proved to be valuable in understanding magnetopause KH waves that involve coupling in multi-scales which would be best addressed by simultaneous multi-scale observations.

Magnetopause KH waves are MHD structures with smaller-scale structures residing in them. While many mechanisms have been proposed, they have yet to be confirmed with satellite observations. Magnetopause KH waves have complex structures that are best studied with multi-satellite observations. Nevertheless, most literature was conducted using single satellite observations in which the spatial characteristics of those waves cannot be resolved. Characterising detailed characteristics of the waves would be useful for understanding physical processes that are operating inside them. Studying these waves in the Earth's magnetospheric environments would also be useful to understand magnetic KH waves in other conditions where in-situ, multi-spacecraft measurements are inaccessible.

1.4 Techniques for Space Plasmas: from Single- to Multi-Spacecraft

In-situ observations using satellites and rockets have brought about significant understanding of the solar wind and Earth's magnetosphere interaction. Radio

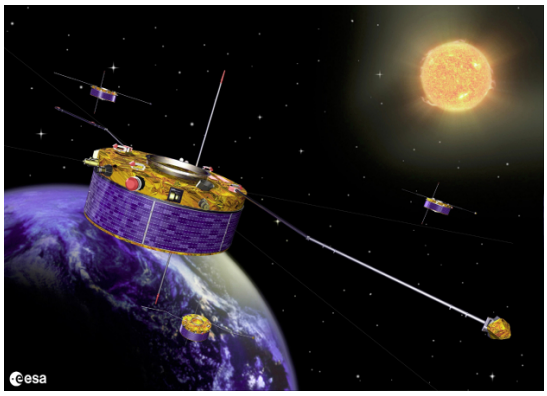

Figure 1.4.1: Artist impression of Cluster mission. Credit: ESA.

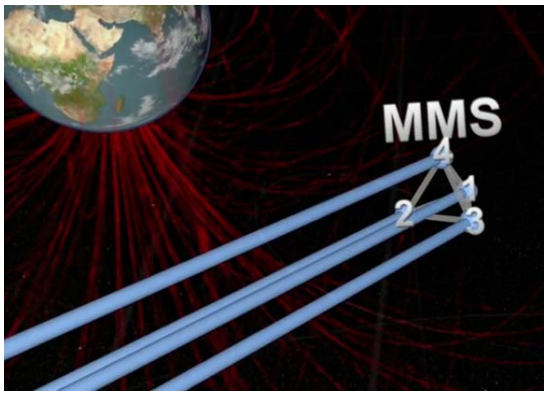

Figure 1.4.2: Artist impression of MMS mission. Credit: NASA.

transmitters and receivers were early technologies that verified the existence of the ionosphere. The magnetopause boundary was discovered from abrupt transitions in magnetic fields observed by Explorer 12 [e.g., *Cahill and Amazeen*, 1963], which confirmed the theoretical prediction by *Chapman and Ferraro* [1931]. Later satellites that were launched to the solar wind also led to the discovery of the bow shock.

There are a number of spacecraft that have been sent to probe interaction between the solar wind and Earth's magnetosphere. Since the magnetopause can be in motion, the measurements from single satellites are sometimes ambiguous, such that we cannot distinguish between the fluctuations from spatial and temporal changes. The International Sun-Earth Explorer (ISEE) 1 and 2 were the first pair of satellites that were launched in 1977 in an attempt to resolve the spatial-temporal ambiguity which was inevitable for single spacecraft measurements. However, such dual spacecraft have to be in the direction normal to the boundary during the crossing to remove the uncertainties, e.g., for estimations of the magnetopause thickness [*Berchem and Russell*, 1982]. For this reason, the four identical spacecraft with a tetrahedral formation were proposed in 1982 and implemented for Cluster mission by the European Space Agency (ESA) (see Figure 1.4.1). The Cluster mission was successfully launched in 2000 after the launch failure in 1996 due to the explosion of Ariane 5 rocket. Cluster has been orbiting the Earth's magnetosphere since then which bring about progress in understanding in the solar-terrestrial interactions. In 2015, NASA launched the new four-spacecraft Magnetospheric Multiscale (MMS) mission (see Figure 1.4.2) with much smaller tetrahedral formation than Cluster to probe magnetic reconnection in the Earth's magnetosphere. Various analysis techniques were developed to understand in-situ data from those satellites which led to many important discoveries. We are reviewing those techniques, in particular, for the analyses of the magnetopause structure.

After the discovery of the magnetopause in 1963, space data techniques are

developed to examine the properties of this boundary. In particular, *Dungey* [1961] proposed that the magnetopause can be open or closed during southward or northward IMF, respectively. To test this idea, *Sonnerup and Cahill* [1967] developed a technique called the Minimum Variance Analysis (MVA) in order to determine the direction normal to the magnetopause. Since the magnetic field is divergence-free, the normal component of the magnetic field must be continuous. By minimising the magnetometer data of in-situ magnetopause crossings, they illustrate two types of the boundary: the rotational and tangential discontinuity. The rotational discontinuity corresponds to the non-zero normal field component of the open magnetopause while the tangential discontinuity corresponds to the zero normal field component of the closed magnetopause. The technique has also been extended to applications of other quantities unlimited to magnetic fields [e.g., *Sonnerup and Scheible*, 1998]. *Russell et al.* [1983] developed multi-spacecraft timing technique to determine the normal and speed of the shock boundary observed by a set of four spacecraft (ISEE 1, 2, 3, and Interplanetary Monitoring Platform, IMP, 8). This method is based on the assumption that the boundary or discontinuity is planar. By constructing an over-determined system of the separation vectors and time delays between spacecraft, one can resolve for the normal and speed of a planar boundary that passes them. The timing technique has also been applied to the magnetopause boundary [e.g., *Owen et al.*, 2001]. Both MVA and timing methods have been commonly used to determine the magnetopause normal; in case of four-spacecraft, the two methods can lead to different results [*Haaland et al.*, 2004]. The lack of consistency is suggested because the planarity assumption made by the timing method is often unsatisfied. Nevertheless, the planarity assumption is valid when the average distance between four spacecraft is much smaller than the scale size of the structure [*Schwartz*, 1998]. The accuracy of the timing technique is also tested against the MVA technique in solar wind discontinuities [e.g., *Knetter et al.*, 2004; *Vogt et al.*, 2011]. The MVA technique is sometimes referred to the timing method because it leads to an optimum direction of the normal magnetic field, e.g., when transformed into the local boundary coordinates [see supplementary information in *Eriksson et al.*, 2016].

During the preparation phase of Cluster mission, techniques for estimating gradients of vectors and scalars measured by the four-spacecraft tetrahedron were developed. Using the least squares determination, the gradient is found to be expressed in terms of the symmetric tensor, so-called the ``volumetric tensor'', constructed from the relative positions of the four spacecraft [*Harvey*, 1998]. This volumetric tensor contains information of the tetrahedron formation such that its size, elongation, and planarity can be obtained [*Robert et al.*, 1998]. *Chanteur* [1998] proposed an alternative method for gradient estimations that utilise the barycentric coordinates which is much practiced in geometry to interpolate gradients at the

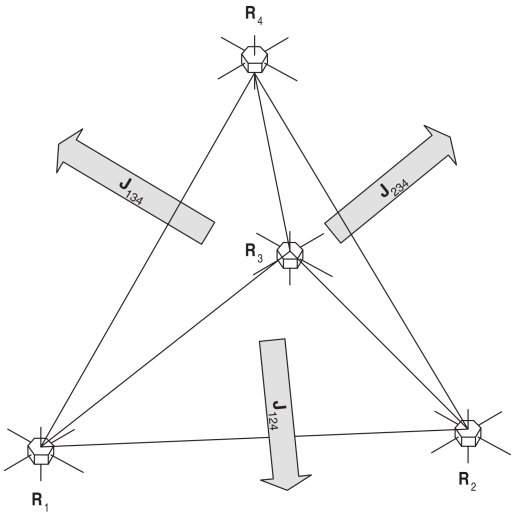

Figure 1.4.3: Sketch of the curlometer technique. Image courtesy of *Dunlop et al.* [2002]

tetrahedron barycentre. These two methods for linear gradient estimations are mathematically equivalent and are tested on simulated magnetic field data with varying tetrahedron shapes [*Chanteur and Harvey*, 1998]. The two methods can give different results especially when the tetrahedron formation is highly irregular, with no clear indication of which method is better. The divergence-free condition can be incorporated into the gradient estimators, though it does not necessarily improve the results because this term involves nonlinear terms that are missed by the linear gradient estimations. Nevertheless, the methods have been proved to be valuable in understanding observational data. The linear estimators form a central part of other gradient-based methods that are derived for four-spacecraft applications in Cluster and MMS observations.

An important gradient quantity that can be calculated using the four-spacecraft tetrahedron is the curl of a vector field. *Dunlop et al.* [1988] develops the curlometer technique for estimating the current density from the magnetometers of Cluster. By expressing Ampere's law in the integral form, one can estimate the current density flux through each face of the tetrahedron from the line integral of the magnetic field around the triangular surface as illustrated in Figure 1.4.3; the total current density is then the sum of the six faces of a tetrahedron. The yielded current density is accurate when the tetrahedron size is much smaller than the current system. Impacts of tetrahedron shape and measurement errors on the accuracy of the current density were tested in simulations by *Robert et al.* [1998] and *Vogt and Paschmann* [1998] (addressed there as the vorticity). *Dunlop et al.* [2002] first applied the curlometer technique on Cluster data to test its applicability. They suggest to use the divergence of the magnetic field to monitor the effect of nonlinear gradients, though it is less meaningful when the tetrahedron formation is highly irregular. Impacts of the relative size of the tetrahedron size with respect

to the width of a line current are tested in simulations by *Forsyth et al.* [2011]. The curlometer tends to underestimate the current when the width of line currents is less than the spacecraft separation. Although these limitations can affect the accuracy of the technique, the applications of the technique have proven to be reliable in many regions of the magnetosphere [*Dunlop et al.*, 2016].

When multiple satellites are crossing the magnetopause boundary, we no longer have to assume a one-dimensionality or planarity of the structure. *Mottez and Chanteur* [1994] gave a theoretical derivation for determining local geometry of a surface boundary crossed by a group of satellites by assuming a rigid surface with constant curvature. Curvature was also proposed to be derived from a relaxation of the planarity and steady motion assumptions [*Dunlop and Woodward*, 1998]. Without any prior assumptions about the structure, four-spacecraft tetrahedron allows an estimation of in-situ magnetic curvature using the linear gradient estimators. *Shen et al.* [2003] develop a technique called ``Magnetic Curvature Analysis (MCA)" to calculate the magnetic curvature by projecting the unit magnetic field component into its gradient ($\mathbf{b} \cdot \nabla \mathbf{b}$) to sketch the local geometry of the magnetotail current sheets in Cluster observations. The technique estimates magnetic curvature which gives a corresponding curvature radius at the tetrahedron barycentre as shown in Figure 1.4.4. The MCA technique is further generalised and called ``Magnetic Rotation Analysis (MRA)" in order to find a rotation of the magnetic field in an arbitrary direction [*Shen et al.*, 2007], in which its applications have been applied into a magnetic flux rope. *Shi et al.* [2005] developed a technique called ``Minimum Directional Derivative (MDD)" to investigate dimensionality of magnetic structures. These four-spacecraft applications bring insights into observations of magnetic structures with four-spacecraft, e.g., of magnetic reconnection [*Runov et al.*, 2003, 2005]. For simple magnetic structures, these techniques readily yield uncomplicated outputs. In addition, the techniques are needed to be well-understood for correct knowledge of real data interpretations. Some of the techniques are tested in simulations in order to understand applications and errors of the techniques [e.g., *Denton et al.*, 2010, 2012]. However, plasma structures can be complex. Therefore, those techniques should be first applied to simulations for accurate interpretations of real data.

With the availability of Cluster and MMS data, four-spacecraft techniques are becoming routinely practiced. Of particular interest is how the inter-spacecraft separation impacts four-spacecraft outputs, as these two missions have different tetrahedron formation scale sizes. Also, plasma processes take place in various spatial and temporal scales. Using either of the missions, one scale can be resolved at a time. So how do we best understand the data when only one-scale is available? This problem is probably phenomena-specific but has broad implications as certain plasma characteristics are ubiquitous. Studying the relative

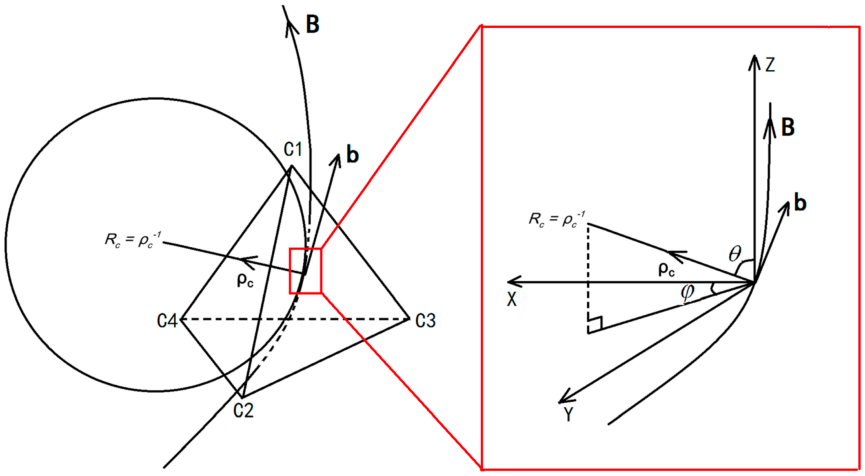

Figure 1.4.4: Sketch of the MCA technique. Image courtesy of *Zhang et al.* [2016]

sizes of the physical phenomena to the tetrahedron configuration is, therefore, an important aspect, especially for future simultaneous, multi-scale observations.

1.5 Motivation and Outline of the Thesis

While KH waves were proposed to contribute to the solar wind plasma transport under northward IMF conditions, the role of magnetopause KH waves in plasma transport is not yet conclusive. Since magnetopause KH waves have rather complex structures, they are best studied using multi-satellites. Past literature was limited to single and multi-point observations where spatial characteristics of the waves were not resolved. Using four spacecraft forming a tetrahedral configuration, we aim to characterise in-situ spatial properties of the waves. These would help to address other mechanisms that are operating inside them at the magnetopause.

Four-spacecraft allows linear estimations of three-dimensional gradients that are essential to understand plasma phenomena. While the current four-spacecraft missions allow measurements at one scale at a time, future space plasma observations may involve simultaneous, multi-scale observations in which outputs from various tetrahedron sizes should be discussed. Magnetopause KH wave structures involve bent magnetic fields and vortical flows that are ubiquitous in plasmas. Analysing such structures would have broad applications in space plasma observations.

The purpose of this thesis is twofold, first, to explore new science of magnetopause KH waves that may emerge from four-point measurements, and, second, to understand the four-spacecraft tools and their applications using various sizes of tetrahedral configuration. The research questions are as the following.

1. What are the four-spacecraft characteristics of magnetopause KH waves?

2. How do the four-spacecraft characteristics change with the tetrahedron size?

3. What are applications of the four-spacecraft tools in multiple scales?

To address the first two questions, we may first consider applications of the four-spacecraft tools in a numerical simulation of typical magnetopause KH waves. Characteristics of the waves can be resolved using varying scale sizes of tetrahedron covering from Cluster to MMS separation ranges. To address the third question, we need to analyse real observations from both four-spacecraft missions. The thesis is outlined as follows.

Chapter 2 introduces the numerical codes that will be used to simulate magnetopause KH waves. Numerical work that was used to study KH waves in literature is briefly reviewed here.

Chapter 3 gives analytical derivations of the four-spacecraft techniques which include the MCA, curlometer, and timing analysis techniques.

Chapter 4 shows applications of the four-spacecraft tools on an MHD simulation with typical conditions on the flank magnetopause. In-situ signatures of the waves are predicted for Cluster observations. Impacts of tetrahedron size on the four-spacecraft measures are discussed.

Chapter 5 shows Cluster observations of KH waves. Predicted signatures are confirmed and further characterised with changes in solar wind conditions. Various KH wavelengths in the event controlled by different IMF clock angles allow the test of the four-spacecraft applications with various tetrahedron size.

Chapter 6 shows MMS observations of KH waves. Small-scale structures in the KH waves are analysed using the four-spacecraft tools. Four-spacecraft analyses of these structures are used to complement interpretations from particle data.

Chapter 7 summarises findings of the thesis and gives an outlook for potential future work.

Chapter 2

Numerical Simulation

This Chapter presents a literature review on numerical studies of magnetopause KH waves (Section 2.1) and numerical codes (Section 2.2) that will be used to simulate the KH waves.

2.1 Numerical studies of magnetopause KH waves

KH instability in the Earth's magnetospheric environments is commonly studied using numerical simulations. Depending on the physical effects one wants to study, the choices of simulations are different. Early two-dimensional simulations include MHD with compressible plasma [e.g., *Miura*, 1984, 1987], Hall MHD [e.g., *Huba*, 1994], and Finite Larmor Radius MHD [e.g., *Huba*, 1996]. Using MHD simulations, *Otto and Fairfield* [2000] illustrate that the Geotail observations of quasi-periodic variations in the magnetotail boundary [*Fairfield et al.*, 2000] are caused by the KH instability. These simulations are extended to include the resistivity to illustrate plasma transport due to reconnection in KH vortices [*Nykyri and Otto*, 2001]. *Matsumoto and Hoshino* [2004] study the impact of density inhomogeneity across the boundary layer on the onset of turbulence inside a KH vortex. Later MHD simulations use empirical inputs from Cluster observations and take into account three-dimensional effects [*Takagi et al.*, 2006]. Using Hall MHD three-dimensional simulations, *Faganello et al.* [2012b] show that KH instability can kink magnetic fields at mid-latitude due to stabilising effects at a higher latitude which trigger thin current sheet formation that is susceptible to reconnection. There are also global MHD simulations such as *Guo et al.* [2010] which shows different surface wave modes propagating on either side of the magnetopause boundary and *Li et al.* [2012] which shows the spatial distribution of KH waves in different stages of development along the magnetopause.

Kinetic effects on magnetospheric KH waves have also been studied using hybrid, two-fluid, and particle simulations. Early hybrid simulations are focused on ion mixing in various conditions including uniform density and magnetic field [e.g.,

Terasawa et al., 1992], non-uniform density [*Thomas and Winske*, 1993], and non-uniform magnetic field [*Fujimoto and Terasawa*, 1995]. Hybrid simulations are also used to study diffusion caused by the KH instability with varying ion density jump *Cowee et al.* [2009] and magnetic shear [*Cowee et al.*, 2010]. Two-fluid codes have been used to study ion [*Fujimoto and Terasawa*, 1991] and electron inertial effects [*Nakamura et al.*, 2004]; the latter of which has been extended to illustrate two types of reconnection induced in the KH vortex [*Nakamura et al.*, 2008]. Fully kinetic simulations have been performed to study the vortex-induced reconnection in two-dimensions [*Nakamura et al.*, 2011] and three-dimensions [*Nakamura et al.*, 2013] which are also shown to produce magnetic islands consistent with the THEMIS observations [*Eriksson et al.*, 2009]. Recently, a KH event observed by MMS [e.g., *Eriksson et al.*, 2016] is reproduced using a three-dimensional fully kinetic simulation [*Nakamura et al.*, 2017] to investigate the plasma transport of the MMS event.

To capture the structural properties of the KH waves that would be detected with four-spacecraft, MHD simulations are a good choice. Considering the Cluster separation between 100 km and 18,000 km (with a sampling resolution of 4 seconds), MHD approximations would be valid for most observations at the Earth's flank magnetopause. Although kinetic simulations are desirable as fewer approximations are made, they are numerically expensive and unnecessary for structural analyses. In addition, MHD simulations are preferred to kinetic simulations because they are less noisy, suitable for most existed KH observations with Cluster. Four-spacecraft applications on the MHD simulations are needed to understand the outputs and limitations of the tools considering that the tetrahedron size is variable. We are employing MHD codes to simulate magnetopause KH waves in which their first-order, macroscopic properties can be extracted and observed with four-spacecraft.

2.2 LareXd codes

LareXd [*Arber et al.*, 2001] are Lagrangian remap codes that solve resistive MHD equations in two or three dimensions. These Lagrangian remap codes split each time-step into a Lagrangian step and then remap onto the original grid. The approach is based on control volume averaging with a staggered grid. The main motivation of *LareXd* codes are to solve problems in solar corona physics where resistivity and viscosity must be incorporated. Nevertheless, *LareXd* codes also allow us to simulate plasma phenomena unlimited to solar corona environments.

The codes solve MHD equations with resistivity in Lagrangian form as the fol-

lowing

$$\frac{D\rho}{Dt} = -\rho\nabla\cdot\mathbf{v}, \tag{2.1}$$

$$\frac{D\mathbf{v}}{Dt} = \frac{1}{\rho}(\nabla\times\mathbf{B})\times\mathbf{B} - \frac{1}{\rho}\nabla P, \tag{2.2}$$

$$\frac{D\mathbf{B}}{Dt} = (\mathbf{B}\cdot\nabla)\mathbf{v} - \mathbf{B}(\nabla\cdot\mathbf{v}) - \nabla\times(\eta\nabla\times\mathbf{B}), \tag{2.3}$$

$$\frac{D\varepsilon}{Dt} = -\frac{P}{\rho}\nabla\cdot\mathbf{v} + \frac{\eta}{\rho}j^2, \tag{2.4}$$

with the Ohm's law for resistive MHD

$$\mathbf{E} + \mathbf{v}\times\mathbf{B} = \eta\mathbf{j}, \tag{2.5}$$

where ρ is the number density, **v** is the velocity field, **B** is the magnetic field, P is the thermal pressure, η is the resistivity that is given as the inverse Lundquist number, $\varepsilon = P/\rho(\gamma-1)$ is the internal energy density where $\gamma = 5/3$ is the specific heat ratio, $\mathbf{j} = (\nabla\times\mathbf{B})/\mu_0$ is the current density where μ_0 is the vacuum permeability, and **E** is the electric field. The solenoidality constraint, $\nabla\cdot\mathbf{B} = 0$, is enforced throughout. The constraint transport model [*Evans and Hawley*, 1988] is used to keep the divergence of B at zero on the staggered grid within the machine precision.

In the codes, the resistivity η is given as `background resistivity' and `anomalous resistivity'. I set the background resistivity to be zero. This is appropriate because magnetospheric plasmas are collisionless. The anomalous resistivity is set to be very low at $1e-11$ which is the default value in the codes. This will be triggered when the maximum current density reaches the value of $J_c = 1.1J_0 = 28.8$ nA m^{-2}. This threshold value is similar to the value in *Otto and Fairfield* [2000] where their initial conditions and normalisations will be adapted to model KH waves in Chapter 4. *Otto and Fairfield* [2000] allowed the resistivity to be switched on when the threshold current density is reached to avoid the evolution of too narrow and too strong current sheets. They further found that the choice of the resistivity has a minor influence of the dynamics of the KH vortex evolution. *Nykyri and Otto* [2001] modeled the resistivity to be depending on current density including the case of no resistivity. They found that the choice of resistivity model does not impact the plasma transport allowed by reconnection in the KH vortex. Since our primary goal is to study KH waves in the magnetospheric environment, the above choice of resistivity is sufficient. Magnetic reconnection may occur in our simulations but it is not the focus of the simulation study in Chapter 4.

The code uses normalised values of parameters. The basic normalisations

are the length L_0, magnetic field B_0 and density ρ_0, such that

$$x = L_0\hat{x}, \qquad \mathbf{B} = B_0\hat{\mathbf{B}}, \qquad \rho = \rho_0\hat{\rho}. \tag{2.6}$$

Other important parameters are then defined through

$$v_0 = \frac{B_0}{\sqrt{\mu_0\rho_0}}, \qquad t_0 = \frac{L_0}{v_0}, \qquad P_0 = \frac{B_0^2}{\mu_0}. \tag{2.7}$$

Note that the plasma beta (β) is not a free parameter as the thermal pressure is normalised to magnetic pressure.

The code uses a staggered grid where scalar and vector quantities must be defined at different points in a grid cell as shown in Figure 2.2.1. The choice of a staggered grid is to build conservation laws into the finite difference scheme and to prevent checkerboard instabilities. For 2-D grid cells, velocity components are defined at cell corners. Defining all the velocities at a single point leads to a more compact code because a single velocity control volume can be used at the remap stage, hence the choice of a staggered grid. All scalars such as density, pressure, internal specific energy, and the ignorable magnetic field component B_z are defined at cell centres. The remaining magnetic field components are defined at cell edges. Given initial conditions are updated according to the equations (2.1) - (2.5) together with the conservation laws through the Lagrangian step. The Lagrangian step is a common predictor-corrector method in which the solution at the next time step is predicted using the Euler method and corrected with the trapezoidal rule. The method is second order in both space and time.

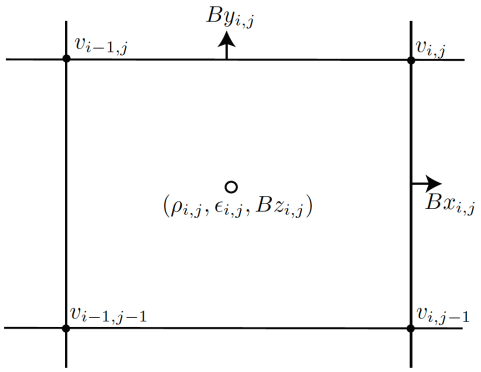

Figure 2.2.1: Two-dimensional grid cell in *LareXD*. Courtesy of *Arber et al.* [2001].

2.5-D simulations of KH waves have been performed. Initial conditions and normalisations of the 2.5-D KH wave simulations will be given in Chapter 4 (Section 4.2.1). 3-D simulations of KH waves and 2-D simulations of the tearing instability have also been performed, reproducing main features of the KH waves and plasmoids respectively, but will not be reported here for the sake of brevity.

Chapter 3

Four-spacecraft Techniques

This Chapter presents four-spacecraft techniques that will be applied onto simulations (Part II) and observations (Part III). They are Magnetic Curvature Analysis (Section 3.1), curlometer for the vorticity calculation (Section 3.2), and multi-spacecraft timing (Section 3.3). Remarks on the errors of the four-spacecraft techniques are also given here (Section 3.4).

3.1 Magnetic Curvature Analysis

Magnetic curvature can be used to determine the local geometry of a magnetic structure. It is proportional to the magnetic tension force which is fundamental to plasmas. The curvature of a magnetic field can be obtained from the change of the magnetic field direction within the curved length as illustrated in Figure 3.1.1, e.g., $\mathbf{C} = \partial\mathbf{b}/\partial S$, where $\mathbf{b} = \mathbf{B}/|\mathbf{B}|$ and dS is the length of the curve on which the magnetic field direction changes. This quantity can be rewritten as $(\mathbf{b}\cdot\nabla)\mathbf{b}$ where $\nabla\mathbf{b}$ can be obtained using the linear gradient estimations. Magnetic curvature has been calculated to determine local magnetic structures since the four-spacecraft observations became available. *Runov et al.* [2003] determined $(\mathbf{b}\cdot\nabla)\mathbf{b}$ in the Cluster observation of a current sheet near the magnetic X-line in the magnetotail. *Shen et al.* [2003] developed Magnetic Curvature Analysis (MCA) technique by deriving it from the magnetic tension force, $(\mathbf{B}\cdot\nabla)\mathbf{B}$, to obtain the curvature radius, curvature directions, and normal of the osculating planes (the planes that contain the curves) of the magnetotail current sheet and neutral sheet. Motivated by the complex magnetic geometry induced by KH instability, we are utilising the MCA technique in the analyses of the magnetopause KH waves.

Shen et al. [2003] have given the formula,

$$C_j = B^{-2}\sum_i B_i\nabla_i B_j - B^{-4}B_j\sum_{i,l} B_i B_l \nabla_i B_l \tag{3.1}$$

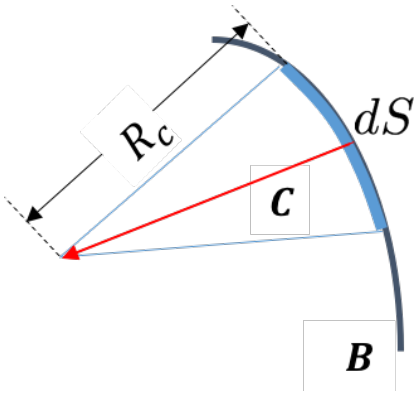

Figure 3.1.1: Differential geometry of the magnetic field curvature.

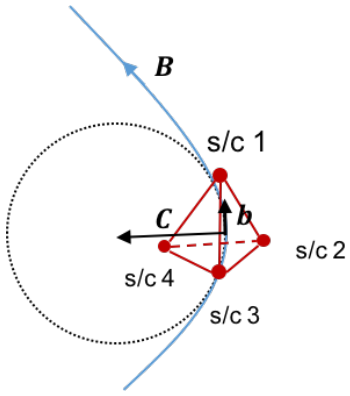

Figure 3.1.2: Magnetic curvature at the tetrahedron barycentre.

where i, j, k represent the vector components, e.g., in the Cartesian coordinates $i, j, k \in \{x, y, z\}$, $B = |\mathbf{B}|$ is the average magnetic field at the tetrahedron barycentre, and $\nabla_i B_j$ are the magnetic field gradient tensors at the barycentre. This formula yields the magnetic curvature vector (**C**) at the tetrahedron barycentre as shown in Figure 3.1.2.

The derivation of the formula (3.1) is given by *Vogt et al.* [2008] as follows. Magnetic tension force (**T**) can be expressed as

$$\mathbf{T} = \mathbf{B} \cdot \nabla \mathbf{B} \tag{3.2}$$

which can be split into perpendicular and parallel components to the magnetic field lines,

$$\mathbf{B} \cdot \nabla \mathbf{B} = (\mathbf{B} \cdot \nabla) B\mathbf{b} = B^2 \mathbf{b} \cdot \nabla \mathbf{b} + \mathbf{b}(\mathbf{B} \cdot \nabla B) = \mathbf{T}_\perp + \mathbf{T}_\parallel \tag{3.3}$$

where $B = |\mathbf{B}|$ and $\mathbf{B} = B\mathbf{b}$. The perpendicular component in (3.3) is proportional to the magnetic curvature which can be rearranged to yield

$$\mathbf{C} = \mathbf{b} \cdot \nabla \mathbf{b} = \frac{\mathbf{B} \cdot \nabla \mathbf{B}}{B^2} - \frac{\mathbf{b}(\mathbf{B} \cdot \nabla B)}{B^2}. \tag{3.4}$$

By writing the parallel component in equation 3.3, the magnetic curvature can be expressed as

$$\mathbf{C} = B^{-2}(\mathbf{B} \cdot \nabla \mathbf{B}) - B^{-4}\mathbf{B}[\mathbf{B} \cdot (\mathbf{B} \cdot \nabla \mathbf{B})]. \tag{3.5}$$

which is equivalent to the expression (3.1). By noting that from differentiation

$$\mathbf{B}\cdot(\mathbf{B}\cdot\nabla\mathbf{B}) = B\mathbf{b}\cdot(B\mathbf{b}\cdot\nabla B\mathbf{b}) = B^2\mathbf{b}\cdot[B(\mathbf{b}\cdot\nabla\mathbf{b})+\mathbf{b}\cdot\mathbf{b}(\nabla B)] = B^2\mathbf{b}\cdot\nabla B = B(\mathbf{B}\cdot\nabla B) \tag{3.6}$$

where $\mathbf{b} \cdot \nabla \mathbf{b} = 0$ for the parallel component term and $\mathbf{b} \cdot \mathbf{b} = 1$, we have shown

that the right hand side terms of equations 3.4 and 3.5 are equivalent.

Using the notation $G_{ij} = \partial_j B_i$, the expression (3.1) becomes

$$C_j = B^{-2} \sum_i B_i G_{ji} - B^{-4} B_j \sum_{i,l} B_i B_l G_{li} \tag{3.7}$$

The linear magnetic gradient (G_{ij}) is a combination of the local magnetic gradient (G^0_{ij}) and the correction term for $\nabla \cdot \mathbf{B} = 0$, e.g.,

$$G_{ij} = G^0_{ij} + \lambda R^{-1}_{ij} \tag{3.8}$$

where R^{-1}_{ij} is the inverse volumetric tensor of the tetrahedron and λ is the Lagrangian multiplier defined by $\lambda = -G^0_{ii}/R^{-1}_{ii}$. The volumetric tensor is given by

$$\mathbf{R} = \frac{1}{4} \sum_{\alpha=1}^{4} (\mathbf{r}_\alpha - \mathbf{r}_\beta)(\mathbf{r}_\alpha - \mathbf{r}_\beta)^T \tag{3.9}$$

where $\mathbf{r}_\alpha$ are the position vectors of the spacecraft $\alpha \in \{1, 2, 3, 4\}$ and $\mathbf{r}_\beta = \frac{1}{4} \sum_{\alpha=1}^{4} \mathbf{r}_\alpha$ is the barycentre of the tetrahedron. Note that the volumetric tensor is not invertible when the four spacecraft are co-planar. The local magnetic gradient can be obtained from either through the minimisation using the least squares method [*Harvey*, 1998] or the linear barycentric estimator [*Chanteur*, 1998]. Here we choose the linear barycentric method due to its convenience, such that

$$G^0_{ij} = \sum_{\alpha=1}^{4} B_{\alpha i} k_{\alpha j} \tag{3.10}$$

where k_α is the reciprocal vectors given by $\mathbf{k}_\alpha = (\mathbf{r}_{\beta\gamma} \times \mathbf{r}_{\beta\lambda})/(\mathbf{r}_{\beta\alpha} \cdot \mathbf{r}_{\beta\gamma} \times \mathbf{r}_{\beta\lambda})$, where $\mathbf{r}_{\alpha\beta} = \mathbf{r}_\beta - \mathbf{r}_\alpha$ are relative spacecraft position vectors, and $(\alpha, \beta, \gamma, \lambda)$ must be a cyclic permutation of $(1, 2, 3, 4)$. Note that the reciprocal vectors are related to the volumetric tensor [*Chanteur and Harvey*, 1998] such that

$$\mathbf{R}^{-1} = 4\mathbf{K}, \qquad \mathbf{K} = \sum_{\alpha=1}^{4} \mathbf{k}_\alpha \mathbf{k}^T_\alpha. \tag{3.11}$$

Note that **R** and **K** are symmetric tensors.

The curvature radius is obtained from $R_c = 1/|\mathbf{C}|$. A curvature radius is typically used to estimate the scale size of the structure. *Shen et al.* [2003] use the minimum of the curvature radius, $R_{c,min}$, to estimate the characteristic half-thickness of the neutral sheet. The error of the method is of order $(a/D)^2$ where a is the average inter-spacecraft separation or the tetrahedron size, e.g., $\langle |\mathbf{r}_\beta - \mathbf{r}_\alpha| \rangle$, and D is the characteristic scale size of the structure which is typically $\sim R_c$.

3.2 Curlometer

The curlometer technique is used to calculate a curl of a vector field, e.g., $\nabla \times \mathbf{B}$ and $\nabla \times \mathbf{V}$ where **B** and **V** are the magnetic and velocity fields respectively. The method is developed by *Dunlop et al.* [1988] to estimate a current density from the four-spacecraft tetrahedron. Using the Ampere's Law (neglecting the displacement current) in the integral form, one can estimate the current density through each face of the tetrahedron, e.g.,

$$\mu_0 \iint_A \mathbf{J} \cdot \mathbf{dS} = \oint_C \mathbf{B} \cdot \mathbf{dl} \tag{3.12}$$

where A is the face of the tetrahedron and C is the triangular path around the face. Given the spacecraft $1, 2, 3$ surrounding a tetrahedron face A with inter-spacecraft separation vectors $\mathbf{r}_{ij}$ where $i, j \in \{1, 2, 3\}$, equation (3.12) reads

$$\mu_0 J_{ijk} \frac{|\mathbf{r}_{ji} \times \mathbf{r}_{jk}|}{2} = \langle \mathbf{B} \rangle_{ij} \cdot \mathbf{r}_{ij} + \langle \mathbf{B} \rangle_{ik} \cdot \mathbf{r}_{ik} + \langle \mathbf{B} \rangle_{jk} \cdot \mathbf{r}_{jk} \tag{3.13}$$

where $\langle \mathbf{B} \rangle_{ij} = (\mathbf{B}_i + \mathbf{B}_j)/2$, assuming a linear variation of **B** between the spacecraft. The total current density is then found by summing the equation (3.13) for all the faces of the tetrahedron. Practically, we can treat one of the four spacecraft as a reference point to simplify the equation (3.13). An alternative method which is more convenient is the linear barycentric estimator using the reciprocal vectors as utilised in Section 3.1. *Chanteur* [1998] has given the formula

$$\nabla \times \mathbf{V} = \sum_{\alpha=1}^{4} \mathbf{k}_\alpha \times \mathbf{V}_\alpha \tag{3.14}$$

where $\mathbf{k}_\alpha$ is the reciprocal vector of the individual spacecraft-α and $\mathbf{V}_\alpha$ is the vector field measured at the spacecraft-α. The equation (3.14) is equivalent to summing of the equation (3.13) of all the tetrahedron face. This can be illustrated in Figures 3.2.1 and 3.2.2, e.g., the vorticity at spacecraft 4 is $\Omega_4 = \mathbf{k}_4 \times \mathbf{V}_4$, where $\mathbf{k}_4 = (\mathbf{r}_{12} \times \mathbf{r}_{13})/(\mathbf{r}_{14} \cdot \mathbf{r}_{12} \times \mathbf{r}_{13})$, and the total vorticity is the sum of the individual vorticities.

The ratio $Q = |\nabla \cdot \mathbf{B}|/|\nabla \times \mathbf{B}|$ has been used to monitor the quality of the estimation because, ideally, $\nabla \cdot \mathbf{B}$ should be zero. However, since $\nabla \cdot \mathbf{B}$ is subject to the same constraints as $\nabla \times \mathbf{B}$ when calculating it, this ratio is not necessarily meaningful and cannot always be used to represent the quantitative error of the current estimation [*Robert et al.*, 1998]. Indeed, a large value of $\nabla \cdot \mathbf{B}$ can arise from the physical nonlinearity [*Robert et al.*, 1998]. The technique underestimates the current density when the tetrahedron size is larger than the cross-section of the line currents [*Forsyth et al.*, 2011]. Applications and efficiencies of the curlometer

technique in various plasma structures and magnetospheric environments have been summarised by *Dunlop and Eastwood* [2008] and *Dunlop et al.* [2016].

3.3 Multi-spacecraft Timing

Multi-spacecraft timing (also called triangulation) is a method for finding the normal direction and the speed of a one-dimensional boundary crossing. The method is based on the assumption that the boundary can be considered as a plane. This criterion is usually satisfied when the scale size of the four-spacecraft is much smaller than the scale size of the planar structure. The method is developed by *Russell et al.* [1983] for determining orientations of the shock normals. The formula for 4-spacecraft [e.g., *Schwartz*, 1998] is given by

$$(\mathbf{r}_\alpha - \mathbf{r}_4) \cdot \mathbf{n} = V(t_\alpha - t_4), \qquad \alpha \in \{1, 2, 3\} \tag{3.15}$$

where $\mathbf{r}_\alpha$ is the position vectors of the spacecraft-α, t_α is the timestamp for a boundary crossing at the spacecraft-α, $\mathbf{n}$ is the normal vector of the surface boundary, and V is the speed of the boundary. Here the spacecraft-4 is taken as a reference. Using the Cartesian coordinates, (3.15) can be explicitly written as

$$\begin{pmatrix} r_{14x} & r_{14y} & r_{14z} \\ r_{24x} & r_{24y} & r_{24z} \\ r_{34x} & r_{34y} & r_{34} \end{pmatrix} \begin{pmatrix} n_x \\ n_y \\ n_z \end{pmatrix} = V \begin{pmatrix} t_{14} \\ t_{24} \\ t_{34} \end{pmatrix} \tag{3.16}$$

where $(\mathbf{r}_\alpha - \mathbf{r}_4)$ in (3.15) is expressed as $(r_{\alpha x} - r_{4x}, r_{\alpha y} - r_{4y}, r_{\alpha z} - r_{4z}) = (r_{\alpha 4x}, r_{\alpha 4y}, r_{\alpha 4z})$, $\mathbf{n} = (n_x, n_y, n_z)$ is a unit column vector of the normal ($|\mathbf{n}| = 1$), and $t_{\alpha 4} \equiv t_\alpha - t_4$ is a column vector of the time-lags of the boundary between the spacecraft . Let

$$D \equiv \begin{pmatrix} r_{14x} & r_{14y} & r_{14z} \\ r_{24x} & r_{24y} & r_{24z} \\ r_{34x} & r_{34y} & r_{34z} \end{pmatrix}, \quad \mathbf{m} = \frac{1}{V} \begin{pmatrix} n_x \\ n_y \\ n_z \end{pmatrix} \equiv \frac{\mathbf{n}}{V}, \quad T = \begin{pmatrix} t_{14} \\ t_{24} \\ t_{34} \end{pmatrix}$$

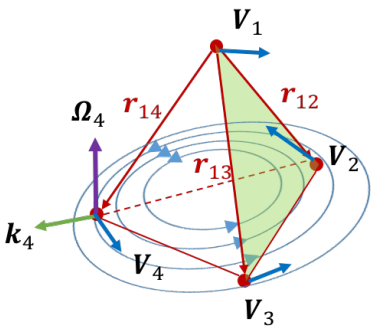

Figure 3.2.1: Vorticity at s/c 4

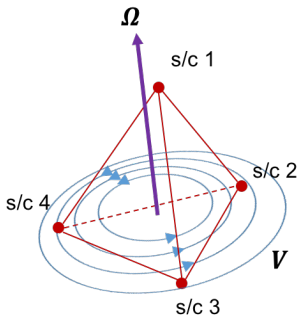

Figure 3.2.2: Vorticity Technique

where D is an invertible 3×3 matrix and T is a linear array. The normal direction $\mathbf{n}$ and the boundary speed V can be resolved in the expression

$$D\mathbf{n} \;=\; VT \tag{3.17}$$

such that

$$\mathbf{m} \;=\; \frac{\mathbf{n}}{V} = D^{-1}T, \quad \text{where } \det D \neq 0, \quad \mathbf{n} = \frac{\mathbf{m}}{|\mathbf{m}|}, \quad V = \frac{1}{|\mathbf{m}|}. \tag{3.18}$$

This technique has been commonly used in multi-spacecraft observations of the passages of discontinuities not limited to shocks. Errors of the method are dependent on the quality of the tetrahedron formation and the speed of the discontinuity relative to the spacecraft [*Zhou et al.*, 2006].

An analysis of the four-spacecraft technique and a single-spacecraft method known as the centre of mass velocity were carried out in the first year of the PhD studies but will not be reported here for the sake of brevity.

3.4 Remarks on the errors of four-spacecraft techniques

Several factors contribute to the errors of quantities that are derived from the four-spacecraft techniques. At the basic level, there are measurement errors or systematic errors that arise from the magnetic field, plasma moment, and spacecraft position measurements. For Cluster mission, error from the measurements arises from a number of sources, but overall the error is a few percent or less [*Paschmann et al.*, 1998]. Errors of the spacecraft positions are in the order of 1 km at apogee and less than this value away from the apogee towards perigee [*Volpp and Sieg*, 2010]. Specifically to a four-spacecraft tetrahedron, there are geometrical errors that arise from the tetrahedron formation deviated from the regular configuration, which is sometimes unavoidable considering limitations in the control of the orbital motions of the spacecraft. Another crucial factor is the variations of the physical structures. Since we assume linear variations of the quantities to obtain the gradients, the error then arises from the non-linear variations. The error from the non-linear variations is typically at second order (e.g., as in Taylor's expansion) and is therefore called a `truncation error'. The truncation error is minimal when the spacecraft separation is much smaller than the scale size of the structure. However, the sensitivity of four-spacecraft-derived quantities to the physical structures is often complex depending on the nature of the specific structures, and this deserves particular considerations.

We limit our attention to the sensitivity of the scale sizes of the spacecraft

tetrahedron with respect to the scale sizes of the structures. Given that the measurement and geometrical errors are small, the impacts of the relative scales can be discussed. The impacts of the relative scales would be essential to understanding the four-spacecraft outputs as the physical structures can exhibit complex variations. Such considerations tailored to specific plasma structures, e.g., surface boundary waves and flux ropes, are useful to understand four-spacecraft observations in multi-scales.

Part II

Four-spacecraft Applications to MHD Simulations

Chapter 4

Four-spacecraft Magnetic Curvature and Vorticity Analyses on Kelvin-Helmholtz Waves in MHD Simulations

[Results in this Chapter have been published in JGR (Space Physics), vol. 123, as *Kieokaew et al.* [2018a], and IAU symposium proceedings, no. 335, as *Kieokaew et al.* [2018b].]

Four-spacecraft missions are probing the Earth's magnetospheric environment with high potential for revealing spatial and temporal scales of a variety of in-situ phenomena. The techniques allowed by these four spacecraft include the calculation of vorticity and the MCA, both of which have been used in the study of various plasma structures. In this Chapter, we will investigate the robustness of the MCA and vorticity analysis techniques when increasing (regular) tetrahedron sizes, to interpret real data. Here, for the first time, we will test both techniques on a 2.5D MHD simulation of KH waves at the magnetopause. We will investigate in particular the curvature and flow vorticity across KH vortices and produce time series for static spacecraft in the boundary layers. It will be shown that the combined results of magnetic curvature and vorticity further help us to understand the development of KH waves. In particular, first, in the trailing edge, the magnetic curvature across the magnetopause points in opposite directions, in the wave propagation direction on the magnetosheath side and against it on the magnetospheric side. Second, the existence of a `turnover layer' in the magnetospheric side, defined by negative vorticity for the duskside magnetopause, which persists in the saturation phase, is reminiscent of roll-up history. The MCA measures will be shown to have significant variations depending on the size of the tetrahedron. This Chapter lends support for cross-scale observations to better understand the nature of curvature

and its role in plasma phenomena.

4.1 Introduction

Four-spacecraft missions provide a unique opportunity to study plasma phenomena in the Earth's magnetospheric environments with high potential for resolving spatio-temporal fluctuations. The Earth's magnetosphere outer boundary, the magnetopause, is the site of plasma processes that allow the entry of solar wind plasma to the magnetosphere. Depending on the interplanetary magnetic field (IMF) configuration, mechanisms that can operate at this boundary are different. Kelvin-Helmholtz (KH) instabilities, arising from a shear flow at the interface, are believed to be common under northward IMF conditions. Numerous observations have been studied by the four-spacecraft Cluster [*Escoubet et al.*, 2001] and recently the Magnetospheric Multiscale (MMS) missions [*Burch et al.*, 2015]. KH instabilities have been proposed as a candidate mechanism for the penetration of solar wind plasma, the widening of the low latitude boundary layer (LLBL), and the triggering of ultra-low-frequency (ULF) waves. Solar-wind plasma entry is possible via magnetic reconnection [e.g., *Nykyri and Otto*, 2001] and turbulence [e.g., *Matsumoto and Hoshino*, 2004] inside rolled-up KH vortices. Analyses of KH events at the magnetopause help us to understand the evolution and mechanisms associated with the waves.

There are two approaches to study KH waves at the magnetopause. Particle distributions are commonly used to reveal particle mixing inside KH vortices [e.g., *Nishino et al.*, 2007; *Taylor and Lavraud*, 2008]. Lower-density and faster-than-sheath (LDFTS) plasma is a distinct signature associated with rolled-up KH vortices [*Takagi et al.*, 2006]. However, other contributing factors such as the presence of a plasma depletion layer (PDL) can mimic the features of the LDFTS plasma [*Plaschke et al.*, 2014]. Investigations of surface boundary geometry, on the other hand, are less common. Periodic surface wave analysis can be used to sketch the spatial structures straightforwardly from time series of KH waves [*De Keyser and Roth*, 2003]. Grad-Shafranov-like (GS-like) reconstruction developed by *Sonnerup et al.* [2006] is used to reconstruct streamlines surrounding the spacecraft path of a plasma flow transverse to the magnetic field structure of KH waves [e.g., *Hasegawa et al.*, 2007]. Multi-spacecraft timing analysis [*Russell et al.*, 1983] has been used to determine the magnetopause boundary inclinations during surface wave passages in the four-spacecraft Cluster [*Owen et al.*, 2004; *Foullon et al.*, 2008] and MMS data [*Plaschke et al.*, 2016]. A steeper leading edge than the trailing edge is expected for KH waves. The method requires the boundary to be planar within the spacecraft separation, which may not always be satisfied for the surface wrapping around KH vortices.

Magnetic curvature is intrinsic to curved magnetic fields which possess magnetic tension. Magnetic curvature calculated from in-situ measurements has been resolved by the four-spacecraft technique called ``magnetic curvature analysis'' (MCA) [*Shen et al.*, 2003]. The method applies magnetic field gradient tensors which can be found either through the least-squares minimisation [*Harvey*, 1998] or the barycentric method [*Chanteur*, 1998]. To extend the idea of the surface wave analysis to three-dimensional, non-planar structures such as KH waves, we aim to explore the applicability of MCA. The method yields the magnetic curvature which, by definition, points in the direction of the magnetic tension force. The reciprocal of the curvature the so-called `curvature radius' can be used to estimate the scale size of the magnetic structure. The method has been applied to Cluster observations of current sheets [e.g., *Runov et al.*, 2006; *Shen et al.*, 2008], plasmoids [e.g., *Zhang et al.*, 2013], ring current [e.g., *Shen et al.*, 2014], and magnetic flux ropes [e.g., *Yang et al.*, 2014]. Particle pitch angle scattering is inferred from magnetic curvature in magnetic reconnection sites in the ion diffusion regions [e.g., *Zhang et al.*, 2016] and in the electron diffusion regions [e.g., *Lavraud et al.*, 2016; *Cao et al.*, 2017].

Magnetic fields threading through KH waves may form complex three-dimensional configurations. Three-dimensional kinetic simulations show that compressed current sheets along the KH wave trailing edges can reconnect, giving rise to magnetic flux ropes over a range of oblique angles between the wave propagation and the magnetic field lines [*Nakamura et al.*, 2013]. These flux ropes propagate with the shear flow and later merge with parent vortices. Some observations suggest mid-latitude reconnection of three-dimensional field lines interweaving through KH waves at the equatorial plane [*Bavassano Cattaneo et al.*, 2010]. Statistical studies on MMS observations by *Vernisse et al.* [2016] show that this process can allow plasma entry even though the KH instability remains in its linear stage. Three-dimensional simulations show that magnetic field lines connecting between the southern and northern hemispheres can be twisted by the vortical flows at the equatorial plane, creating a favourable condition for reconnection at mid-latitudes [*Faganello et al.*, 2012a; *Leroy and Keppens*, 2017]. Resolving magnetic curvature of KH waves may help in understanding distortion of Earth's magnetic field lines between low and high latitudes, and consequently how they may reconnect with the magnetosheath magnetic field.

Vorticity is intrinsic to any flow system that exhibits swirling patterns such as vortical flows in KH vortices. Despite that, in-situ vortical flow studies in magnetospheric environments are limited. Four spacecraft make it possible to resolve vorticity $\Omega = \nabla \times \mathbf{V}$, where $\mathbf{V}$ is the velocity field, using either the least squares method [*Harvey*, 1998] or the barycentric estimator [*Chanteur*, 1998]. Vorticity in observed KH events has been resolved in three-spacecraft measurements by THEMIS and

Cluster by *Shen et al.* [2012]. This work further suggests that pulsed-enhanced periodic vorticity can be the signature of rolled-up KH waves. Using global MHD simulations, *Collado-Vega et al.* [2013] studied plasma vortices (quantified with a velocity gradient tensor) under various IMF clock angles and solar wind speeds, and found that the majority of vortices are consistent with a KH instability origin. KH vortices in the large plasma device (LAPD) experiment have been probed and characterised by an array of Langmuir probes [*Horton et al.*, 2005]. In addition, vorticity may be important in studies of turbulence [e.g., *Consolini et al.*, 2015], magnetic reconnection [e.g., *Phan et al.*, 2016], and plasma heating [e.g., *Parashar and Matthaeus*, 2016].

Due to the fact that the scale size of structures of interest should be much larger than that of the spacecraft tetrahedron, the Cluster mission (inter-spacecraft separation between 100 km and 18000 km) is suitable for macrophysics of magnetohydrodynamics whereas the MMS (inter-spacecraft separation between 10 km and 400 km) is suitable for microphysics of plasma kinetic theory. For techniques that resolve geometrical parameters such as MCA, tetrahedron size impact should be discussed. The robustness of four-spacecraft methods is dependent on size, elongation, and planarity of the tetrahedron shape; quantified as the so-called `tetrahedron geometrical factors' by *Robert et al.* [1998]. Since the gradient estimation is based on a first-order approximation, e.g., assuming the physical linearity, the relative error increases as the tetrahedron size becomes bigger. Tetrahedron size impacts have been studied in various four-spacecraft tools such as the $k-$filtering technique for plasma turbulence studies [*Sahraoui et al.*, 2010] and the first-order Taylor expansion (FOTE) for finding magnetic nulls [*Fu et al.*, 2015]. Highly irregular shapes of tetrahedron (e.g., almost planar or highly elongated) result in large errors ($> 10\%$) of the current density [*Robert et al.*, 1998], as estimated from the curlometer technique [*Dunlop et al.*, 1988].

We propose to combine four-spacecraft techniques for magnetic curvature and vorticity analyses in KH studies. We first present a resistive MHD simulation of KH waves at the Earth's flank magnetopause in Section 4.2.1 and then the application of the four-spacecraft analyses in Section 4.3. The spatial studies in Section 4.4.1 and temporal studies in Section 4.4.2 are done using virtual spacecraft at typical Cluster scale-sizes. These studies provide the basis for sketching local magnetic field and flow geometries around a spacecraft trajectory. Effects of the varying spacecraft tetrahedron size are examined in the spatial studies in order to test the robustness of the methods. We finally summarise and discuss potential applicability of MCA and vorticity techniques in Section 4.5.

4.2 Simulation

4.2.1 Initial conditions of 2.5-D simulation

We simulate the Kelvin-Helmholtz instability using *Lare2d*, a Lagrangian-step resistive MHD code with a staggered grid in 2.5-D [*Arber et al.*, 2001]. The simulation reproduces Kelvin-Helmholtz waves for typical conditions along the Earth's flank magnetopause on the duskside.

Normalisation values are the following. The normalisation length $L_0 = 600\times10^3$ m ($= 600$ km), time $t_0 = 4$ s, the speed $v_0 = L_0/t_0 = 150 \times 10^3$ m s^{-1} ($= 150$ km s^{-1}). The normalisation ion density $n_0 = 10\times10^{-6}$ m^{-3} ($= 10$ cm^{-3}), magnetic field $B_0 = v_0\sqrt{\mu_0 m_p n_0} = 21.7$ nT, and temperature $T_0 = 2.7 \times 10^6$ K. The background resistivity η is set to zero as the magnetospheric plasmas are collisionless. The anomalous resistivity η_0 is set as the inverse Lundquist number of value $1e-11$ which is the default value in the codes. The anomalous resistivity is triggered when the critical value of current density of $J_c = 1.1J_0 = 28.8$ nA m^{-2} is reached. Discussions on these specifications of the resistivity are given in Section 2.2 of Chapter 2. Magnetic reconnection may occur in this simulation but it is not the focus of our study.

The simulation box is of the size $80 \times 60\ L_0^2$ which corresponds to $7.5 \times 3.8\ R_E^2$. The grid resolution is $N_x \times N_y = 320\times160$, hence each cell covers $L_0/4\times L_0/4$ km^2. The chosen cell length of $L_0/4 = 150$ km corresponds to $2-3$ ion inertial lengths at the magnetopause and therefore the simulation is not adequate for Cluster separations of 100 and 200 km. The XY-plane of the simulation represents the equatorial-GSM plane with the X-axis directed sunward. The simulation domain is periodic in the X-direction and open in the Y-direction.

Let the subscripts $1, 2$ represent magnetosheath and magnetospheric sides respectively. The parameter profiles are given by

$$n = (n_1+n_2)/2 + (n_1-n_2)\tanh[(y-y_0)/\Delta w])/2 \quad (4.1)$$

$$B = (B_1+B_2)/2 + (B_1-B_2)\tanh[(y-y_0)/\Delta w])/2 \quad (4.2)$$

$$T = (T_1+T_2)/2 + (T_1-T_2)\tanh[(y-y_0)/\Delta w])/2 \quad (4.3)$$

$$V = -V_1(\tanh[(y-y_0)/\Delta w]+1)/2 \quad (4.4)$$

where y_0 is the mid-plane Y position and $\Delta w = L_0$ is the width of the boundary layer. The boundary layer and current sheet are centred and co-located for simplicity. The initial simulation parameters are the magnetic field strength $B_1 = B_2 = 0.92B_0$, ion density $n_1 = n_0, n_2 = 0.1n_0$, ion speed $V_1 = 2.0v_0$, and temperature $T_1 = 0.85T_0, T_2 = 9.8T_0$. Note that the temperature T is not a free parameter and it must be calculated to balance the total plasma and magnetic pressures at the mid-plane. The flow velocity $\mathbf{V} = (V, \delta V, 0)$ is initially defined

mainly in the X-direction with a small transverse perturbation in the Y-direction. The velocity component $V_x = V$ has a hyperbolic tangent profile in the Y-direction (see equation 4.4) while the velocity component $V_y = \delta V$ (the perturbation) has a sinusoidal profile with 10% strength of the V_x. The KH wavelength is defined by the initial sinusoidal perturbation δV which is a half of the box length ($\lambda_{KH} = 40L_0$). The chosen wavelength of $40L_0$ is a convenient choice to fit two wavelengths for the simulation box size of $80L_0 \times 40L_0$ and thus to visualise one wavetrain (one wavelength) into context (another λ split on either side). The Alfvén Mach number is 1.49 using the initial velocity jump of 300 km s^{-1} and the Alfvén speed of 202 km s^{-1}. The plasma beta is not available in the code because the plasma pressure is normalised to the magnetic pressure. The initial magnetic field is given by $\mathbf{B} = B(\sin\varphi, 0, \cos\varphi)$, $\varphi = 10^o$, making an angle of $90^o - \varphi$ with the flow direction. The given initial magnetic field with a small component B_x is common for magnetopause KH wave studies as the IMF can be tilted away from the geomagnetic north while propagating down the flanks. The magnetic field strength and orientation are quite similar to KH observations, e.g., for the 20 November 2001 event of *Foullon et al.* [2008] which will be presented in Chapter 5.

To obtain the KH growth rate from the linear theory, the expression 1.3 may be rewritten in terms of φ angle and with the wavevector $\mathbf{k} = k\mathbf{x}$ for this problem [*Otto and Fairfield*, 2000], as

$$\gamma/k = \left[\alpha_1\alpha_2 V_1^2 \cos^2\varphi - (\alpha_1 V_{A,1}^2 + \alpha_2 V_{A,2}^2)\sin^2\varphi\right]^{1/2} \tag{4.5}$$

where $\alpha_1 = n_1/(n_1+n_2)$ and $\alpha_2 = n_2/(n_1+n_2)$, and $V_{A,1}, V_{A,2}$ label the Alfvén speeds in the X-direction on either side of the boundary. The calculation yields the growth rate of $\gamma/k = 78$ km s^{-1}. For comparison, *Otto and Fairfield* [2000] found a similar growth rate using empirical inputs from their Geotail observations of KH waves in the magnetospheric context.

Physically, the simulated KH event lasts $150t_0$ = 600 seconds, with a repetition period of $25t_0 = 100$ seconds (frequency 10 mHz). The wave phase speed is 241 km.s^{-1}. This is between the linear theory prediction of KH wave group speed which is the boundary centre-of-mass (CM) velocity $\mathbf{V}_{\text{cm}} = (n_1\mathbf{V}_1 + n_2\mathbf{V}_2)/(n_1 + n_2) = 273$ km.s^{-1} and the average velocity $\mathbf{V}_{\text{avg}} = (\mathbf{V}_1 + \mathbf{V}_2)/2 = 150$ km.s^{-1}, consistent with the prediction of KH wave speed for a finite-thickness shear layer [*Hasegawa et al.*, 2009]. The KH wavelength is $3.7\ R_E$, consistent with observed events where the KH wavelengths vary from a few R_E to $\sim 10\ R_E$ [e.g., *Taylor et al.*, 2012; *Lin et al.*, 2014]. We analyse up to 6 back and forth boundary motions of this wave from linear to non-linear stages.

4.2.2 Example of 3-D Simulation

To ascertain the relevance of 2.5-D simulation for our purpose, we explore numerically extensive simulations of MHD KH waves in 3-D using *Lare3D* codes. A simplest set-up is to duplicate the initial conditions of the 2.5-D simulation in Section 4.2.1 along the Z-direction. The set-up using *Lare3D* codes is as follows.

The simulation box is of the size $L_x \times L_y \times L_z = 80 \times 40 \times 40\ L_0^3$. For fast numerical calculation, we assign only one computation node per one grid cell cube. The simulation box applies the GSM coordinates with the X-axis directed sunward and the Z-axis directed along the Earth's magnetic dipole. The simulation domain is periodic in the X and Z directions, and open in the Y-direction.

Let the subscripts $1, 2$ represent magnetosheath and magnetospheric sides, respectively. The initial conditions are given by

$$n_0(x,y,z) = (n_1+n_2)/2 + (n_1-n_2)\,\mathsf{tanh}[(y-y_0)/\Delta w])/2 \quad (4.6)$$

$$T_0(x,y,z) = (T_1+T_2)/2 + (T_1-T_2)\,\mathsf{tanh}[(y-y_0)/\Delta w])/2 \quad (4.7)$$

$$V_{x,0}(x,y,z) = -V_1(\mathsf{tanh}[(y-y_0)/\Delta w]+1)/2 \quad (4.8)$$

$$V_{y,0}(x,L_y/2,z) = a\,\mathsf{sin}(4\pi x/L_x) \quad (4.9)$$

$$\mathbf{B}_0(x,y,z) = B_0(\mathsf{sin}\,10^o, 0, \mathsf{cos}\,10^o) \quad (4.10)$$

where $\Delta w = L_0$ is the width of the boundary layer. The boundary layer and current sheet are centred and co-located for simplicity. From equations 4.6 - 4.8, one can see that the density, temperature, and velocity profiles only vary along Y-direction. To initiate the KH waves, we gave a small transverse perturbation in velocity at mid-plane $y = L_y/2$ as shown in equation 4.9, where a is the amplitude. Note that this perturbation is also duplicated along the Z-direction, such that the KH waves are initiated at $y = L_y/2$ for $z \in [-L_z/2, L_z/2]$. The magnetic field is directed along the Z-direction with a small component in the X-direction. The simulation results are shown in Figure 4.2.1.

One can see that a certain magnetic field line connects through different phases of the wave in different XY-planes. Magnetic field lines which connect through different phases of the waves further get twisted when the KH waves reach their non-linear stage as seen in right panel of Figure 4.2.1. In the absence of an initial B_x component, a certain magnetic field line would connect through the same phase of the wave in different XY-planes. In this case, the magnetic fields do not get twisted; the fields only `surf' the waves.

4.2.3 Duplication of the 2.5-D Simulation

A duplication of the 2.5-D simulation in Section 4.2.1 along the Z-direction would be equivalent to the 3-D simulation in Section 4.2.2. To support this argu-

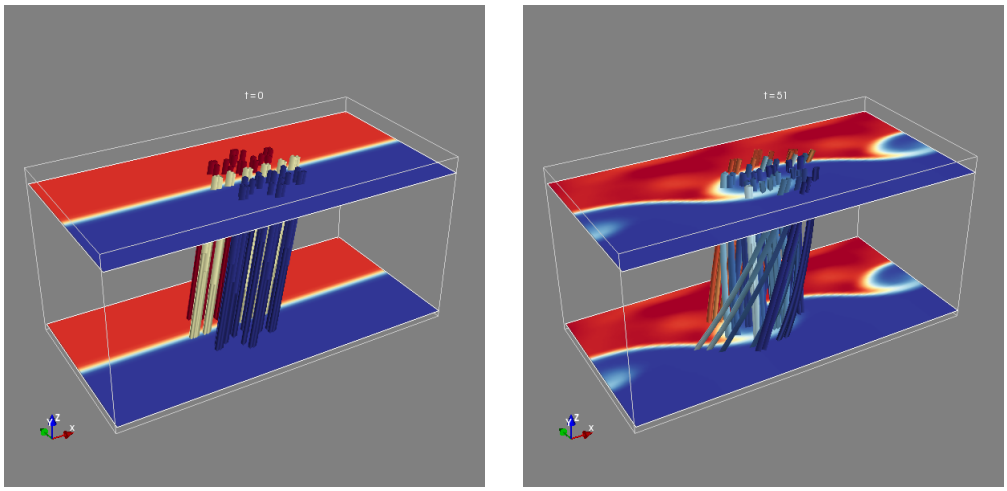

Figure 4.2.1: Snapshots of the 3-D simulation: (left) the initial configuration and (right) the non-linear KH waves. Slabs in the XY-plane show ion density and thick lines connecting between the planes show magnetic field lines with the same colour-code as the ion density. The magnetic field lines connect through different phases of the waves in different XY-plane and wrap around the rolled-up vortex.

ment, we stack up the 2.5-D simulation in panel (a) of Figure 4.4.1 that is simulated using the *Lare2D* codes in the out-of-plane direction for a limited extent. Magnetic field lines are then visualised in Figure 4.2.2. One can see that the orientation of the field lines are consistent with those in the 3-D simulation (see panel (b) of Figure 4.2.1). These results also support the orientation of the field lines that are drawn based on the magnetic curvature results in Chapter 4 in Figure 4.4.2.

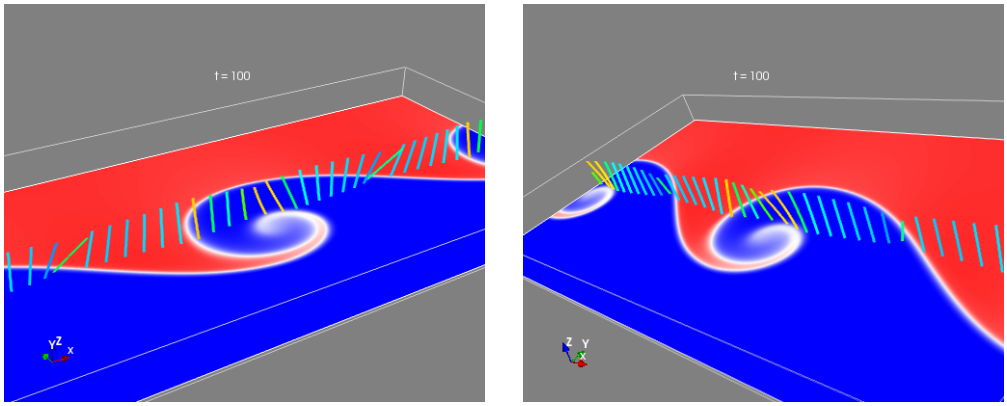

Figure 4.2.2: Visualisation of the duplication of the 2.5D KH simulation produced in Chapter 4 along the Z-direction in two different perspectives. The slab in the X-Y plane shows ion density with the same colour code as in panel (a) of Figure 4.4.1. Magnetic field lines are visualised in the out-of-plane direction. These field lines orientation are consistent with those in the 3-D simulation (panel (b) of Figure 4.2.1). It will also be shown that these are similar to the magnetic curvature results (Figure 4.4.2).

4.3 Four-spacecraft Analyses

We set up virtual probes in a regular tetrahedron configuration and vary the separation size $a = L_0/4, L_0/2, ...$, up to $12L_0$ in the 2.5-D simulation in Section 4.2.1. The virtual probes are labelled by SC1, SC2, SC3, and SC4 with the barycentre in the simulation plane. Note that we have assumed some translation/duplication of the 2D plane in the Z-direction. This is justified with the KH wave because the wave is perturbed in the Y-direction, not in the Z-direction. The calculation is numerically done using 3-D positions of the virtual spacecraft which separate also in the Z-direction, despite all the spacecraft sample values in the same plane. The positions of the four spacecraft are chosen such that their barycentre is in the simulation plane, with three of them (SC1, SC2, SC4) are under and one of them (SC3) is above the simulation plane. The four spacecraft cannot be in the same plane because this will result in a singular matrix (non-invertible matrix) when calculating the volumetric tensor (see equation 3.9).

To calculate the magnetic curvature, we expand $\mathbf{C} = \mathbf{b} \cdot \nabla \mathbf{b}$, where $\mathbf{b} = \mathbf{B}/|\mathbf{B}|$, into

$$C_j = B^{-2} \sum_i B_i G_{ji} - B^{-4} B_j \sum_{i,l} B_i B_l G_{li}, \quad i,j,k \in x,y,z \tag{4.11}$$

as in *Shen et al.* [2003], where $B_i = \sum_{\alpha=1}^{4} B_{\alpha i}/4$ are average magnetic field components from four-spacecraft ($\alpha = 1,2,3,4$) and $G_{ij} = \partial_j B_i$ are magnetic field gradient tensors. The magnetic field gradient tensors are composed of two parts $G_{ij} = G^0_{ij} + \lambda R^{-1}_{ij}$, where the local magnetic gradient tensors (G^0_{ij}) are corrected with the solenoidal constraint ($\nabla \cdot \mathbf{B} = 0$) through the Lagrangian multiplier $\lambda = -G^0_{ii}/R^{-1}_{ii}$ where the volumetric tensors $R_{ij} = \sum_{\alpha=1}^{4} r_{\alpha k} r_{\alpha_j}/4$, for given position vectors $\mathbf{r}_\alpha$ of spacecraft α. In our work, we apply the barycentric method for calculating magnetic gradient tensors $G^0_{ij} = \sum_{\alpha=1}^{4} B_{\alpha i} k_{\alpha j}$ where the reciprocal vectors $\mathbf{k}_\alpha = (\mathbf{r}_{\beta\gamma} \times \mathbf{r}_{\beta\lambda})/(\mathbf{r}_{\beta\alpha} \cdot \mathbf{r}_{\beta\gamma} \times \mathbf{r}_{\beta\lambda})$, $\mathbf{r}_{\alpha\beta} = \mathbf{r}_\beta - \mathbf{r}_\alpha$ are relative position vectors, and $(\alpha, \beta, \gamma, \lambda)$ must be a cyclic permutation of $(1,2,3,4)$. Results of the method are subject to a truncation error from Taylor's expansion, which is of order $(a/D)^2$, where a is the spacecraft separation and D is the scale size of the structure of interest. Note that a relative error a/D to the first order is also used in the literature. We have benchmarked our MCA code against published literature both in Cluster and MMS data.

To calculate the vorticity $\mathbf{\Omega} = \nabla \times \mathbf{V}$, we apply the linear barycentric estimator of curl of vector field given in *Chanteur* [1998] as $\mathbf{\Omega} = \sum_{\alpha=1}^{4} \mathbf{k}_\alpha \times \mathbf{V}_\alpha$. This estimator does not enforce the solenoidality of the vector field which is desirable for our compressible fluid ($\nabla \cdot \mathbf{V} \neq 0$). Errors of the method were explicitly derived by *Vogt and Paschmann* [1998] depending on instrumental errors. These errors were found to be less than 12% for cross products of velocity [*Gurgiolo et al.*, 2010].

A tetrahedron of virtual spacecraft scale size $a = 4L_0$ (MHD scale) is used

for reproducing spatial profiles along the spacecraft trajectory, equivalent to KH observations along the wave propagation direction, and temporal profiles equivalent to observed timeseries by a spacecraft sampling the plasma. For greater visualisation, 2D XY-maps are constructed at a given time from combining multiple spatial X-profiles togeter across the Y-range. These maps constructed from point-by-point measurements are helpful to give a full picture of the curvature and vorticity *in the simulations for this study*, which is informative to understand observational data of KH waves (a first step for future works using real data). The single-spacecraft proxy for identifying rolled-up KH vortices so-called ``lower-density-faster-than-sheath (LDFTS) plasma" [*Takagi et al.*, 2006] is re-visited in order to compare and to identify the stages of vortex development.

4.4 Results

4.4.1 Spatial Studies

Figure 4.4.1 shows the spatial profiles of the selected snapshot ($t = 100t_0$) for the non-linear KH waves exhibiting fully rolled-up vortices. Panel (a) shows the virtual spacecraft by the four yellow points forming a regular tetrahedron configuration of side-length $a = 4L_0$ with the path of its barycentre flying across KH vortices (shown in ion density). To describe general properties along the trajectory, we mark six vertical grey dashed lines by numbers (1) - (6). The yellow box outlines the region of width $1\lambda_{KH} = 40L_0$ for later analyses. The vortex regions, i.e., between (2) and (4), show tenuous ion density from the magnetospheric side in panel (b), with a local increase of mid-value density (between the magnetosheath and magetospheric values) at (3), as seen by SC1 and SC4. This vortex region also shows a local drop in magnetic field component B_z at around (3) in panel (c). The total pressure in panel (d) reaches its maximum around the wave trailing edges, i.e., between (5) and (6), and reaches its minimum in the vortex centre at around (3). The ion velocity field resulting from the simulation is shown in panel (a) with white vectors. This 2-D velocity field is used to obtain the vorticity component Ω_z shown in panel (e), which reaches its maximum around the vortex centre (3). The magnetic curvature radius $R_c = 1/|\mathbf{C}| = 1/\sqrt{C_x^2 + C_y^2 + C_z^2}$ in panel (f) drops to a value of about a half wavelength around the vortex centre (3). The magnetic curvature in panel (g) shows approximately zero curvature at (1) and (4), which corresponds to magnetic field lines perpendicular to the plane ($B_x = B_y \approx 0$ in panel (c)). The leading edge of the rolled-up vortex at (2) shows a positive peak in C_y. The vortex centre (3) shows negative C_x, which apparently gives rise to the small curvature radius in this region. The wave trailing edge between (5) and (6) shows magnetic rotation, marked by a reverse direction of all curvature com-

ponents. Table 4.1 notes explicitly the curvature radius, magnetic curvature, and magnetic field values at locations (1)-(6).

In Figure 4.4.2, we sketch schematic 3D magnetic field lines threading through the KH waves at the equatorial plane based on the values in Table 4.1. The simulated magnetic fields are shown in the equatorial plane $Z = 0$ in GSM coordinates where B_z is shown in greyscale and B_x, B_y are shown as streamlines. The following sketch is consistent with the associated field line orientations (see Figure 4.2.2) and is drawn in a magnetospheric context. Considering that the magnetic field lines are straight initially and connected to the high-latitudes (in the northern and southern hemispheres which are more stable to KH instabilities), 3D magnetic field lines may be drawn as follows. Zero curvatures at (1) and (4) in Table 4.1 correspond to straight magnetic field lines in the magnetosheath (red field line at (1) in Figure 4.4.2) and magnetospheric (blue field line at (4) in Figure 4.4.2) sides respectively. Curvature at (2) which is dominant in positive C_y, with a radius value of $R_c = 0.5\lambda_{KH}$, corresponds to the purple field line at (2) in Figure 4.4.2. Magnetic curvature at this location (shown by green vector) indicates magnetic tension at the boundary layer against the counter-clockwise twist (seen from above) of the vortex. Curvature at (3) which is dominant in negative C_x, with a radius value of $R_c = 0.4\lambda_{KH}$, corresponds to the purple field line at (3) in Figure 4.4.2. The magnetic field line at (3) may be consistent with a sweep of the magnetic field lines that thread through the edge of the KH vortex, e.g., the original field line at the leading edge at location (2), counter-clockwisely into the inner part of the vortex. Curvature radius at (5) is very small, with a value of $R_c = 0.2\lambda_{KH}$, due to a strong perturbation in magnetic curvature in all directions. The region (5) is called `KH spine' in *Otto and Fairfield* [2000] (and also in *Miura* [1984, 1987]; *Wu* [1986]) which is characterised by a strong reduction of B_z and typical extrema in B_x, B_y with opposite polarity. Magnetic curvature in this region points in positive X-direction and negative Y-direction as indicated by a green vector at (5), consistent with the dragging of plasma along the boundary region into the vortex. Magnetic curvature at (6), in contrast, points in the opposite direction to that of (5) with a smaller curvature magnitude (larger curvature radius). From (5) to (6), the magnetic field rotates by $\sim 180^o$, presumably due to different inertia on both sides of the boundary layer (with higher inertia on the magnetosheath side due to denser ion population). We then investigate the tetrahedron size effects in details at the locations (2), (3), and (5) as follows.

We apply the MCA and vorticity techniques using tetrahedrons of varying sizes and with their barycentres located at three different positions in the KH vortex. Figure 4.4.3 shows curvature radius (left column panels), curvature direction (middle), and vorticity magnitude (right). The values for the leading (top row panels), inner (middle), and trailing edges (bottom) of the KH vortex are shown at the locations

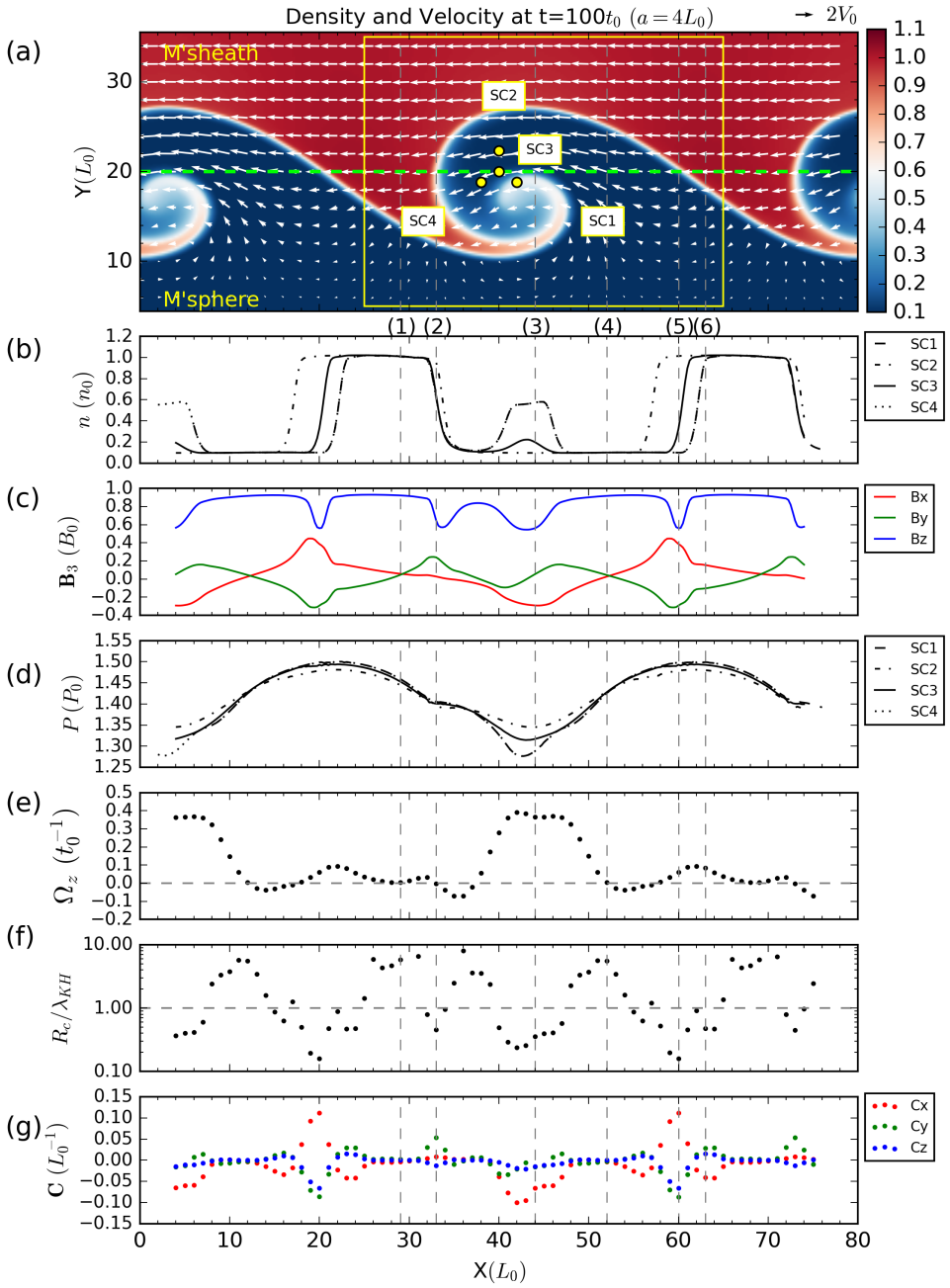

Figure 4.4.1: Spatial profiles of the non-linear KH waves. (a) KH vortices shown in ion density, over-plotted by velocity field (white vectors), with the four-spacecraft configuration of a regular tetrahedron of side-length $a = 4L_0$ (yellow dots) (SC1 (right), SC2 (top), SC3 (middle), and SC4 (left)), and the spacecraft trajectory (green dash) through the mid-plane. The following panels are parameter profiles along the spacecraft trajectory shown in panel (a). (b) Ion density at SC1-SC4, (c) magnetic field at SC3, (d) total pressure at SC1-SC4, (e) flow vorticity, (f) magnetic curvature radius, and (g) curvature vector components. The yellow box in panel (a) outlines the region for analyses in Figures 4.4.5 and 4.4.7.

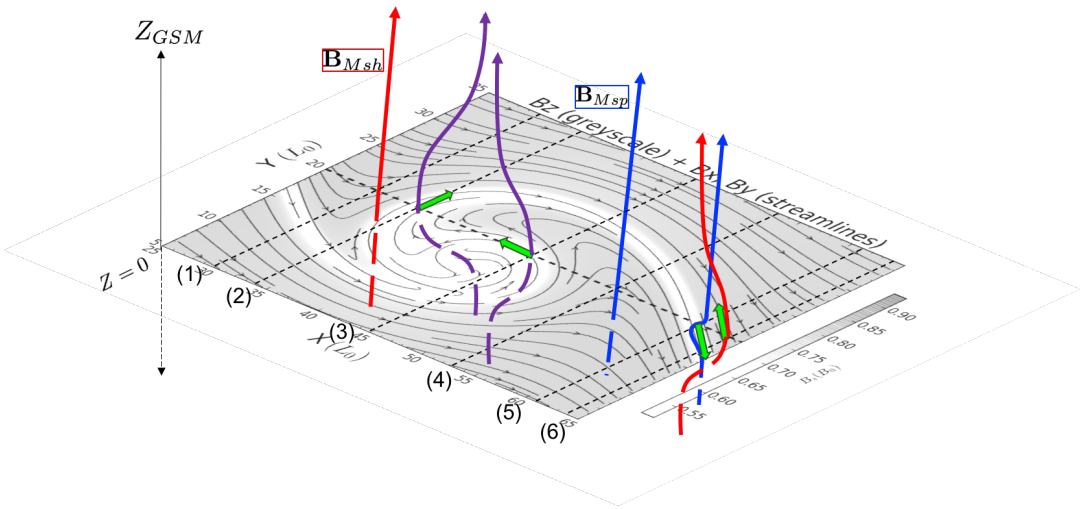

Figure 4.4.2: A schematic magnetic field of KH vortex. The simulation plane at $Z = 0$ (in GSM coordinates) shows magnetic field components B_z in greyscale and B_x, B_y with streamlines. 3D magnetic field lines are inferred based on magnetic curvature and curvature radius at locations (1) - (6) as marked in Figure 4.4.1 (see Table 4.1). Blue, red, and purple lines depict the field lines from magnetospheric (Msp), magnetosheath (Msh), and boundary layer regions respectively. Green vectors represent magnetic curvature as resolved in the equatorial plane.

(2), (3), and (5) respectively of Figure 4.4.2. The values for $a = L_0/4$ are represented with the horizontal grey dash-dotted lines. Truncation errors of order $(a/D)^2$ are represented with error bars in blue. In addition, to be resolved, the structure scale must be larger than a half of the spacecraft separation $R_c \geq a/2$ [*Shen et al.*, 2003], denoted here as a `resolving offset'. The validity of curvature radius data is represented by results above the resolving offset (shown as red dashed lines). Despite the truncation error bars, the results show that the resolved curvature radius increases with the tetrahedron size, linearly in range from a few L_0 to $10L_0$ particularly for the leading and trailing edges. The curvature direction does not change much in the same range. Vertical orange dashed lines denote the break in the linear increase at the tetrahedron size $10L_0$. Both curvature radius and direction erratically vary outside the ``linear" range, presumably because the magnetic fields do not have much linearity in the small ($\lesssim 3L_0$) or

Table 4.1: Magnetic Curvature and Field Values at the Marked X-Positions from tetrahedron size $a = 4L_0$ (See Figure 4.4.1).

	X-positions	R_c/λ_{KH}	$\mathbf{C}(L_0^{-1})$	$\mathbf{B}_3(B_0)$
(1)	29	5.8	(0.00, 0.00, 0.00)	(0.06, 0.05, 0.92)
(2)	33	0.5	(0.01, 0.05, -0.01)	(0.03, 0.24, 0.65)
(3)	44	0.4	(-0.07, -0.02, -0.01)	(-0.29, 0.05, 0.56)
(4)	52	5.6	(0.00, 0.00, 0.00)	(0.06, 0.05, 0.92)
(5)	60	0.2	(0.11, -0.09, -0.07)	(0.39, -0.29, 0.56)
(6)	63	0.5	(-0.04, 0.03, 0.02)	(0.15, -0.10, 0.92)

large ($> 10L_0$) scales. The vorticity magnitude in right column panels generally decreases as the tetrahedron size increases. This shows that the vorticity gradients of the KH wave are spatially quite constant, with strong vortical flows at the smaller scale, i.e., in panel (h), we find the linear fit $\Omega_z = -0.02a + 0.42$ in the range of tetrahedron sizes $a \in [4, 12]$.

The linear or non-linear variations in the four-spacecraft results with respect to the tetrahedron size could arise from spatial variations in the physical structures or from limitations in the techniques themselves. In Figure 4.4.4, we illustrate how spatial variations in the physical structures may lead to variations in curvature by considering two possible scenarios. For both of these scenarios, we cannot regard the variations of the curvature with respect to the tetrahedron size as inaccuracy of the technique, but rather the non-linearity of the physical structures. Similar considerations would apply for the vorticity. To fully understand the magnetic curvature of the KH wave, we further apply the MCA at every Y-location and then construct magnetic curvature maps. Figure 4.4.5 shows a comparison of the magnetic curvature maps of a fully rolled-up vortex from 3 sizes of tetrahedron ($a = L_0/4, L_0, 4L_0$). Left panels show the curvature radius R_c in wavelength unit and right panels show the curvature direction $\theta = \arctan(C_y/C_x)$ from 0^o to 180^o and 0^o to -180^o, over-plotted with the curvature projection $\mathbf{C}_p = C_x\mathbf{i} + C_y\mathbf{j}$. We will first investigate the curvature from the smallest tetrahedron and then study the effects of tetrahedron size.

We may characterise vortex regions based on magnetic curvature from the smallest tetrahedron ($a = L_0/4$) as it gives the smallest truncation error $O \sim (a/R_c)^2$ in panel (a). Curvature radius (left panel) shows increasing values away from the magnetopause as delineated by black dots. One prominent feature is the region of low curvature radius, of order $0.1\lambda_{KH}$ (red) to $0.5\lambda_{KH}$ (green), on the magnetospheric side of the magnetopause. This region, labeled by [1] in the right panel, hereafter referred to as the ``magnetospheric (M'spheric) KH spine", possesses $\theta$ directed from $-45^o$ to $45^o$ (anti-wave propagation direction) shown as a mint-green patch. On the magnetosheath side of the magnetopause, labeled by [2] in the right panel, hereafter referred to as the ``magnetosheath (M'sheath) KH spine", by contrast, possesses θ directed from 90^o to 180^o (wave propagation direction) shown as an orange-red patch. The curvature direction surrounding the rolled-up magnetopause on the magnetospheric side, labeled by [3] in the right panel, hereafter referred to as the ``magnetospheric (M'spheric) vortex", gradually increases from 45^o (golden) to 180^o (red) and then -180^o (purple) to -45^o (blue) with respect to the vortex rotation (anti-clockwise seen from above). A similar pattern can be noticed next to the magnetopause on the magnetosheath side, labeled by [4] in the right panel, hereafter referred to as the ``magnetosheath (M'sheath) KH vortex" where θ increases from -180^o (purple) to 90^o (golden). In the vicinity

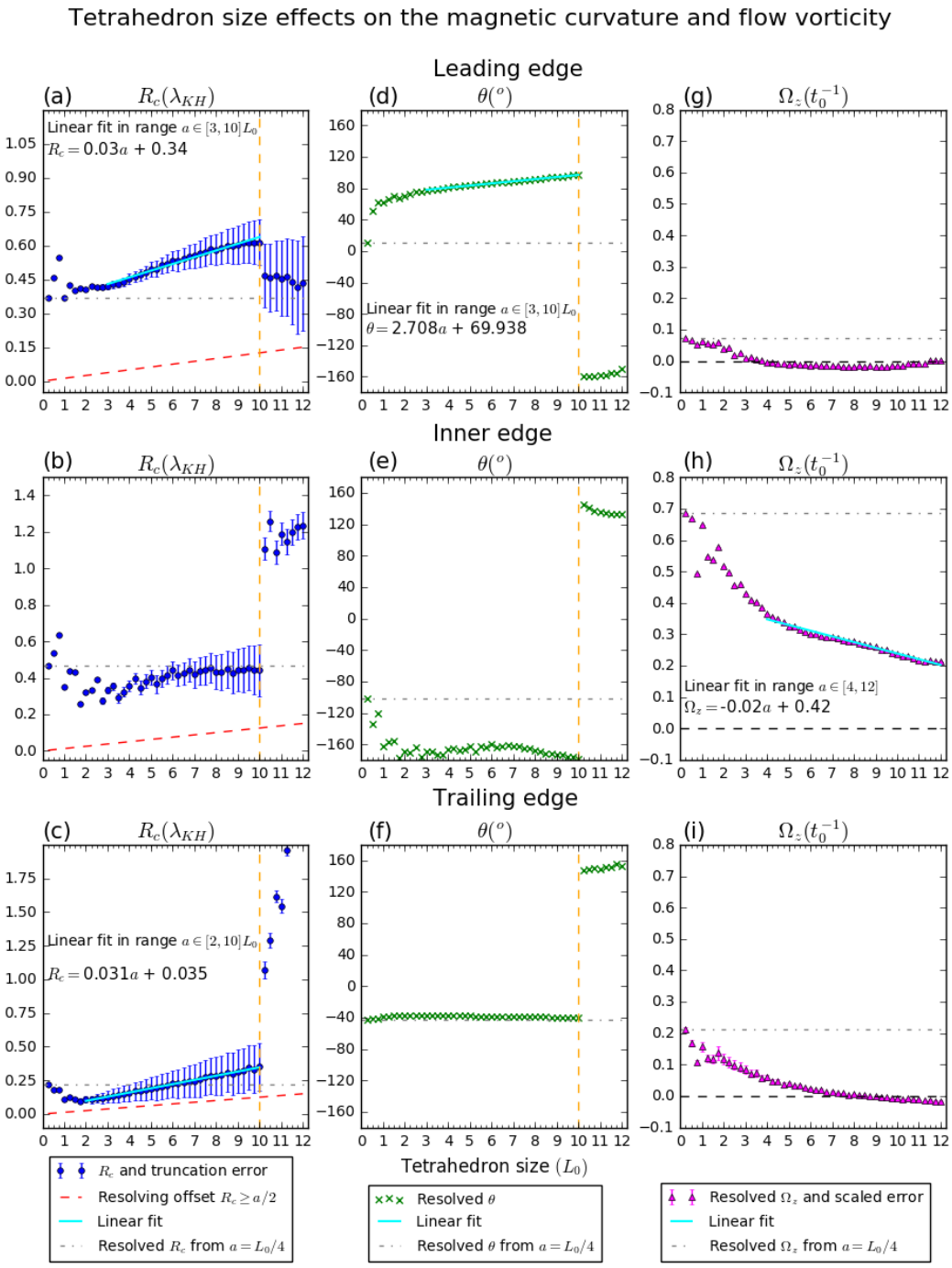

Figure 4.4.3: Curvature radius (a) - (c), curvature direction (d) - (f), and vorticity (g) - (i) against tetrahedron sizes at the selected locations : leading edge (top), inner edge (middle), and trailing edge (bottom) of the KH vortex shown in Figure 4.4.2 (numbers (2), (3), and (5), respectively).

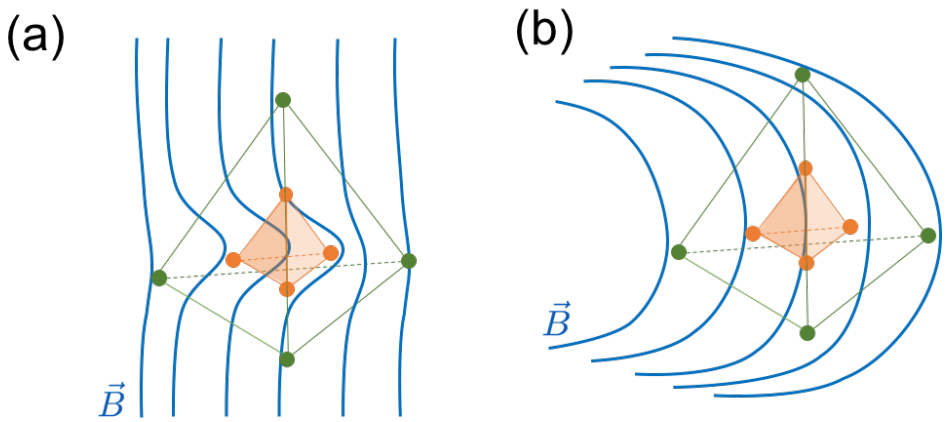

Figure 4.4.4: Spatial variations in magnetic field structures (blue) measured by nested spacecraft tetrahedrons of small (shaded orange) and large (green) scales (with the same barycentre). The magnetic field structures have (a) no variation at large scales but ``kinked" in the small scale, (b) no variation at the small scale but with linear gradient at large scale. As the tetrahedron size increases, these two physical structures would lead to (a) increasing (b) decreasing variations in radius of curvature.

of the vortex centre, labeled by [5] in the right panel, the curvature radius varies from $0.5\lambda_{KH}$ (green) to $9.0\lambda_{KH}$ (navy-blue). Curvature in this region, delineated by grey dashed lines, points in all directions except from -45^o to 45^o. Table 4.2 summarises these characteristic regions. For a temporal evolution of these characteristic regions, see Movie S1 in the supporting information of *Kieokaew et al.* [2018a]. Figure 4.4.6 is adapted from panel (a) of Figure 4.4.5 to sketch these regions based on the values in Table 4.2.

We present the impact of the tetrahedron size on magnetic curvature in Figure 4.4.5. In the vicinity of the KH vortex, the smaller tetrahedron yields more pronounced drops in radius values (see panel (a) in comparison to panels (b) and (c)). The curvature radius from bigger tetrahedron sizes increases faster away from the magnetopause. The curvature direction from bigger tetrahedron sizes resembles the pattern from smaller tetrahedron sizes, but with a less defined outline. The magnetospheric KH spine (labeled by [1] in Figure 4.4.6) is clearly visible in cases $a = L_0/4$ and $a = L_0$. The magnetosheath vortex pattern (labeled by [4] in Figure 4.4.6) persists for all tetrahedrons; however, the magnetospheric

Table 4.2: KH Vortex Region Characterisation from tetrahedron size $a = L_0/4$ (See Figure 4.4.6).

Regions	Range of θ	Range of R_c/λ_{KH}
[1] Magnetospheric KH spine	$-45^o \leq \theta \leq 45^o$	0.1 - 0.5
[2] Magnetosheath KH spine	$90^o \leq \theta \leq 180^o$	0.1 - 0.5
[3] Magnetospheric vortex	$45^o \leq \lvert\theta\rvert \leq 180^o$	0.5 - 2.0
[4] Magnetosheath vortex	$-180^o \leq \theta \leq 90^o$	0.5 - 2.0
[5] Vortex centre	$45^o \leq \lvert\theta\rvert \leq 180^o$	0.5 - 9.0

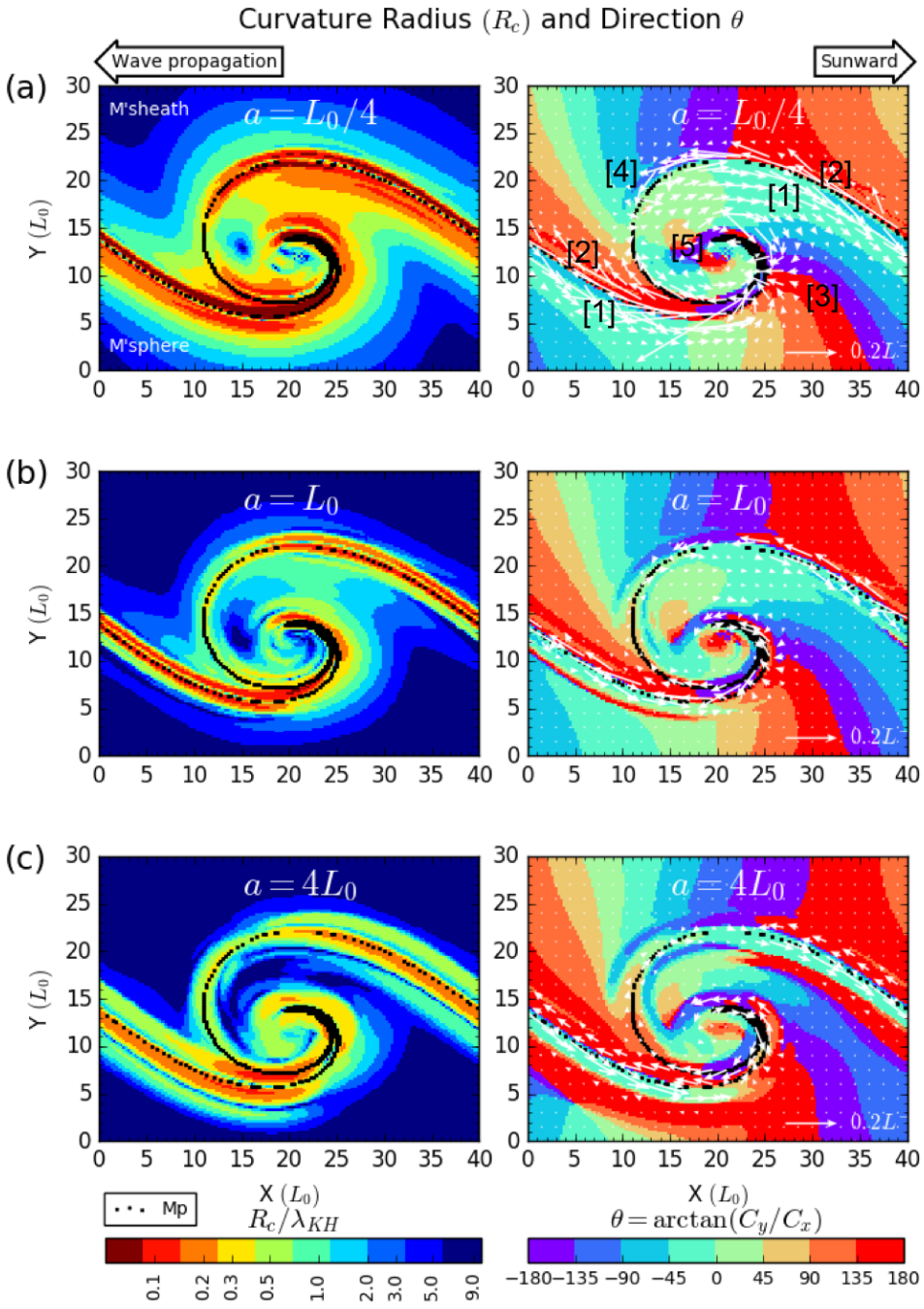

Figure 4.4.5: Magnetic curvature of a fully rolled-up KH vortex. Curvature is calculated from the MCA algorithm with tetrahedron sizes (a) $a = L_0/4$, (b) $a = L_0$, and (c) $a = 4L_0$. Curvature radius is shown on the left panel in discrete colour (nearest interpolation). Curvature direction is shown in the right panel with values binned to 45^o - range. White vectors on the left panel represent curvature projection. Numbers in the top right panel label the vortex regions [1] magnetospheric KH spine, [2] magnetosheath KH spine, [3] magnetospheric vortex, [4] magnetosheath vortex, and [5] vortex centre (See Table 4.2). Shaded areas outlined by grey dashed lines in the right panel mark vortex centre regions. For a temporal evolution of the top-right panel, see Movie S1 in the supporting information of the online paper [*Kieokaew et al.*, 2018a].

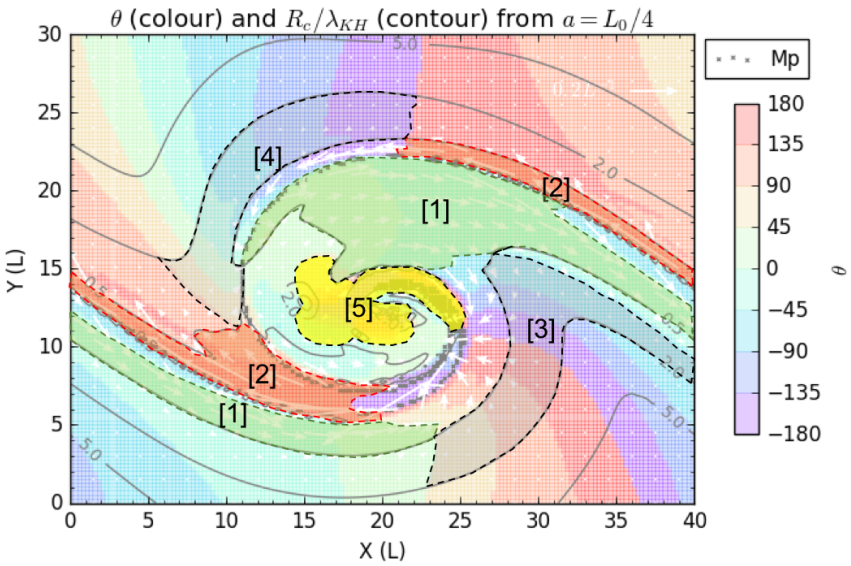

Figure 4.4.6: Sketch of the characteristic KH vortex regions adapted from panel (a) of Figure 4.4.5. Dashed lines mark boundaries of the characteristic regions using the criteria in Table 4.2.

vortex (labeled by [3] in Figure 4.4.6) appears less distinct as tetrahedron size increases. The mix of curvature direction identified at the vortex centre in right panel (in shaded area delineated by grey dashed lines) from the bigger tetrahedron appears less clustered. This suggests that only some characteristic regions such as the magnetospheric KH spine and the magnetosheath vortex can be resolved by MCA across all tetrahedron sizes, at least up to $a = 4L_0$ ($0.1\lambda_{KH}$).

Figure 4.4.7 shows a comparison of vorticity from the tetrahedron sizes $a = L_0/4$ and $a = 4L_0$ in panels (a) and (b) respectively. Flow vorticity dominates around the magnetopause, as expected for an original shear layer. Flow vorticity peaks at the same locations for both tetrahedron sizes but the magnitude is weaker for the bigger tetrahedron. This can be explained by the scaling of vorticity magnitude $|\Omega_z| = |\nabla \times V| \sim (V_2 - V_1)/a$, which reads that the magnitude of vorticity is inversely proportional to the inter-spacecraft separation a, for constant asymtotic values V_1 and V_2. However, this scaling is only satisfied when the spacecraft separation a is big enough (larger than the width of shear layer Δw) to sample the velocities on both sides of the shear layer. The vorticity is dominantly positive in and around the vortex centre, associated with counter-clockwise rotation of KH vortex seen from above. This is consistent with the vortical flow motion expected on the dusk-side magnetopause. However, there is a small negative vorticity in the magnetospheric side of the magnetopause, which may be attributed to a small clockwise rotation flow. We will further investigate this negative vorticity in the temporal studies.

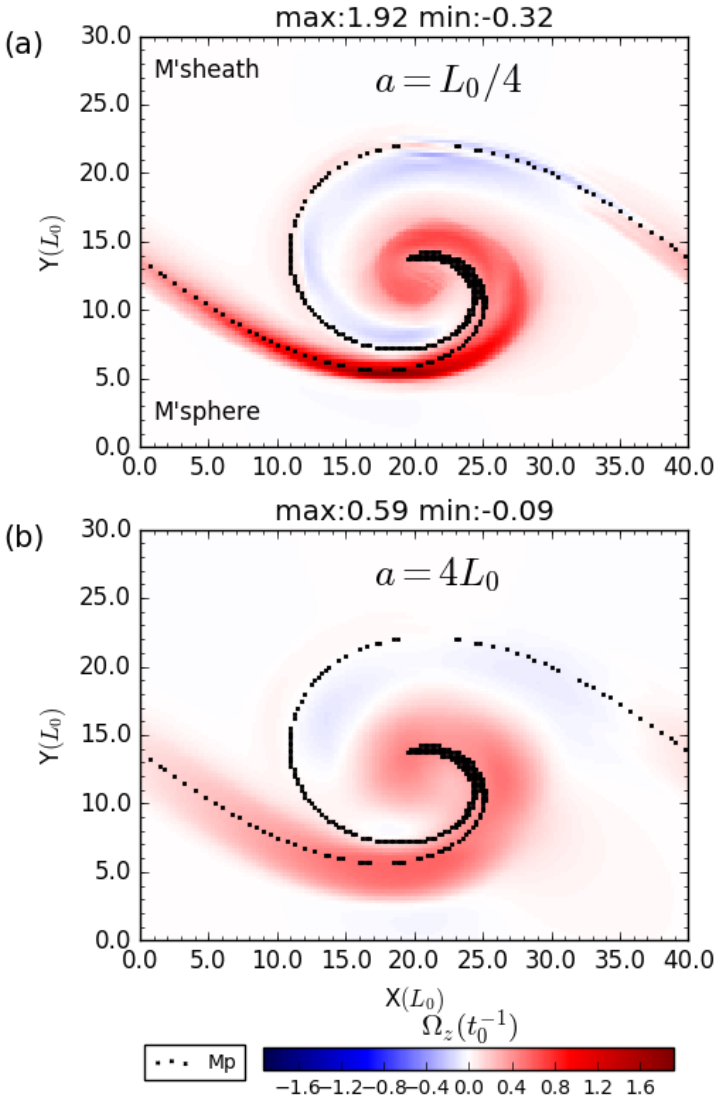

Figure 4.4.7: Flow vorticity of a fully rolled-up KH vortex. Vorticity component Ω_z is calculated from vorticity technique with tetrahedron sizes (a) $a = L_0/4$, and (b) $a = 4L_0$. Magnitude of vorticity is shown in symmetric colour scale from red (positive) to blue (negative). The negative vorticity, sandwiched between the vortex core and the magnetopause, is explained by the rolling-up process in which the vortex core has a stronger (positive) vorticity than the outer vortex regions near the magnetopause (original shear layer) (see text).

4.4.2 Temporal Studies

Figure 4.4.8 shows the time series for static spacecraft in the boundary layer recorded at the simulation centre (probe positions in panel (a) of Figure 4.4.1) using the tetrahedron size $a = 4L_0$ from the time $t = 20t_0$ to $t = 240t_0$ of the simulation. Note that the tetrahedron size $a = 4L_0$ (MHD scale), as illustrated in the spatial studies, is in the range in which the dependence on the tetrahedron size is linear. The time snapshot (in density) at $t = 100t_0$ in Figure 4.4.1 and time snapshots (in vorticity) at $t = 88t_0, 122t_0$ and $160t_0$ in Figure 4.4.10, which we will later discuss, are used to illustrate various stages of the KH wave. Ion density in panel (a) recorded at the four-probes shows 6 back and forth motions of the boundary layer during the time $t = 50t_0 - 200t_0$. We mark 6 transits from the magnetosphere to magnetosheath with numbers (1) - (6). Magnetic field at SC3 in panel (b) shows opposite polarity peaks of B_x and B_y which coincide with drop in B_z, showing characteristics of KH spines at the marked transits. Panel (c) shows ion velocity fluctuations at SC3. It is useful to note that a region of LDFTS is present between transits (2) and (3). Total pressure in panel (d) shows maxima at the transits (1) - (3). Curvature components in panel (e) shows a clear reversal in direction of C_x while crossing from the magnetosphere to magnetosheath. Curvature radius in panel (f) is found to be decreasing with time and reaching a value of less than a half wavelength $R_c \sim 0.5\lambda_{KH}$ at transit (2) ($t = 88t_0$). The curvature radius stays low after the transit (2) and fluctuates around the value of one wavelength until reaching the transit (5), then it fluctuates around increasing values between $\sim 0.1\lambda_{KH} - 10\lambda_{KH}$. Curvature direction (colour-coding corresponds to curvature direction in Figure 4.4.5) in panel (g) changes from $\sim 0^o$ (mint green dots) to $\sim 180^o$ (red dots) during the transitions. Vorticity in panel (h) starts out at the value $\Omega \approx 0.4t_0^{-1}$ because the probe barycentre is initially at the centre of the original shear layer. There are two clear peaks of vorticity between the transits (1) and (3) that are co-located with minimum in total pressure, as expected for rolled-up KH vortices at $t = 76t_0$ and $t = 100t_0$.

Brief episodes of negative vorticity are detected after the transits (2) - (6) in panel (h), and the vorticity peaks afterwards when the probes are crossing the KH spines (4) - (6). While the LDFTS is expected away from the vortex core in the magnetospheric side of the rolled-up vortex [*Hasegawa et al.*, 2006], it is not always present in the time series (see panel (c)). On the other hand, the negative vorticity is present after the vortex has rolled-up. The negative vorticity, generated during the rolling-up process, can be explained by the radial distributions (horizontal cuts) of the ion density and vorticity away from the vortex centre as seen in panels (b) and (e) of Figure 4.4.1. Here, the inner denser part of the vortex core (e.g., number (3) as reference) rotates faster than the outer tenuous part (number (4)) which is of magnetospheric origin. Since this tenous part has

zero vorticity initially and is between a strong positive vorticity of the vortex core (number (3)) and a weaker positive vorticity of the outer vortex regions near the magnetopause (original shear layer) (number (5)), it is susceptible to a reversed flow direction (see panel (c) of Figure 4.4.8) and therefore causing the negative vorticity. This effect is also clearly seen in Figure 4.4.7 and Movie S2 in the supporting information of the online paper [*Kieokaew et al.*, 2018a].

To understand the time evolution in the latter quantities in Figure 4.4.8, the analyses are done as follows. First, we take a time snapshot in KH vortex frame in the X-range of one wavelength (see the yellow box in panel (a) of Figure 4.4.1) for total pressure, curvature radius, and vorticity. Three Y-locations at the mid-plane (Y_{mid}), on the magnetosheath side ($Y_{mid} + \lambda_{KH}/8$), and on the magnetospheric side ($Y_{mid} - \lambda_{KH}/8$) are chosen, as marked by green, orange, and blue dashed lines respectively in Figure 4.4.10. For each quantity, we calculate the difference between its minimum value and maximum value at a given Y-location. This is a useful indicator of the level of the KH activity over time. To refer to evolution of the KH wave, we calculate KH growth from the average velocity perturbation of the whole simulation. To apply the LDFTS proxy, we calculate the percentage of roll-up (% RO) as in *Taylor et al.* [2012]. The lower density $n < 0.7n_{max}$ and faster than sheath $V_x < \langle V_x \rangle - \sigma$ criteria, where n_{max} is the maximum density, $\langle V_x \rangle$ is the average ion velocity of the time series, and σ is the standard deviation, are set as threshold for LDFTS plasma. The maximum density n_{max} and the average ion velocity $\langle V_x \rangle \pm \sigma$ are obtained from panels (a) and (c) of Figure 4.4.8 respectively. Figure 4.4.9 shows KH growth in panel (a), % RO in panel (b), change in pressure ΔP in panel (c), change in curvature radius ΔR_c in panel (d), and change in vorticity $\Delta\Omega_z$ in panel (e) as a function of time.

The KH growth rate in panel (a) of Figure 4.4.9 shows one growing mode with non-linear stage during $t = 40t_0 - 120t_0$. Panel (b) shows non-zero % RO during around $t = 80t_0$ to around $t = 122t_0$. Later when the growth rate reaches a saturation (see panel (a)), there appears a non-zero % RO during $t = 160t_0$ to $t = 200t_0$. Note that we only regard the former interval of the non-zero % RO as a rolled-up stage. The change in total pressure in panel (c) increases with time at the mid-plane (Y_{mid}, green solid line) and reaches its maximum at time $t = 88t_0$ (time snapshot in left panel of Figure 4.4.10), at the highest value among other Y-locations, and then decreases with time until around $t = 122t_0$. As expected, this change at Y-locations away from the mid-plane is weaker. The maximum of ΔP on the magnetosheath side ($Y_{mid} + \lambda_{KH}/8$, yellow solid line) is lower than that on the magnetospheric side ($Y_{mid} - \lambda_{KH}/8$, blue solid line). ΔP does not change much during the saturation phase at around $t = 122t_0$ to $t = 200t_0$.

Panel (d) of Figure 4.4.9 shows that the change in magnetic curvature radius decreases with time. This is due to the development of the roll-up at mid-plane

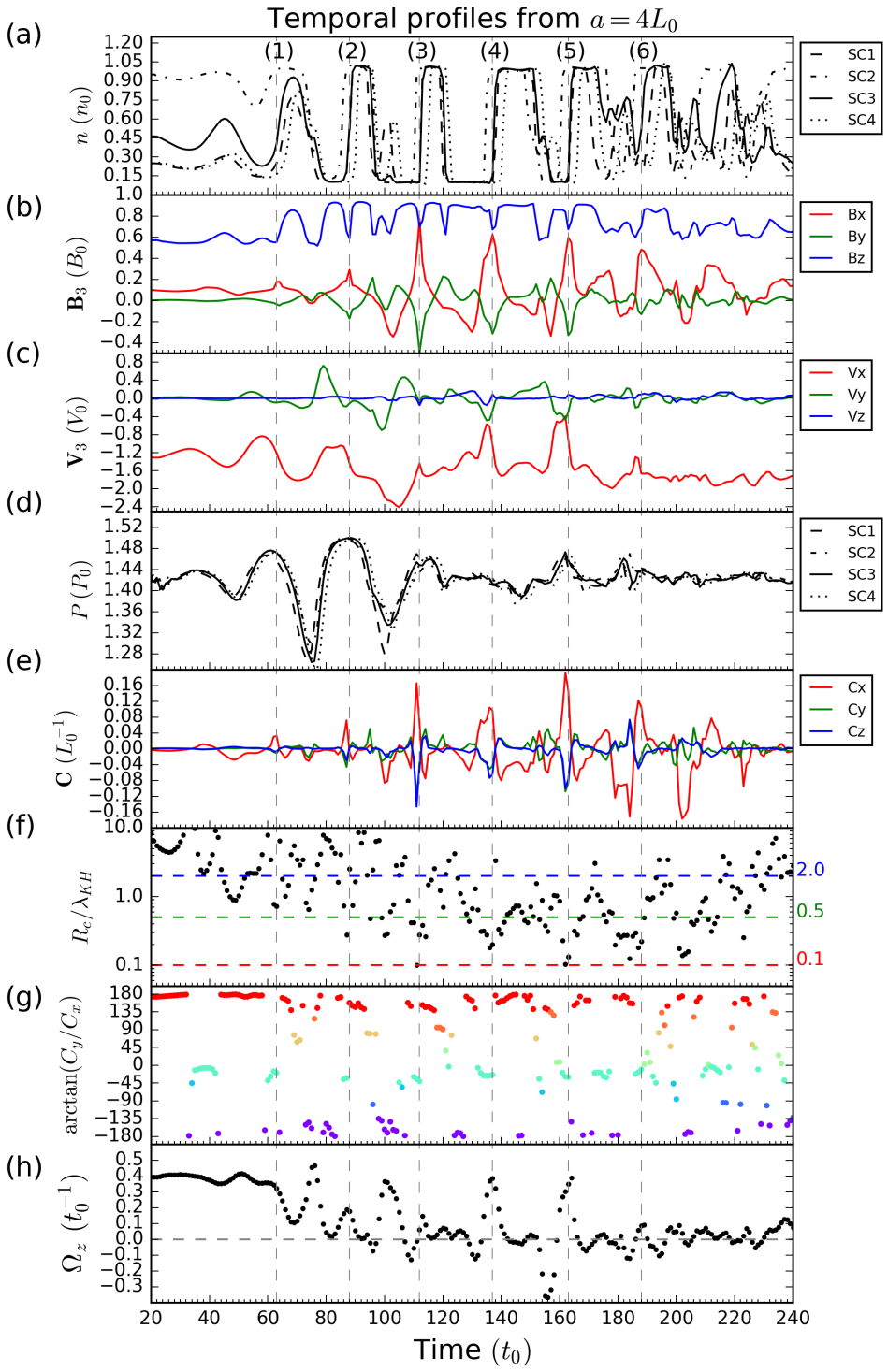

Figure 4.4.8: Time series from the tetrahedron size $a = 4L_0$ with the barycentre at SC3 in Figure 4.4.1. (a) density at SC1-SC4, (b) magnetic field at SC3, (c), ion velocity at SC3, (d), total pressure at SC1-SC4, (e) curvature components, (f) curvature radius, (g) curvature direction, and (h) flow vorticity. Numbers and vertical dashed lines mark transits from magnetosphere to magnetosheath. Curvature direction in panel (g) is colour-coded to correspond with the right panel of Figure 4.4.5.

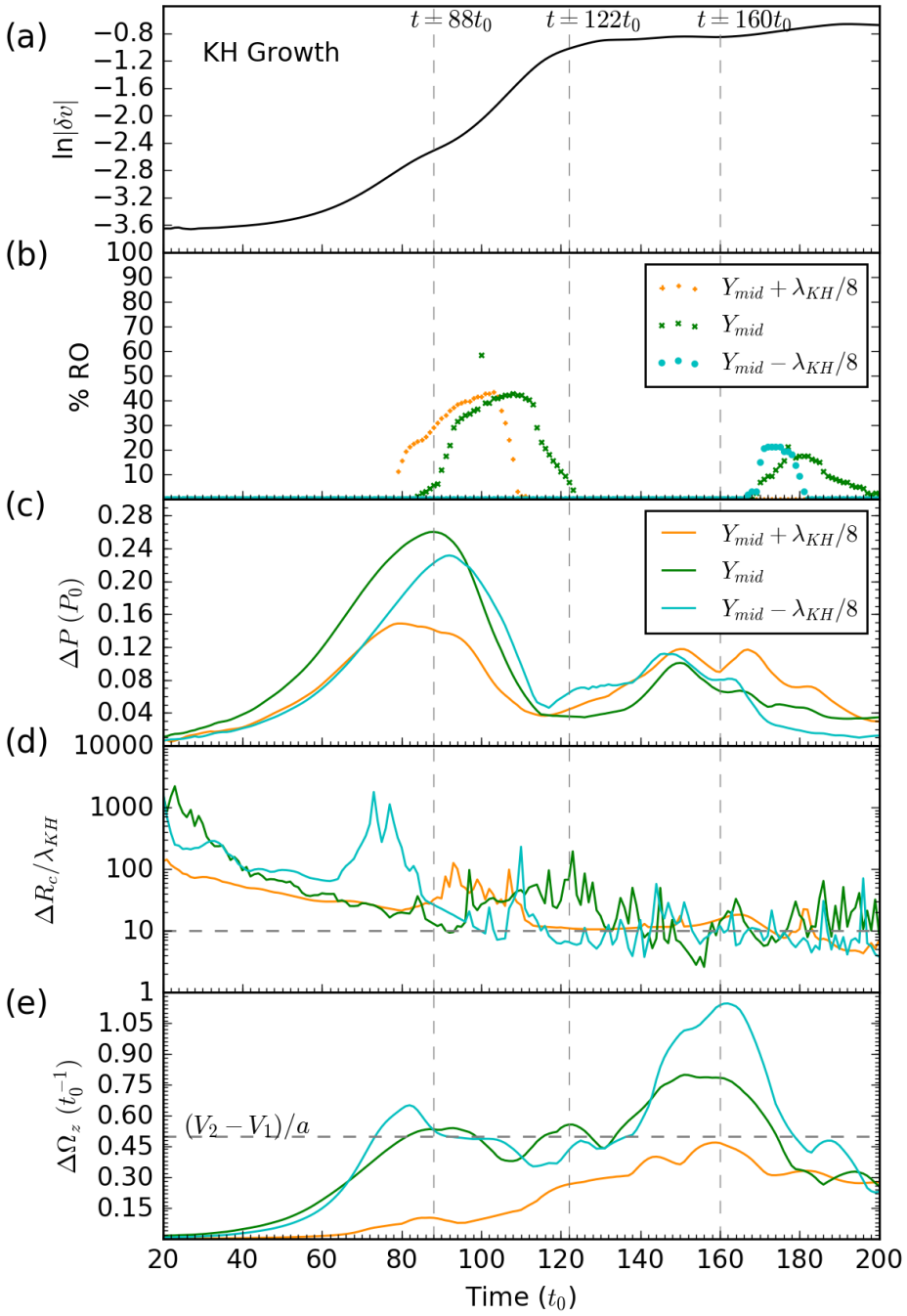

Figure 4.4.9: KH wave evolution. (a) average velocity perturbation (KH growth), (b) percentage of roll-up (percentage of ions that satisfy LDFTS plasma criteria), changes of (c) total pressure, (d) curvature radius, and (e) vorticity as a function of time. The changes in panel (c) - (e) are calculated from the difference between the maximum and minimum values at a given Y-location within X-range of one wavelength.

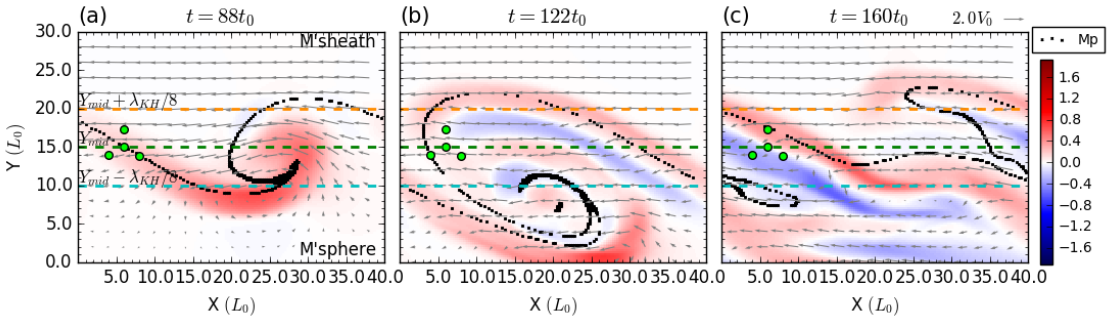

Figure 4.4.10: Evolution of flow vorticity in KH waves. This is the same format as Figure 4.4.7. (a) at $t = 88t_0$, (b) at $t = 122t_0$, and (c) at $t = 160t_0$. Grey vectors represent the velocity field in the static frame of magnetosphere. Green dots show static spacecraft positions (the same as panel (a) of Figure 4.4.1). Dashed lines represent four-spacecraft barycentres and correspond to panel (b) - (e) in Figure 4.4.9. For an animation of this sequence, see Movie S2 in the supporting information of the online paper [*Kieokaew et al.*, 2018a].

(green solid line). Despite the fluctuation, it can be seen that the change ΔR_c reaches its first local minimum at value $\sim 10\lambda_{KH}$ approximately when ΔP reaches its maximum. During $t = 88t_0 - 122t_0$, the trend of ΔR_c at mid-plane increases from $10\lambda_{KH}$ to $100\lambda_{KH}$, in contrast to the magnetosheath side where it decreases from $100\lambda_{KH}$ to $10\lambda_{KH}$. ΔR_c at all Y-locations stays low at value $\sim 10\lambda_{KH}$ after $t = 122t_0$. Overall, ΔR_c fluctuates more on the magnetospheric side, showing more activity of bending of magnetic field compared to at the magnetopause and on the magnetosheath side.

Panel (e) of Figure 4.4.9 shows that the changes in vorticity ($\Delta\Omega_z$) at mid-plane and on the magnetospheric side increase with time until around $t = 80t_0$. Then they approximately reach a plateau with a value $\sim 0.5t_0^{-1}$ until around $t = 120t_0$ at these locations. To justify this vorticity saturation, we suggest an explanation as follows. The change $\Delta\Omega_z = \Omega_{z,max} - \Omega_{z,min}$ at a given time along the mid-plane increases with time as the wave amplitude grows because it is more perturbed from sinusoids. Once the wave amplitude has significantly grown, the virtual probes should detect $\Omega_{z,min} = 0$ at non-shear layer regions; therefore $\Delta\Omega_z \approx \Omega_{z,max}$. This $\Omega_{z,max}$ is limited by the scaling value $\Omega_z \sim (V_2 - V_1)/a = 0.5t_0^{-1}$, given that there is no further rolling within the vortex. However, $\Delta\Omega_z$ further increases after $t = 120t_0$ and reaches its global maximum with a value of $2(V_2 - V_1)/a$ around $t = 160t_0$. We will next investigate this high change of vorticity. On the magnetosheath side, $\Delta\Omega_z$ gradually increases until $t = 160t_0$, with much lower magnitude compared to other Y-locations.

To understand the change in vorticity, we show time snapshots of vorticity at chosen times $t = 88t_0, 122t_0, 160t_0$ in panels (a), (b), and (c) of Figure 4.4.10 respectively (for full time-sequence, see Movie S2 in the supporting information of the online paper). The first maximum in $\Delta\Omega_z$ at $t = 88\ t_0$ (panel (e) of Fig-

ure 4.4.9) is associated with the development of the rolled-up vortex in panel (a) of Figure 4.4.10. The second peak of Ω_z at $t = 122t_0$ (panel (e) of Figure 4.4.9) is associated with the development of the negative vorticity layer (blue in panel (b) of Figure 4.4.10) in the rolled-up envelope on the magnetospheric side of the magnetopause, hereafter referred to a ``turnover layer." This turnover layer persists after the KH growth reaches a saturation and becomes stronger in vorticity magnitude (blue in panel (c) of Figure 4.4.10), giving rise to the global peak around $t = 160t_0$ (panel (e) of Figure 4.4.9) with strongest value in the magnetospheric side. This negative vorticity layer is reminiscent of the rolled-up history on the dusk-side magnetopause (the positive vorticity layer is expected on the dawn-side).

4.5 Summary and Discussion

We have analysed magnetic curvature and vorticity of the non-linear Kelvin-Helmholtz instability in a 2.5D MHD simulation using four-spacecraft techniques, using increasing (regular) tetrahedron sizes of virtual spacecraft. This is important to understand magnetic distortion and vortical flow induced by KH waves spatially and temporally for future analyses with real data. Our main results are as follows.

Magnetic curvature radius and direction vary depending on the sizes of the tetrahedron. This shows that there are no such `exact' values as they all depend on the structure we want to characterise (see Figure 4.4.4). For our particular example, this dependence is found to be linear in range of $a = [3L_0, 10L_0]$, ($[0.075\lambda_{KH}, 0.25\lambda_{KH}]$), especially at the leading and trailing edges of the non-linear KH wave. This linear increase breaks when the tetrahedron size becomes larger than a quarter of the KH wavelength ($10L_0$). The magnetic curvature erratically varies in the smaller range $a = [L_0/4, 3L_0]$, ($[0.00625\lambda_{KH}, 0.075\lambda_{KH}]$), particularly in the vicinity of the vortex centre. This illustrates how the KH vortex system may be understood on 3 scale ranges in which the linear and non-linear structures of KH waves may be expected. This also suggests that for a comprehensive understanding of the KH phenomenon, a cross-scale coverage of KH observations would be needed, best represented by 3 nested scales of spacecraft tetrahedron. Using a multi-scale tetrahedron size may also be useful for cross-scale KH studies, i.e., as recently reported for cross-scale energy transport from fluid to ion scales inside a KH vortex [*Moore et al.*, 2016].

MCA has revealed the detailed magnetic curvature of KH waves. Depending on tetrahedron size, specific regions are resolved. For the range of inter-spacecraft separations in our studies, $a = [L_0/4, 4L_0]$, ($[0.00625\lambda_{KH}, 0.1\lambda_{KH}]$), we resolve the so-called KH `spine' reported by *Otto and Fairfield* [2000] (and reference therein), marked by sharp gradient in B_z and different polarity of B_x and B_y. We report that this KH spine associated with the magnetospheric boundary layer is

characterised by curvature opposite to the wave propagation direction. We further report the existence of a magnetosheath boundary layer characterised by curvature in the wave propagation direction. Magnetic curvature against the shear flow in the magnetospheric boundary layer may be a consequence from plasma motion which drags along the magnetic field into the rotating vortex. Twisting of magnetic field lines around the vortex can be clearly seen from a gradual change of curvature direction both on the magnetosheath and magnetospheric sides. However, our simulation suggests that this twisting pattern can only be resolved on the magnetosheath side (so-called ``magnetosheath vortex'') for every tested tetrahedron size. Identifying these vortex regions in spacecraft data using curvature would be useful for sketching the magnetic geometry around a spacecraft trajectory, which can complement studies of other KH wave induced mechanisms such as magnetic reconnection.

A train of rotating vortices would give rise to periodical vorticity peaks, and these may be indicative of rolled-up KH vortices. This is illustrated in spatial studies (Section 4.4.1) in which we have shown the clear enhanced vorticity interval during the vortex centre passage. In temporal studies (Section 4.4.2) there are similar pulses but not all of them correspond to vortex centres, identified by minimum total pressure (i.e., at $t = 138t_0$ and $162t_0$). At these times the total pressure shows neither a minimum nor a maximum, but the magnetic field data show characteristics of KH spines (consistent with magnetic curvature direction and curvature radius). The vorticity peaks at these times arise from the shear flow layer. This can be observed by negative vorticity dips before positive peaks, showing passages of a turnover layer which is sandwiched between the vortex centre and the KH spine. We explain this negative vorticity layer as a result of the rolling-up process in which the vortex core has a stronger (positive) vorticity than the outer vortex regions near the magnetopause (original shear layer): the sandwiched, more tenous magnetospheric plasma, which has zero vorticity initially, is susceptible to a reversed flow direction. This effect is clearly seen in Figures 4.4.1, 4.4.7, 4.4.8, and Movie S2 of the online paper [*Kieokaew et al.*, 2018a]. The negative vorticity may also correspond to the `reversed shear flow' described by *Nakamura et al.* [2004] in two-fluid simulations (there this phenomenon was found to be related to the presence of a density jump as expected in our case at the magnetopause). In addition, we would like to point out that these shear layer crossings can give rise to periodic pulse-enhanced vorticity, even though the probes are not crossing through vortex centres. The pulse-enhanced vorticity Ω_z, together with current density J_z, is also found when spacecraft transit from magnetopause to magnetosheath in three-spacecraft studies of KH waves by *Shen et al.* [2012]. However, to pinpoint if spacecraft are passing the vortex centre of a rolled-up vortex, a strong vorticity peak due to the rotating vortex in

between two smaller peaks of vorticity from KH spines should be visible. Vorticity time series in Figure 4.4.8 during the transits (2) and (3) show a perfect example of a rolled-up vortex passage.

Change in curvature radius and vorticity with time may be indicative of different stages of KH wave development. The significant decrease of $\Delta R_c(t)$, from 1000 to $10\ \lambda_{KH}$, in the transition from linear to non-linear stage implies structural evolution in the magnetic field (consistent with *Ryu et al.* [2000]), especially on the magnetospheric side. The flow vorticity $\Delta\Omega_z(t)$ saturates at the expected scaling value $\Delta V/a$, where ΔV would be limited by the spacecraft separation, for fully rolled-up vortices. We suggest that observed $\Delta\Omega_z$ larger than the scaling value correspond to the development of a turnover layer which possesses negative vorticity (for dusk-side magnetopause). This layer exists in an elongated vortex, on the magnetospheric side of the magnetopause, in which a relative clockwise flow rotation can locally develop. Since this layer persists after the KH growth has saturated, it may be used as an indicator for a roll-up history of KH waves.

This work illustrates an example of combined four-spacecraft methods, with important applications to consider for analysis and interpretation of real spacecraft data. There are various limitations or simplifications to keep in mind. For instance, our results on magnetic curvature depended on the initial magnetic field configuration: finite curvature in the simulation is a consequence of an initial B_x component; in the absence of B_x, magnetic curvature would be zero everywhere. Asymmetric magnetic field B_z on both sides of magnetopause could result in more complex signatures ([e.g., *Nakamura and Daughton*, 2014]) and should be taken into account when interpreting real data. Also, non-alignment of B_z at the magnetopause surface, e.g., when IMF clock angle is non-zero, may already create a region of small curvature radius at the transition layers. Adding complexity to the model set-up will not affect the qualitative results at the magnetopause, namely: (1) the dependence of magnetic curvature on the tetrahedron sizes, (2) the detailed magnetic curvature characterisation, and (3) the vorticity signatures of the KH waves (i.e., spatial variations across a KH wavelength and temporal non-linear development). It may be useful to note that some of the vorticity signatures may occur because of the specificities of the magnetopause environment such as the presence of a density jump. In particular, previous studies indicate a shift between the centres of velocity and density profiles, which change the conditions for vortex formation [*Rossi*, 2015]. The observed signatures in our simulations will be shifted towards the vicinity of a KH vortex in cases where the shear layer is located away from the magnetopause (not shown). Non-ideal configurations of the spacecraft tetrahedron would affect gradient estimations, and subsequently the quality of the MCA estimates. In addition, our 2.5D results are applicable mainly in the equatorial plane. Finally, the chosen KH wavelength does not impact on the qualitative

results listed above as it only represents the physical scale of the KH structure with respect to the tetrahedron scale. Future works include an extension of our results to consider the applications in the higher latitudes by applying the techniques in 3D simulations. Finally, we aim to apply both four-spacecraft techniques in future work with the availability of in-situ data from two different 4-spacecraft missions Cluster and MMS.

Note that the order of magnitude of curvature radii in this Chapter is slightly different than those in Kieokaew et al. [2018a] due to a numerical bug while the qualitative results and conclusions are unchanged.

Part III

Four-spacecraft Applications to Observations

Chapter 5

Four-spacecraft Magnetic Curvature and Vorticity Analyses on KH Waves: Cluster Observations

[Results in this Chapter have been published in JGR (Space Physics), vol. 124, as *Kieokaew and Foullon* [2019]]

Magnetopause Kelvin-Helmholtz (KH) waves are rich in complex magnetic and flow structures which are key to understand the role of these waves in facilitating the solar wind plasma transport into the Earth's magnetosphere. Four spacecraft in tetrahedral configuration provide the tools necessary for characterising in-situ magnetic geometry and vortical flow. In this Chapter, we will apply the tools on KH waves observed by Cluster inside an electron boundary layer on the dusk side magnetopause. Magnetic curvature and flow vorticity properties of the KH waves will be obtained for various solar wind conditions. It will be shown that smaller curvature radius and higher positive vorticity are found for longer wavelengths. Changes in KH wavelengths observed with relatively fixed tetrahedron size allow us to resolve magnetic curvature across multiple scales. For the first time in space plasma observations, we will report the dependence of the curvature radius measurement on the ratio of the tetrahedron size to the wavelength, consistent with non-linear spatial variations of magnetic structures that would be resolved by nested cross-scale spacecraft tetrahedrons. It will be shown that negative vorticity is found to develop in the rolled-up vortex adjacent to positive vorticity in the vortex core. The strength of negative vorticity will be shown to increase with the solar-wind proton density and proton bulk flow speed. This Chapter provides observational evidence of multi-scale magnetic structures and is useful for understanding the development of rolled-up vortex signatures during various stages of solar-wind controlled KH wave evolution.

5.1 Introduction

Four-spacecraft analyses allow us to resolve in-situ spatial and temporal dimensions of space plasmas. Cluster is the first four-spacecraft mission, launched in 2000, to study the Earth's magnetospheric environments [*Escoubet et al.*, 2001]. Under northward interplanetary magnetic field (IMF) conditions, the Earth's magnetospheric boundaries along the flanks can be unstable to the Kelvin-Helmholtz (KH) instability. The KH instability can develop to form surface waves on the flank magnetopause which may facilitate solar wind plasma transport across the magnetopause through secondary mechanisms such as magnetic reconnection [e.g., *Nykyri and Otto*, 2001; *Nakamura and Fujimoto*, 2008] and turbulence [e.g., *Matsumoto and Hoshino*, 2004; *Rossi*, 2015]. Recently, a cross-scale energy transport from fluid to ion scales, a fundamental problem in plasma physics, has been reported within a KH vortex using Cluster observations [*Moore et al.*, 2016; *Retinò*, 2016]. KH waves can also be observed in other environments such as in the solar corona at the flank of a coronal mass ejection [*Foullon et al.*, 2011] and in a prominence [*Hillier and Polito*, 2018]. They are also observed in other planetary magnetospheric boundaries such as those of Mercury [e.g., *Slavin et al.*, 2008] and Saturn [e.g., *Masters et al.*, 2010]. Studying KH waves at the Earth's magnetopause has the advantage that in-situ multi-spacecraft measurements are much more accessible than in any other environment.

The KH instability bends magnetic fields and induces vortical flows in the magnetopause boundary layers. Magnetic and flow structures are ubiquitous in the Earth's magnetospheric environments and are best studied using multi-spacecraft observations. In particular, four-spacecraft techniques provide qualitative properties of space plasmas that are difficult to resolve by single-spacecraft methods. However, understanding applications and limitations of four-spacecraft techniques is essential to interpret their outputs. In Chapter 4, we applied magnetic curvature analysis (MCA) [*Shen et al.*, 2003] and vorticity analysis [*Chanteur*, 1998] techniques on magnetohydrodynamics simulations of magnetopause KH waves. In particular, we applied the techniques using various sizes of the four-spacecraft tetrahedron with a fixed KH wavelength. Multi-scale structural analyses of the KH process are the first step to a physical cross-scale understanding. Chapter 4 shows spatial characteristics of magnetic curvature and flow vorticity of the simulated KH waves as illustrated in Figure 5.1.1. For example, small radii of curvature are found along the KH wave trailing edges (sunward facing) in the magnetospheric boundary layer as shown in panel (a) (see also panels (c) and (d)). For a rolled-up vortex developed on the dusk side magnetopause, negative flow vorticity is expected to form between the strong positive flow vorticity of the vortex core and the positive flow vorticity of the original shear layer as shown in panel (b). This negative vorticity feature persists through the non-linear development

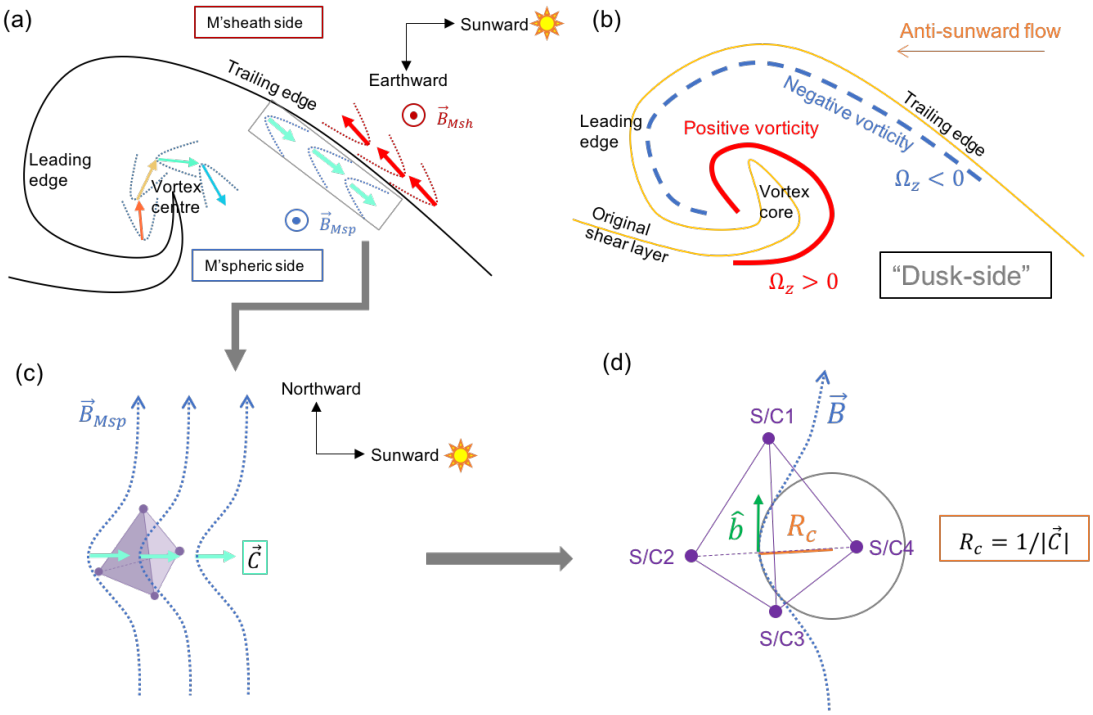

Figure 5.1.1: Sketch of (a) magnetic curvature directions and (b) flow vorticity of a KH vortex developed on the dusk-side magnetopause; and illustrations of the MCA technique (c and d). (a) Curvature directions (coloured vectors) point in the opposite direction across the wave trailing edge and turn in a clockwise sense around the vortex centre. (b) Vorticity is positive and strong around the vortex core while it is negative and weak between the vortex core and the original shear layer. (c) Magnetic curvature ($\vec{C}$) of the local magnetic field is resolved at the centre of the tetrahedron. (d) The corresponding curvature radius (R_c) is retrieved from $1/|\vec{C}|$ which is equal to the radius of a circle that can be fitted into the curved magnetic field line.

stage. Such expected signatures have yet to be confirmed in real observations.

Four-spacecraft measurements are sensitive to the distances between spacecraft. This was demonstrated in Chapter 4, where we found that the measures of four-spacecraft signatures of the magnetopause KH waves depend on the tetrahedron size. This is because plasma structures have non-linear variations in the spatial dimension (see panel (c)). In Chapter 4, we proposed the scenario of non-linear spatial variations that can lead to a measurement of magnetic curvature radius that is (1) increasing (see panel (a) of Figure 4.4.4) or (2) decreasing (see panel (b) of Figure 4.4.4) with the tetrahedron size. Of particular interest is the numerical result that the measure of the radius of curvature (panels (c) and (d)) should increase linearly with the tetrahedron size when the ratio of the tetrahedron size, a, to the KH wavelength, λ_{KH}, is between 0.075 and 0.25. Such ratios are easily achieved with Cluster at the magnetopause. The magnetic curvature in the simulation erratically varies with the tetrahedron size outside this range, possibly due to complex structures in small ($a/\lambda_{KH} < 0.075$) and large ($a/\lambda_{KH} > 0.25$) scales. Nevertheless, some qualitative features of the magnetopause KH waves

are shown to be less sensitive to the tetrahedron size such as magnetic curvature direction and flow vorticity polarity (as those sketched in panels (a) and (b)). With these simulated preliminaries in mind, we are now looking for observational confirmation of non-linear spatial variations of plasma structures associated with the Earth's flank magnetopause KH waves.

We choose KH observations on the dusk flank magnetopause by Cluster from the 20 - 21 November 2001 event. The coexistence of cold solar-wind and hot magnetospheric ion populations in the vortices is first reported as evidence of solar wind plasma transport during the non-linear stage of the waves by *Hasegawa et al.* [2004]. Magnetic and velocity perturbations are reported to be consistent with rolled-up vortices for a 16-minutes interval that is later confirmed by *Hasegawa et al.* [2006] using a single-spacecraft method [*Takagi et al.*, 2006]. *Chaston et al.* [2007] report evidence of diffusive transport across the magnetopause due to mode conversion from surface to kinetic Alfvén waves that is sufficient to account for the boundary layer formation. *Foullon et al.* [2008] characterise the evolution of the KH waves with the boundary layer thickness, geomagnetic latitude, and IMF clock angle (defined by the clockwise angle between the IMF orientation and the geomagnetic north direction) by utilising the exceptionally prolonged KH activity of about 17-hours. They select five 2-hour intervals of relatively steady solar wind conditions but with different IMF clock angles. In particular, using 4-spacecraft methods, they report the dependence of KH wavelengths and maximum spectral power on the IMF clock angle, consistent with *Farrugia et al.* [1998]. The dependence of the KH wavelength and amplitude on the IMF clock angle is explained by the linear theory which predicts the KH unstable region on the dayside magnetopause and the KH growth rates (see Section 1.3 in Chapter 1). We also note work by *Shen et al.* [2012] in which they employ multiple-point analysis tools and use the same short interval as *Hasegawa et al.* [2004] for illustrations of flow vorticity and current density calculated from a three-spacecraft method.

The Cluster 20 - 21 November 2001 event, as previously analysed by *Foullon et al.* [2008], allows us to benchmark the four-spacecraft methods for identifying rolled-up KH vortices, as proposed in Chapter 4. The resolved characteristics relate to physical phenomena that previous studies did not explore. Moreover, the different KH wavelengths and amplitudes (controlled by IMF clock angles) in the five intervals in *Foullon et al.* [2008] allow us to characterise KH properties at various scales. Indeed, the different KH wavelengths are observed with a four-spacecraft tetrahedral configuration that can be considered of fixed size during the event and relative to the wavelength changes. This is opposite to the approach in the numerical study in Chapter 4, where the size of the virtual tetrahedron is varied relative to a given wavelength from a single KH event. These two approaches are equivalent in that they allow us to study variations in KH wave properties for

changes in the a/λ_{KH} ratio. Therefore, the new observational approach will enable us to probe the KH waves in five `nested' scales with the aim to provide evidence for the non-linear spatial variations of KH structures.

In this Chapter, we will resolve three-dimensional spatial characteristics of magnetopause surface waves with four identical spacecraft forming a tetrahedral configuration that detail multi-scales of plasmas. We first investigate the magnetic curvature of simple boundary layer crossings of KH waves. The short interval in *Hasegawa et al.* [2004] and *Shen et al.* [2012] is revisited to benchmark applications of the four-spacecraft tools. We then compare four-spacecraft analysis results for different scales of KH waves subjected to various IMF clock angle conditions, as characterised in *Foullon et al.* [2008].

5.2 Data and Methodology

We investigate KH wave properties during the northward IMF conditions on 20 - 21 November 2001. Cluster entered the electron boundary layer (EBL) from the magnetosheath side at 09:15 UT on 20 November 2001 and exited the EBL to the magnetosphere at 03:00 UT on 21 November 2001. For this time interval, Cluster was in the EBL and did not cross the magnetopause. *Foullon et al.* [2008] characterise the KH activity into 5 intervals: A (10:00-12:00 UT), B (15:00-17:00 UT), C (18:04-20:04 UT), D (19:45-21:45 UT), and E (23:36-01:36 UT) with different IMF clock angle, solar wind proton bulk flow speed, and proton density. The solar wind conditions for each 2-hour interval are those tabled in *Foullon et al.* [2008], given in the observation frame of Cluster (see our Table 5.2). They were derived from the NASA High-Resolution OMNI (HRO) product that is initially measured by the Advanced Composition Explorer (ACE) satellite and time-shifted to a model bow shock nose. Since not all on board instruments of Cluster (C1, C2, C3, C4) were operative, we obtain plasma conditions as follows. Magnetic field data are provided by the Flux Gate Magnetometer (FGM) instruments on C1 - C4. Ion density, temperature and bulk velocity data are provided by the Composition and Distribution Function analyser (CODIF) instruments on C1, C3, and C4. Kinetic pressure is provided by the Hot Ion Analyser (HIA) instrument on C1 and C3. Original data are obtained in geocentric solar magnetospheric (GSM) system and transformed to the local boundary coordinates (LMN) using transformations given in *Foullon et al.* [2008] and derived from a model magnetopause [*Roelof and Sibeck*, 1993]. In this LMN coordinates, **N** is perpendicular to the unperturbed model magnetopause pointing away from the Earth, **L** points along $\mathbf{Z}_{GSM}$, and **M** completes the system (which is in the sunward direction for the dusk event).

The following information is important to understand and to justify four-spacecraft results. We use the KH wavelengths derived by *Foullon et al.* [2008] from applying

Table 5.1: Time-lags between C2 and C3 from Table 4 of *Foullon et al.* [2008] from magnetic field component B_m and electron temperature component $T_{e\perp}$ for a) inbound and b) outbound crossings.

Intervals	a) $B_{m3} - B_{m2}$	b) $B_{m3} - B_{m2}$	a) $T_{e\perp3} - T_{e\perp2}$	b) $T_{e\perp3} - T_{e\perp2}$	Average
A	20.4 s	-3.0 s	10.6 s	-1.5 s	6.6 s
B	8.1 s	20.3 s	9.6 s	4.8 s	10.7 s
C	-	-	11.1 s	18.7 s	14.9 s
D	17.6 s	8.8 s	4.1 s	10.5 s	10.3 s
E	-17.4 s	-	-	22.0 s	2.3 s

the timing analysis onto the wave leading and trailing edges (see panel (a) of Figure 5.1.1), in which the boundary normal speeds are obtained and projected onto the wave propagation direction. These KH wavelengths are proportional to the spectral power of the waves that correspond to the wave amplitudes [*Foullon et al.*, 2010]. The average inter-spacecraft separation during the event under study is 2000 ± 93 km. Considering dominant KH wavelengths, which are $1.5 - 2.9$ earth radii (R_E) for all intervals of KH activity in this event, the ratio of the tetrahedron size to the KH wavelengths is between 0.11 and 0.23 where a linear dependence of magnetic curvature on tetrahedron size is expected (see Figure 4.4.3). The average tetrahedron configuration has an elongation of 0.07 ± 0.05 and planarity of 0.08 ± 0.04, which can be categorised as a regular tetrahedron where high accuracy of four-spacecraft tools are expected [*Robert et al.*, 1998]. Figure 5.2.1 shows average Cluster C1 (black), C2 (red), C3 (green), and C4 (blue) positions projected on GSM X-Y, X-Z, and Y-Z planes. C3 is chosen as the reference spacecraft for its middle position along the X and Y directions which correspond to the wave propagation and perturbation directions, respectively, as seen in Figure 5.2.1.

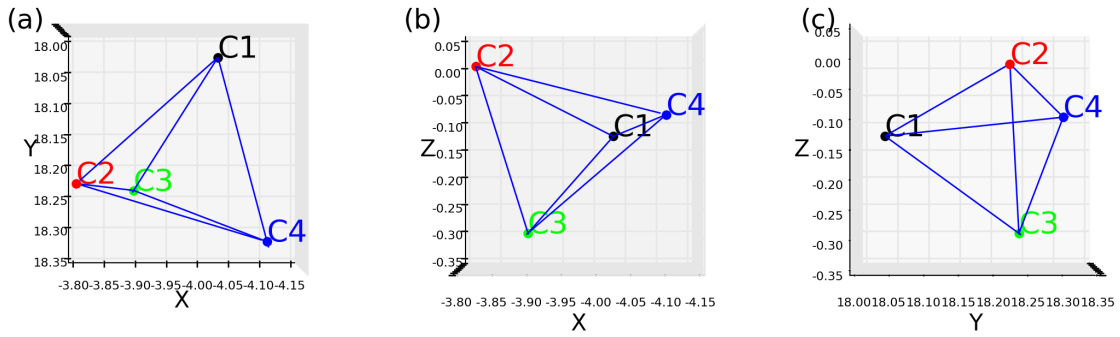

Figure 5.2.1: 2-D projections in (a) X-Y, (b) X-Z, and (c) Y-Z planes of the average Cluster positions in earth radii on 20 - 21 November 2001 between 9 and 3 UT in GSM coordinates. The X-Y projections of the Cluster positions (a) are similar to the virtual spacecraft positions in the X-Y positions in the simulation coordinates shown in panel (a) of Figure 4.4.1 but with a tilted tetrahedron.

Magnetic curvature (**C**) is calculated using the MCA technique as in Section 3.1

to calculate $\mathbf{C} = \mathbf{b} \cdot \nabla \mathbf{b}$, where $\mathbf{b}$ is the average unit magnetic field, at the tetrahedron barycentre with the solenoidal constraint of magnetic fields. Four-spacecraft vorticity, $\mathbf{\Omega} = \nabla \times \mathbf{V}$, where $\vec{V}$ is the velocity field, is calculated using the linear barycentric estimator [*Chanteur*, 1998] as in Section 3.2. These two techniques have been applied on KH waves in 2.5 MHD simulations using varying tetrahedron sizes in Chapter 4 (Section 4.3).

Since the ion bulk velocity data is not available at C2, we require a proxy to apply the vorticity technique. We are interested in comparison with previously simulated fluid-scale bulk flow properties. We can use the results obtained from applying a three-spacecraft technique on ion data [*Shen et al.*, 2012] to corroborate our derived vorticity. The high-cadence C2 electron dataset would require a separate treatment [*Foullon et al.*, 2008]. We thus obtain a proxy for the C2 ion bulk velocity by considering the 3-D spacecraft configuration in Figure 5.2.1 with respect to wave perturbations as follows. KH waves are mainly confined in the equatorial plane (X-Y plane in GSM system or M-N in LMN system) when the IMF is strongly northward. The waves propagate tail-ward in -X direction (-M in LMN system) with their amplitude growing in Y direction (N in LMN system) (see also Figure 5.1.1). C2 and C3 are far apart in the Z-direction as seen in panels (b) and (c) of Figure 5.2.1 by about $0.3\ R_E$ but this direction should not be of concern for our proposed approximation because it is not the main perturbation direction. Given that C2 is located close to C3 in the X-direction by about $0.1\ R_E$ and at almost the same level in the Y-direction as seen in panel (a), we obtain the C2 ion bulk velocity proxy by time-shifting the C3 ion bulk velocity data with time delays obtained from cross-correlation between time series. These time delays were derived by *Foullon et al.* [2008] (see their Table 4), where they obtain average four-spacecraft timings at C1 - C4 from magnetic field component B_m and electron perpendicular temperature $T_{e\perp}$ time series for both inbound and outbound crossings. These time delays are shown in Table 5.1 for a) inbound and b) outbound crossings for both B_m and $T_{e\perp}$ for the five intervals characterised in *Foullon et al.* [2008]. We use the average of these time delays in each two-hour interval. Averaging both time lags from the magnetic field and temperature series gives better statistics for ion velocity. Our vorticity result using the synthetic C2 ion velocity is found to be consistent with the vorticity calculated using a three-spacecraft technique by *Shen et al.* [2012] for the same interval.

Table 5.2: Upstream and local parameters for the five intervals A-E with statistical standard deviations: IMF clock angle (CA), solar wind proton bulk speed (V_{sw}), proton density (ρ_{sw}), average minimum radius of curvature ($R_{c,min}$) in R_E, average maximum vorticity ($\Omega_{l,max}$), and average minimum vorticity ($\Omega_{l,max}$).

Intervals	CA (^{o})	V_{sw} (km s^{-1})	ρ_{sw} (cm^{-3})	$R_{c,min}$ (R_E)	$\Omega_{l,max}$ (s^{-1})	$\Omega_{l,min}$ (s^{-1})
A	36 ± 3	443 ± 4	6.0 ± 0.7	0.50 ± 0.19	0.101 ± 0.017	-0.078 ± 0.015
B	12 ± 10	417 ± 2	4.8 ± 0.2	0.29 ± 0.06	0.123 ± 0.034	-0.059 ± 0.016
C	41 ± 18	400 ± 5	4.2 ± 0.4	0.40 ± 0.07	0.129 ± 0.030	-0.058 ± 0.027
D	19 ± 12	390 ± 3	3.8 ± 0.1	0.37 ± 0.08	0.119 ± 0.017	-0.039 ± 0.011
E	62 ± 16	389 ± 3	4.2 ± 0.3	0.75 ± 0.27	0.038 ± 0.013	-0.017 ± 0.001

5.3 Results

5.3.1 Magnetic curvature in the magnetopause boundary layers disturbed by KH waves

We first examine the magnetic curvature in the boundary layers disturbed by KH waves in order to investigate magnetic field distortions in the presence of the KH instability. Figure 5.3.1 shows time series between 15:39 and 15:46 UT for two adjacent waveform crossings: first, numbers (1) - (4), and, second, numbers (1') - (4') marked by vertical black lines. The first waveform crossing between 15:39 and 15:43 UT (numbers (1) to (4)) is shown as an example of an oscillatory structure in *Foullon et al.* [2008]. This time interval is part of interval B which has the lowest clock angle ($12^o \pm 10^o$) among the five intervals A-E.

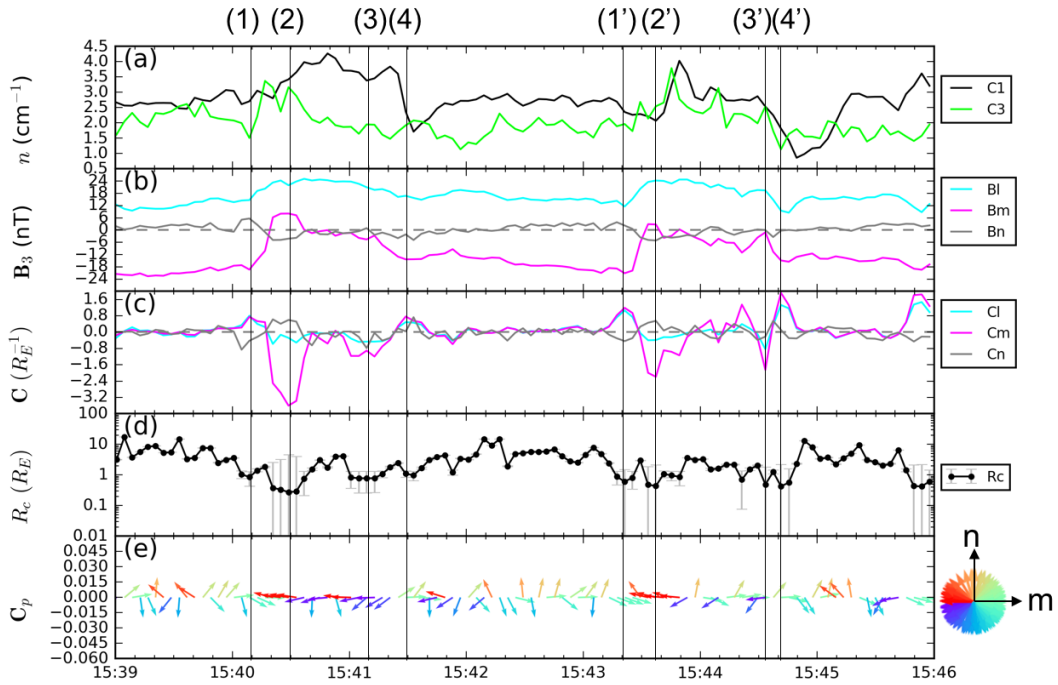

Figure 5.3.1: Crossings of an oscillatory structure between 15:39 and 15:46 UT. (a) ion density at C1 and C3, (b) magnetic fields at C3, (c) magnetic curvature components, (d) radius of curvature, and (e) 2-D normalised curvature projection $\mathbf{C}_p = (C_m\mathbf{m} + C_n\mathbf{n})/\sqrt{C_m^2 + C_n^2}$ with a colour-coded angle $\arctan(C_n/C_m)$.

Panel (a) of Figure 5.3.1 shows ion density at C1 (black) and C3 (green) which refer roughly to inner (tenous) and outer (dense) magnetospheric boundary layers. Since the KH waves propagate tail-ward, we may refer to transitions between boundary layer regions seen by the spacecraft as follows. An `outbound' transition is associated with the trailing edge (sunward facing edge) (see panel (a) of Figure 5.1.1) of the wave where the spacecraft transits from the inner to outer

magnetospheric boundary layers, e.g., from (1) to (2) and (1') to (2'). An `inbound' transition is associated with the leading edge of the wave where the spacecraft transits from the outer to inner magnetospheric boundary layers, e.g., from (3) to (4) and from (3') to (4'). Panel (b) shows magnetic field components at C3 with magnetic field rotations during the inbound and outbound transitions, best seen in B_m (purple line). These are signatures seen by all spacecraft.

We are next considering magnetic curvature at the barycentre of the four Cluster spacecraft as resolved by MCA. Panel (c) shows curvature components which indicate the direction of the magnetic tension force perpendicular to the magnetic field lines (see panel (c) of Figure 5.1.1). Curvature component C_m (purple) changes from positive ($\sim$ sunward) to negative ($\sim$ tail-ward) values during the outbound crossings, while it changes from negative to positive values during the inbound crossings. Panel (d) shows radius of curvature (see panel (d) of Figure 5.1.1) defined by $R_c = 1/\sqrt{C_l^2 + C_m^2 + C_n^2}$ with a truncation error $(a/R_c)^2$ where a is the tetrahedron size. The radius of curvature typically reaches a local minimum at each marked number (vertical solid line). Considering magnetic field configuration in the equatorial plane, we consider a 2-D curvature projection $\mathbf{C}_p = C_m\mathbf{m} + C_n\mathbf{n}$. Panel (e) shows the 2-D normalised curvature projection vectors with colour-coded angles $\theta = \arctan(C_n/C_m)$ (consistent with those in panel (a) of Figure 5.1.1). The curvature projection changes from sunward (mint-green) at around (1) to tail-ward (red) at around (2) during the outbound crossing. The curvature projection changes from tail-ward and earthward (purple) at around (3) to the opposite direction (green) at around (4) during the inbound crossing. These observational results show that magnetic curvature points in opposite directions when crossing the boundary layers disturbed by the KH waves, confirming the simulation result in Chapter 4, e.g., Figure 4.4.5.

The opposite change of curvature direction across the boundary layer is likely due to the bending of magnetic fields by the KH waves. We notice that the magnetic field rotation at outbound crossings (e.g., from (1) to (2)) is more pronounced than that at the inbound crossings (e.g., from (3) to (4)). Also, we notice that the radius of curvature in panel (d) on the outer magnetospheric side (e.g., number (2)) is smaller than that on the inner magnetospheric side (e.g., number (1)). This implies that the magnetic field bending is stronger on the outer magnetospheric side.

5.3.2 Rolled-up vortex signatures

Figure 5.3.2 shows time series for the interval between 20:30 and 20:40 UT. This time interval was shown to have signatures consistent with rolled-up vortices in *Hasegawa et al.* [2004]; *Hasegawa et al.* [2006]. This time interval is also studied in the wider 2-hour interval D by *Foullon et al.* [2008] and used for illustrations of

three-spacecraft calculations of vorticity and current density in *Shen et al.* [2012]. We are now revisiting this time interval using the four-spacecraft techniques.

Panels (a) - (d) show time series from C1, C2, C3, and C4, with black, red, green, and blue lines respectively. Vertical dotted lines mark outbound transitions in which the spacecraft transit from inner to outer magnetospheric boundary layers (wave trailing edges). Panel (a) shows magnetic field components B_m, which generally increases sharply at each outbound transition. Panel (b) shows ion density which also generally increases sharply at the outbound transitions. Panel (c) shows ion bulk velocity components V_m (thick solid lines) and V_n (thin solid lines) with the proxy data at C2. Using the lower-density and faster-than-sheath (LDFTS) criteria given in *Hasegawa et al.* [2006] where $n < 6$ cm^{-3} and, to first approximation, $|V_m| > 290$ km s^{-1}, we mark the ion population that fits the criteria in panel (b) with green dots. The LDFTS population is best seen at ∼20:33 UT marked by a vertical black solid line, co-located with the fast tail-ward speed ($V_m < -290$ km s^{-1}) in panel (c) (thick solid lines). This population is found at the beginning of a turning of the ion bulk velocity component V_n from earthward ($V_n < 0$) to anti-earthward ($V_n > 0$) seen at C1 (black thin line) which corresponds to a counter-clockwise (CCW) vortical flow seen from above the equatorial plane, as expected for vortices developed on the dusk side. These qualities of the flow are strong evidence of a vortex. Panel (d) shows total pressure of magnetic and kinetic pressure which is typically high at outbound transitions and low in the vicinity of vortex centres, as expected from simulations.

The MCA results are shown in panels (e) - (g). Panel (e) shows curvature components and panel (f) shows the normalised curvature projection ($\mathbf{C}_p = C_m\mathbf{m} + C_n\mathbf{n}$). The outbound transitions (vertical dotted lines) co-locate with C_m minima in the outer magnetospheric side which correspond to tail-ward curvature ($C_m < 0$) in panel (e) (purple line). In panel (f), we notice a curvature vector rotation at around 20:33 UT marked by a circle next to the LDFTS plasma (green dots in panel (b)). The curvature projection rotates from tail-ward (red) to sunward (mint-green), corresponding to a clockwise (CW) rotation seen from above the equatorial plane, and consistent with the curvature directions sketched in panel (a) of Figure 5.1.1 at the vortex centre. This curvature rotation is against the CCW vortical flow at 20:33 UT, reported earlier in panel (c). During 20:33 and 20:35 UT, the curvature vectors mainly point in the sunward and earthward direction (mint-green). Panel (g) shows the radius of curvature which is typically found to reach a local minimum at the outbound transitions (similar to (2) and (2') in panel (d) of Figure 5.3.1). The radius of curvature does not show distinct variations during the rolled-up vortex passage at 20:33 UT.

Panel (h) shows northward vorticity component Ω_l which is along Z in GSM coordinates. The northward vorticity is found to reach a maximum at the outbound

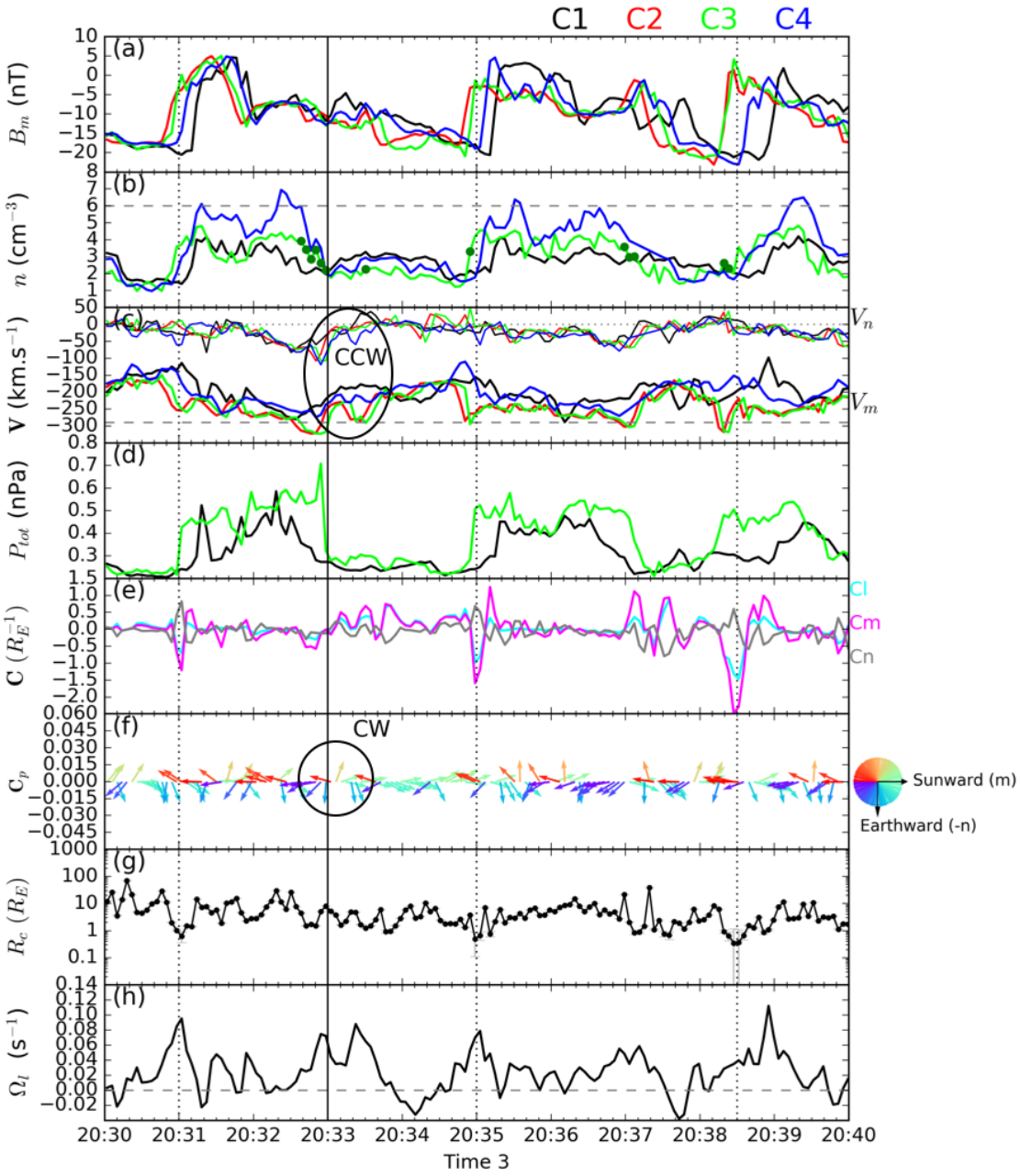

Figure 5.3.2: Time series observed on 20 November 2001 during 20:30 and 20:40 UT at C1 (black), C2 (red), C3 (green), and C4 (blue) of (a) magnetic field component B_m, (b) ion density n, (c) ion velocity components V_m, V_n, and (d) total pressure P_{tot}. Four-spacecraft results at the tetrahedron barycentre - (e) magnetic curvature components C_l, C_m, C_n, (f) 2-D normalised curvature projection $\mathbf{C}_p = (C_m\mathbf{m} + C_n\mathbf{n})/\sqrt{C_m^2 + C_n^2}$ with a colour-coded angle $\arctan(C_n/C_m)$, (g) curvature radius R_c, and (h) northward component, Ω_l, of the vorticity ($\mathbf{\Omega} = \Omega_l\mathbf{l} + \Omega_m\mathbf{m} + \Omega_n\mathbf{n}$).

transitions, consistent with the three-spacecraft study by *Shen et al.* [2003]. These maxima are due to the shear layer transitions at the wave trailing edges (see panel (b) of Figure 5.1.1), typically associated with high total pressure, and should not be confounded with vortex centres which correspond to low total pressure. For the rolled-up vortex at around 20:33 UT, we notice high positive vorticity interval with a peak of value $\Omega_l \sim 0.10$ s^{-1}. After that, the vorticity decreases and then reaches negative values with a minimum of -0.03 s^{-1} at around 20:34 UT. This pair of high positive and small negative vorticity intervals confirm the rolled-up vortex signature found in the simulation in Section 4.4.2 as sketched in panel (b) of Figure 5.1.1. The negative vorticity is also found in the next adjacent waveform with more negative values briefly before 20:38 UT, consistent with the simulation result that the negative vorticity remains present in the saturation phase (e.g., Figure 4.4.10).

5.3.3 Parametric survey

We further apply the four-spacecraft techniques in the intervals A-E to compare properties of local magnetic and flow structures when the wave activity is subjected to different solar wind conditions (as characterised in *Foullon et al.* [2008]). For the magnetic curvature property, we consider a minimum curvature which is typically found at the wave trailing edges (e.g., vertical dotted lines in panel (g) of Figure 5.3.2). Note that a maximum curvature radius is of no interest because it is typically very large and therefore indicates a straight magnetic field line. For the vorticity, we consider its maximum and minimum values. These curvature radius and vorticity extrema may be regarded as the local properties associated with the waves. To obtain these extrema, we divide each 2-hour interval into 10 sub-intervals of 12 minutes. The chosen sub-interval duration is larger than the KH wave period which is 3-4 minutes for the dominant mode (see Table 5 of *Foullon et al.* [2008]), and is adequate because a waveform does not always periodically appear. The extrema are obtained for each sub-interval and their averages for each 2-hour interval are presented in Table 5.2. We follow the characterised 2-hour intervals in *Foullon et al.* [2008] as they provide optimal intervals to study a variety of solar wind IMF clock angle conditions and minimise standard deviations of the IMF clock angles.

The representative four-spacecraft outputs are plotted against the solar wind conditions in Figure 5.3.3. The upper panels (a), (d) and (g) show the average minimum radius of curvature against the solar wind conditions. The minimum radius of curvature positively correlates with the IMF clock angle as seen in panel (a). This means that magnetic field structures are more bent (smaller radius of curvature) for lower IMF clock angle. The minimum radius of curvature does not show significant correlations with either solar wind speed (panel (d)) or proton

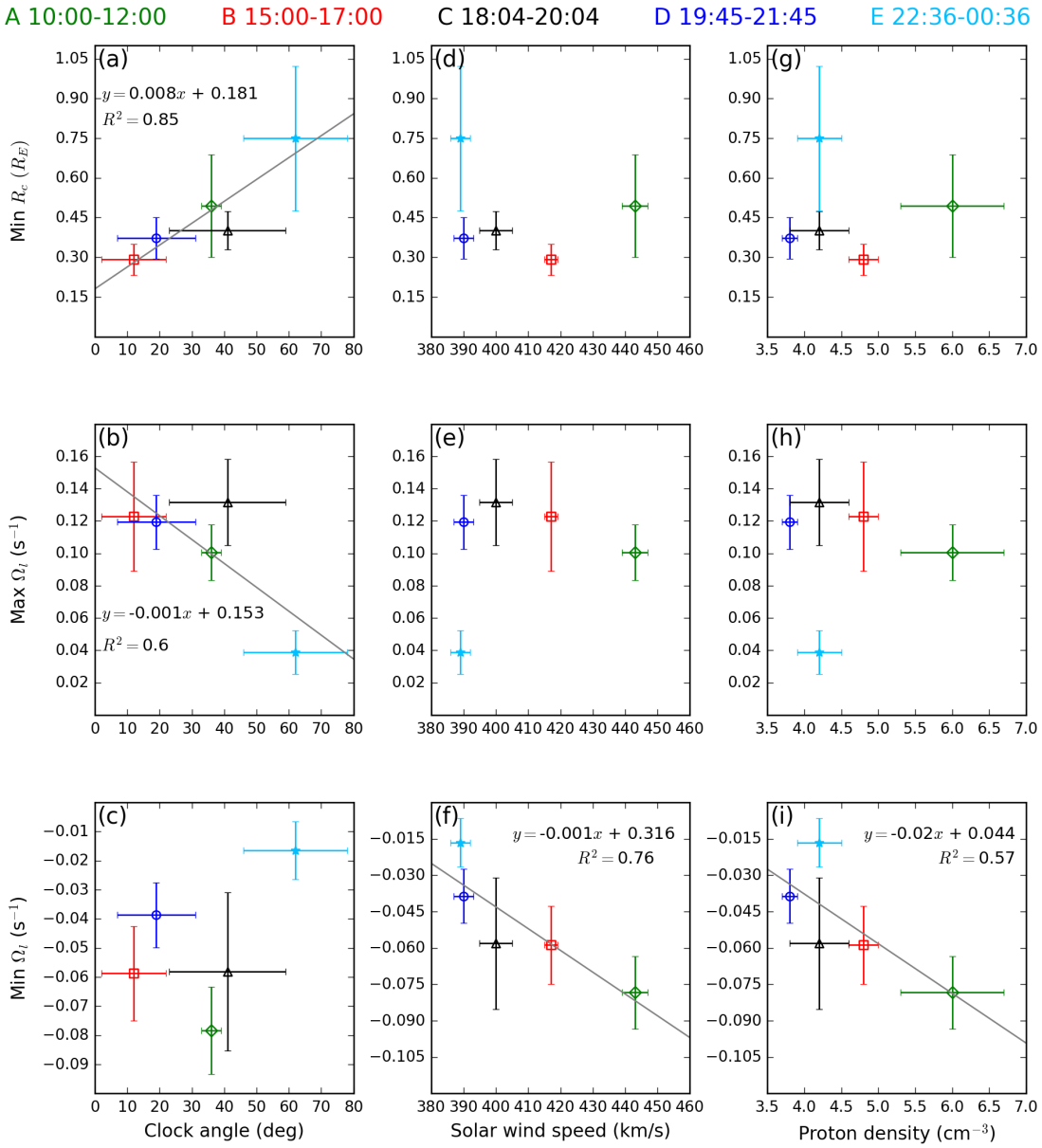

Figure 5.3.3: Parameter space plots between upstream parameters (a-c) IMF clock angle, (d-f) solar wind proton bulk speed, (g-i) solar wind proton density versus in-situ four-spacecraft outputs (a,d,g) minimum radius of curvature, (b,e,h) maximum vorticity, and (c,f,i) minimum vorticity for the five intervals A (green diamond), B (red square), C (black triangle), D (blue circle), and E (cyan star) with average values and standard deviations shown in Table 5.2.

density (panel (g)). The middle panels (b), (e) and (h) show the average maximum vorticity against the solar wind conditions. The maximum vorticity has a positive sign as expected for vortices developed on the dusk-side magnetopause. The maximum vorticity is found to be higher for lower IMF clock angle as seen in panel (b). Excluding the interval E, the maximum vorticity slightly decreases with faster solar wind speed as seen in panel (e) and denser proton density as seen in panel (h). Note the interval E has almost no KH activity and therefore may be regarded as a control group. Without the interval E (blue star), the trend in panel (b) would be unclear. This is because the interval C (black triangle) is an outlier. The interval C has the highest maximum vorticity in panels (b), (e), and (f). From detailed investigations, it appears that there is a sudden drop in ion bulk velocity, of about $\Delta V = 250$ km s^{-1}, during the interval C (see panel (b) of Figure 2 of *Foullon et al.* [2008] for data at C3). Therefore, the high vorticity of the interval C is not purely caused by the KH wave activity but results from the sudden change in ion bulk velocity during the interval (hence the large error bar). This has to be taken into considerations when interpreting the vorticity from the interval C. The lower panels (c), (f) and (i) show the average minimum vorticity against the solar wind conditions. The minimum vorticity has a negative sign. The minimum vorticity does not correlate well with the IMF clock angle as seen in panel (c). The minimum vorticity becomes increasingly negative with the higher solar wind speed as seen in panel (f) and higher proton density as seen in panel (i). Despite limited data points, panels (a), (b), (f), and (i) show good correlations (with the correlation coefficient $R^2 \geq 0.6$). We discuss all these features in the next section.

5.4 Discussions

The four-spacecraft analyses above have revealed additional signatures of the KH waves observed on 20 - 21 November 2001 by Cluster, complementary to previous studies. MCA reveals magnetic distortions caused by the KH waves. In particular, we have seen evidence of magnetic field twisting against the vortical flow at the vortex centre (highlighted by black circles in panels (c) and (f) of Figure 5.3.2), consistent with the simulation in Chapter 4 (panel (a) of Figure 5.1.1). MCA also aids in distinguishing KH waves regions as proposed in Chapter 4, by confirming several signatures as follows. First, we find minimum curvature radii at the wave trailing edges (less than $1\ R_E$). Second, in the same regions, magnetic curvature, which points in the magnetic tension direction, is found to point sunward and earthward on the inner magnetospheric side and to rotate into the opposite direction on the outer magnetospheric side. This magnetic field distortion at the wave trailing edges may be favourable for magnetic reconnection, the so-called Type I vortex-induced-reconnection [e.g., *Nakamura and Fujimoto*, 2008], and it is

consistent with recent observations [*Eriksson et al.*, 2016]. Evidence of magnetic reconnection is reported at 20:34:55 UT (near the third vertical dashed line in Figure 5.3.2) by *Hasegawa et al.* [2009]. Magnetic field distortions due to the twisting of the magnetic field lines may lead to the anti-parallel magnetic configuration (in 3-D) favourable for reconnection at this location.

We have shown signatures of vorticity as seen in panel (h) of Figure 5.3.2 between 20:31 and 20:35 UT, consistent with rolled-up vortices and rolled-up vortex history proposed in Chapter 4 (panel (b) of Figure 5.1.1). A relatively high positive vorticity is found in the vicinity of the LDFTS plasma as seen in panels (b) and (h) of Figure 5.3.2. We note here that the magnitude of the vorticity at the vortex centre is not significantly higher than at the boundary layer (original shear layer). In Chapter 4 (and also in *Gratton et al.* [2009]), the vortex centre has stronger vorticity than that of the original shear layer. This is possibly because the detected KH waves are at the interface between outer and inner magnetospheric boundary layers while those in the simulations are at the magnetopause surface. We also found negative vorticity next to the positive vorticity at the vortex centre, consistent with simulations in Chapter 4 (see panel (b) of Figure 5.1.1). This feature is also consistent with counter-rotating vortices (with the negative vorticity) which arises after one roll-over time shown in three-dimensional MHD simulations by *Gratton et al.* [2009].

We now discussed the features identified in Figure 5.3.3 from comparing the five 2-hours data intervals characterised by *Foullon et al.* [2008]. Since *Foullon et al.* [2008] demonstrated the occurrence of larger KH wavelength and amplitude for lower IMF clock angle, it is possible to discuss relationships between the size of the KH waves and the local properties given by our results. In Figure 5.4.1, we show relationships between the minimum curvature radius and the KH wavelength. Average minimum curvature radii versus KH wavelengths of the dominant modes for the five intervals are plotted in panel (a) of Figure 5.4.1. There is a tendency for the smaller (minimum) curvature radius measurement to occur in larger KH waves. This could result from non-linear developments of small scale structures inside the large scale waves. However, taking into account the tetrahedron size effect in panel (b) of Figure 5.3.3, we reveal a dependence that can be interpreted as multi-scale structures resolved by different ratios of a/λ_{KH}.

Consistent with non-linear spatial variations of physical structures, we found in Chapter 4 that the magnetic curvature radius measurement resolved by MCA is dependent on the tetrahedron size. These non-linear spatial variations can be resolved by a cross-scale configuration of small and larger scale tetrahedrons with the same barycentre, as shown in their simulation for a single wavelength KH wave. Looking for such observational evidence, we have used for the first time a favourable event to resolve spatial variations of the magnetic structures in

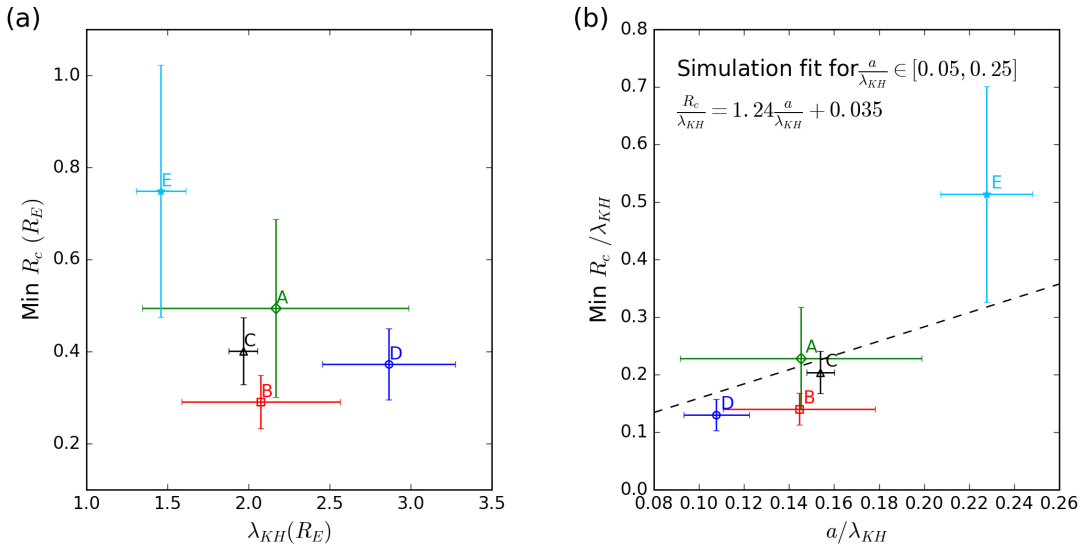

Figure 5.4.1: (a) Minimum curvature radii versus KH wavelengths of the dominant modes in the five intervals A-E. (b) Minimum curvature radii versus Cluster tetrahedron sizes, both of which in KH wavelength unit. The dashed line in panel (b) is a linear fit of the curvature radii in the KH wave trailing edge with the varying tetrahedron sizes (panel (c) of Figure 4.4.3) in the simulation in Chapter 4. This Figure is slightly different from Figure 6 in the published paper: the horizontal error bars of the data points in panel (b) are corrected.

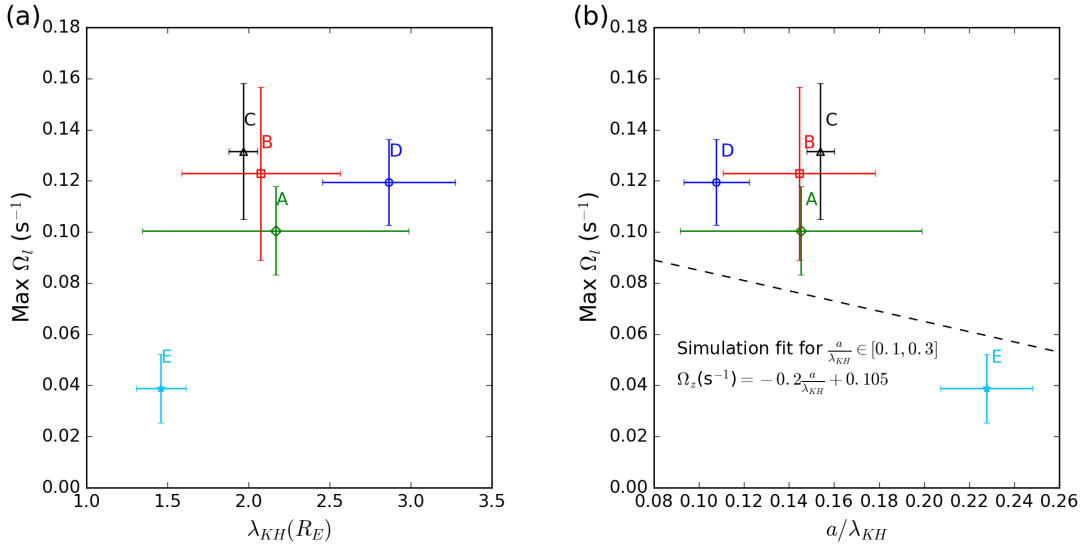

Figure 5.4.2: (a) Maximum vorticity versus KH wavelengths of the dominant modes in the five intervals A-E. (b) Maximum vorticity versus Cluster tetrahedron sizes in KH wavelength unit. The dashed line in panel (b) is a linear fit of the vorticity at the KH vortex centre with the varying tetrahedron sizes (panel (h) of Figure 4.4.3) in the simulation in Chapter 4.

multi-scales, thanks to variations in KH wavelengths for five intervals with approximately fixed tetrahedron size (opposite to the case in Chapter 4). To examine this, panel (b) of Figure 5.4.1 shows the measurements of minimum curvature radii against the tetrahedron sizes relative to the wavelength for the five intervals. The ratio of the minimum curvature radius to the wavelength is roughly increasing with the ratio of the tetrahedron size to the wavelength a/λ_{KH}. This shows that the minimum curvature radius measure is increasing with the relative tetrahedron size. The dashed black line represents a linear fit to numerical data in panel (c) of Figure 4.4.3 for curvature radii in the wave trailing edge, where the minimum curvature radius is typically found, resolved by the varying tetrahedron sizes, viz.

$$R_c/\lambda_{KH} = 1.24a/\lambda_{KH} + 0.035 \tag{5.1}$$

for their range $a/\lambda_{KH} \in [0.05, 0.25]$ where the linear dependence on the tetrahedron size is found. The data points from Cluster are roughly consistent with the linear fit from the simulation, which confirms the dependence of the curvature radius measure on the (relative) tetrahedron size. This plot illustrates the non-linearity of spatial variations of the magnetic field structures in observations as resolved by Cluster.

Figure 5.4.2 shows the relationships for the maximum vorticity versus KH wavelength in panel (a) and the maximum vorticity versus the ratio a/λ_{KH} in panel (b). There is a tendency for larger maximum vorticity for a longer wavelength, despite this relation is not so obvious in panel (a). In panel (b), we add a fit from the simulation of the vorticity at the KH vortex centre versus the tetrahedron size shown as a dashed line. Based on the simulation, the vorticity should yield the maximum value at the KH vortex centre (see Figure 4.4.7). This simulation fit is obtained from panel (h) of Figure 4.4.3 in Chapter 4, viz.

$$\Omega_z(\mathrm{s}^{-1}) = -0.2a/\lambda_{KH} + 0.105 \tag{5.2}$$

for their range $a/\lambda_{KH} \in [0.1, 0.3]$ where the linear dependence is found. The maximum vorticity from Cluster data in panel (b) generally follows the simulation fit. This shows that the vorticity is higher for a smaller ratio of a/λ_{KH} as expected.

The above comparison with the simulation assumed that the KH waves in the five intervals for this event have spatial variations governed essentially by their amplitudes (or wavelengths) and/or physical parameters (density, velocity jumps) controlling the KHI excitation. This is not entirely true as these waves can have other, possibly minor, spatial variations due to their non-linear evolution (rolled-up vortex signatures and other non-linear spatial variations). These waves are considered to be of remote origin [*Foullon et al.*, 2008] such that they are produced somewhere on the dayside where the conditions are KH-unstable [*Farrugia et al.*,

1998], e.g., where the shear angle between the IMF clock angle and the Earth's magnetic fields is low, and so the waves in the five intervals of different IMF clock angles do not originate at the same place and therefore have taken slightly different amount of time to develop before reaching Cluster. Consequently, these waves are in different stages of development when they are probed by Cluster. Of particular relevance is the simulation result (for fixed wavelength) that the average radius of magnetic curvature can become smaller when the KH wave evolves from linear to non-linear stages [*Ryu et al.*, 2000] (also see panel (f) of Figure 4.4.8). Since the intervals A (IMF clock angle = $36^o \pm 3^o$, λ_{KH} = $2.16 \pm 0.82\ R_E$) and B (IMF clock angle = $12^o \pm 10^o$, λ_{KH} = $2.07 \pm 0.49\ R_E$) in panel (b) of Figure 5.4.1 have the same ratios of a/λ_{KH}, we can attribute the differences to the impact of non-linear KH development on the radius of curvature. Here, the KH waves in interval B have smaller minimum R_c/λ_{KH} than that of the interval A. This is consistent with the other properties showing that the KH waves in the interval B are more developed than the waves in the interval A [*Foullon et al.*, 2008].

Higher (maximum) positive vorticity in longer wavelength KH waves (see Figure 5.4.2) is consistent with larger vortices found in KH simulations of the magnetopause (e.g., *Belmont and Chanteur* [1989]; *Miura* [1999]). In addition to the main positive vorticity expected on the dusk side, we have found the negative vorticity which is a secondary feature associated with rolled-up vortices (consistent with panel (b) of Figure 5.1.1). In theory, negative vorticity occurs after rolling up [*Gratton et al.*, 2009], and we would expect the negative vorticity layer between the positive vorticity layers of a rolled-up vortex core and an original shear layer (Section 4.4.2). However, from the observations [*Foullon et al.*, 2008], we know that not all five intervals contain rolled-up vortex signatures. Indeed, in interval E, the method picks up vorticity minima that are close to zero (see panels (c), (f), (i) of Figure 5.3.3), but still negative. This interval contains little wave activity and therefore should not be regarded as having any rolled-up signature. The strength of the negative vorticity increases with the solar wind speed (panel (f)), consistent with more developed KH waves as expected for higher velocity shear across the boundary layer. In addition, the magnitude of the (positive, negative) vorticity should be initially controlled by the vorticity scaling value $|\Omega| \sim |V_{sw}/\Delta L|$, where V_{sw} is the solar wind speed and ΔL is the thickness of the boundary layer (e.g., as in Section 4.4.2 of Chapter 4); the KH activity then amplifies/weakens this initial vorticity. Using the boundary layer thickness (ΔL) obtained by F08 in their Table 3, it can be shown that the scaling values of all intervals are in the order A $>$ C $>$ B $>$ D $>$ E that is in the same order as the negative vorticity in panel (f) of Figure 5.3.3. The relationship between the negative vorticity and the proton density (panel (i)) is consistent with simulation results in *Nakamura et al.* [2004]. There, the negative vorticity (referred as a reversed shear flow) only occurs when there

is a density jump across the shear layer. Since the density jump is modified by proton density on the magnetosheath side, the negative vorticity development is associated with solar wind proton density. This is confirmed by our result in panel (i) of Figure 5.3.3 as one can see that the negative vorticity tends to zero for lower proton density.

5.5 Summary

Observations of KH waves on 20 - 21 November 2001 made by Cluster are revisited using the four-spacecraft magnetic curvature and vorticity analyses. Several four-spacecraft signatures in magnetic curvature and flow vorticity of KH waves proposed in Chapter 4 are confirmed. We observe a rotation of curvature direction from sunward and earthward in the inner magnetospheric side to the opposite direction in the outer magnetospheric side across the wave trailing edges, consistent with the simulation. Rolled-up vortex signatures are further highlighted by the four-spacecraft tools complementary to previous studies using single spacecraft observations. We observe the magnetic field distortion against the vortical flow at the vortex centre. We also observe the negative vorticity layer adjacent to the positive vorticity of the vortex core of a rolled-up KH vortex where the LDFTS plasma is found. The confirmation of such vorticity variations is useful to assess whether identifying rolled-up KH waves in four-spacecraft observations may be applicable.

Local properties of the KH waves are characterised with changes in solar wind conditions. In particular, we found the smaller radius of magnetic curvature (stronger bending) and larger positive flow vorticity for lower IMF clock angle (longer wavelength KH waves). The average minimum curvature radii are compared for various ratios of the tetrahedron size to the wavelength. We have demonstrated observationally the dependence of the curvature radius on the tetrahedron size, consistent with non-linear spatial variations of magnetic structures resolved by nested cross-scale virtual spacecraft tetrahedrons in a numerical simulation. Finally, we confirm the importance of local conditions on the development of the negative vorticity as previously found in the simulations, such that the negative vorticity is associated with the density jump and strengthened with higher solar-wind proton density. We additionally find that it also strengthens with increasing solar wind speed.

In other words, there are three possible effects that are being detected in the parametric study in the various panels of Figure 5.3.3. The first one observed as linear relationships as seen in panels (a) and (b) could be caused by the scale size of the KH waves (controlled by the IMF clock angle) with respect to the tetrahedron size. The impact of the a/λ_{KH} ratio is summarised in Figure 5.4.1 (shown for the

minimum curvature radius). The second effect also observed as linear relationships in panels (f) and (i) could be due to the physical parameters that control the KHI excitation, e.g., density and velocity jumps across the shear interface or the vorticity scaling that is a characteristic of the boundary layer (associated speed and layer thickness). The third effect observed in the lack of linear relationship could be attributed to non-linear KH evolution. The negative vorticity (e.g., panel (c)) is one of the spatial variations expected to arise due to non-linear KH evolution. However, not all negative vorticity in the data can be taken as a signature of the rolled-up vortex, and there is no evidence that the strongest negative vorticity occurs in relation to non-linear KH evolution either. Further investigations to understand the development of negative vorticity would be needed, e.g., using the KH vortex frame in observational data, but they are beyond the scope of this study. While more data points are desirable for better statistics in the parametric survey (Section 5.3.3), we cannot conduct an ideal "controlled" experiment with unrelated KH events that may resemble in some aspects our selected event, but will always differ in solar wind / local plasma conditions and satellite relative locations and separations. The multi-scale analysis in this work has broad applications especially for cross-scale observations of complex magnetic and vortical flow structures, which are ubiquitous in the Earth's magnetospheric environments.

Chapter 6

Four-spacecraft analyses on small-scale structures of KH waves: MMS observations

Magnetopause KH waves are believed to mediate solar wind plasma transport via small-scale mechanisms that take place along the wave edges and in rolled-up vortices. In this Chapter, we will look into MMS observations of KH waves on 8 September 2015 and 5 May 2017 on the dayside dusk-flank and post-terminator dawn-flank magnetopause, respectively. Mid-latitude reconnection associated with KH waves was reported using remote signatures from the particle pitch angle distributions in the former event. We will apply the MCA technique to resolve magnetic topologies that may be consistent with the mid-latitude reconnection. We will show that the MCA finds weak evidence of reconnection, possibly because the scale size of the MMS tetrahedron is too small. We will further identify closed magnetic structures, characterised by counter-streaming electrons, in the local reconnection exhausts in the two events; the latter of which will be identified as a magnetic-island-type plasmoid. We will also apply the vorticity technique using electron data. The resolved electron vorticity will reveal a vortical structure of the plasmoid in the electron scale. We will additionally identify a flux transfer event (FTE) during the KH activity on 5 May 2017. It will be shown that the MCA readily gives an impression of the in-situ FTE structure consistent with a classical FTE model, such that the magnetic curvature directs inward while the curvature radius is increasing towards the FTE core. This study is useful to understand small-scale structures in KH waves. Applications of the four-spacecraft tools will be proved to be helpful in analysing the local magnetic topology and flow structure of the KH waves in small-scales.

6.1 Introduction

Launched in March 2015, MMS is the NASA four-spacecraft mission that is aimed at the study of magnetic reconnection, a fundamental process in plasmas, using the Earth's magnetospheric environment as a laboratory. Due to the small-scale nature of reconnection, MMS tetrahedral formation is much smaller than Cluster with inter-spacecraft separations between 7 and 400 km that are comparable to the electron and ion inertial lengths. Moreover, due to the fast time-scale of reconnection, MMS has a very high time resolution down to milliseconds. The small tetrahedral formation of MMS allows us to study magnetopause KH waves at fine spatial-temporal scales.

We have selected two KH events on the magnetopause where periods of burst (highest resolution) data were made by the MMS Scientist-In-The-Loop team. The first event was detected on 8 September 2015 with about 2 hours of activity on the dayside dusk-flank magnetopause. This event was reported in detail by *Eriksson et al.* [2016]. The KH waves were found to be in the linear stage [*Vernisse et al.*, 2016]. Using KH wavelength of $2.56 \pm 0.3\ R_E$ reported in their paper, the ratio of the tetrahedron size of $150 - 185$ km (a) to the KH wavelength (λ_{KH}) is around 0.01. This ratio is in the small range of the tetrahedron size dependence, $a/\lambda_{KH} \in [0.00625, 0.075]$, resolved in the simulation (see Chapter 4). We do not expect the results in Chapter 4 to be accurate at this scale because the simulation is MHD (while MMS would detect kinetic effects). Although the grid cell length of the simulation is 150 km which is comparable to the MMS separation in this KH event, the time-step of the simulation (t_0) of 4 seconds is much slower than the MMS time resolution.

The second event was detected on 5 May 2017 with about 4 hours of activity on the post-terminator dawn-flank magnetopause. Considering the evolution of KH waves with the distance away from the subsolar point (see Figure 1.3.3), the second event is expected to be in its non-linear stage and have a longer wavelength than that in the first event. The KH wavelength can become longer when propagating away from the subsolar point due to a convective motion (λ stretching effect) [e.g., *Wu*, 1986; *Mills et al.*, 2000]. In the non-linear stage, KH wavelengths can become longer due to inverse cascade [e.g., *Belmont and Chanteur*, 1989; *Thomas and Winske*, 1993]. Since the tetrahedron size is very small compared to the KH wavelength, we do not aim to resolve the (macroscopic) spatial properties of the waves as done in Chapter 5 for Cluster observations. Instead, we aim to analyse small-scale structures that reside in the waves.

KH waves are believed to allow solar-wind entry via small-scale mechanisms that operate along the wave edges and through their vortices. MMS enables us to investigate small-scale mechanisms associated with the waves, which would lead to a better understanding of how the KH waves mediate solar-wind plasma trans-

port. The main mechanism that allows plasma transport during the KH activity is proposed to be magnetic reconnection (see Section 1.3). Intense current sheets may form along the trailing edges of KH waves due to oppositely directed in-plane magnetic fields, together with the dominant B_z, across the magnetopause [e.g., *Pu et al.*, 1990; *Knoll and Chacón*, 2002]. The presence of the KH instability amplifies the in-plane magnetic fields by its vortical flow which can further compress the current sheets to become thinner than the electron inertial length [*Nakamura et al.*, 2008, 2013; *Karimabadi et al.*, 2013], hence becoming susceptible to reconnection. These current sheets form early in the linear stage of KH development and persist through the non-linear stage [*Nakamura et al.*, 2013]. *Eriksson et al.* [2016] reported direct observations of reconnection along the wave trailing edges (Type-I VIR) (left panel of Figure 1.3.1) using MMS. *Nakamura et al.* [2017] studied the same event using kinetic simulations with empirical inputs from MMS. They showed that the conditions in this event marginally satisfy the KH instability onset condition in which rolled-up vortices can develop. They concluded that the KH waves at the MMS locations are in the early non-linear growth phase of the instability, in which the ion-scale reconnection signatures in the observations were successfully reproduced.

A more complex type of reconnection induced by KH waves was also reported in this event by *Vernisse et al.* [2016]. Using particle signatures, *Vernisse et al.* [2016] identified additional reconnection signatures coming remotely from higher latitudes, consistent with mid-latitude reconnection model proposed by *Faganello et al.* [2012a]. The model proposes that magnetic reconnection is triggered at mid-latitudes in the southern and northern hemispheres, about 30,000 km away from the equatorial plane where the KH waves are developing. Using directionality of particle pitch angle distribution, they distinguished between particles coming from the northern and southern hemispheres. This model involves twisting of the magnetic fields by the KH instability in large-scales as shown in Figure 6.1.1. The twisting of magnetic fields at mid-latitude induces thin current sheets that are susceptible to reconnection [e.g., *Faganello et al.*, 2012a; *Borgogno et al.*, 2015; *Ma et al.*, 2017]. In the first section of this Chapter, we aim to resolve in-situ magnetic topologies using the four-spacecraft tools in order to find supporting evidence of the remote reconnection reported by *Vernisse et al.* [2016].

In numerical simulations, magnetic islands are commonly produced by magnetic reconnection for both anti-parallel and component (guide-field) reconnection types. One theory of how reconnection contributes to the solar-wind transport by the KH waves is that it produces magnetic islands that later evolves into the vortices, which enhance plasma mixing [*Nakamura et al.*, 2011, 2013]. However, observations of magnetic islands are scarce. Magnetic islands in the KH waves were first identified using THEMIS by *Eriksson et al.* [2009]. They were found

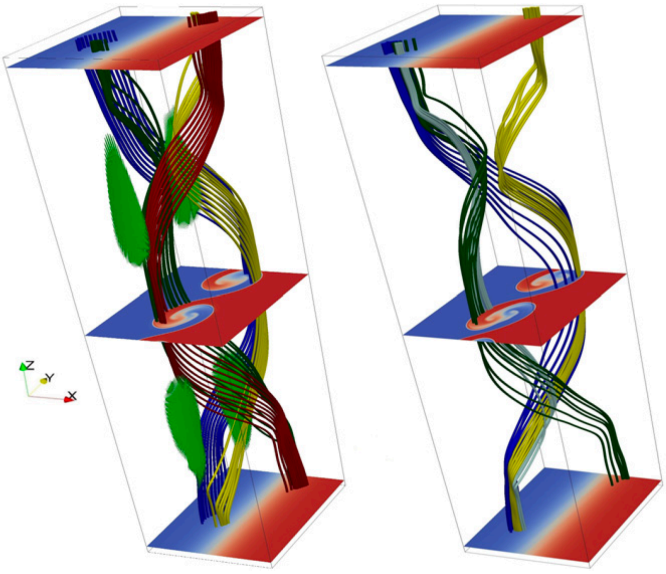

Figure 6.1.1: Magnetic field configuration of mid-latitude reconnection induced by KH waves. (left) Before reconnection and (right) after reconnection. While the magnetic fields of the solar wind (blue) and magnetosphere (red) are anchored to high latitudes (top and bottom XY-planes) which are KH stable, they undergo twisting along with the KH waves at the equatorial plane (middle XY-plane). Consequently, current sheets (green region) are formed due to the sheared magnetic fields at mid-latitudes. The mid-latitude reconnection results in a change of magnetic topology as shown in the right panel. Courtesy of *Faganello et al.* [2012a].

to develop during the growth phase of the KH waves detected on the dayside dusk-flank magnetopause. Magnetic islands were also studied near dayside reconnection sites under southward IMF conditions using 9 years of *Cluster* data by *Vines et al.* [2017]. However, high-resolution observational evidence of magnetic islands in the vicinity of KH waves does not yet exist. We are looking into the KH events observed by MMS in which there exist particle signatures that are indicative of magnetic islands.

There may be some confusion in terminology since different terms may be used to describe the same structures by different communities. *Ieda et al.* [1998] define a ``plasmoid" as a structure with rotating magnetic fields and enhanced total pressure in their magnetotail plasma sheet study. They further categorise two types of plasmoids depending on whether magnetic or plasma pressure mainly contributes to the enhanced total pressure. If plasma pressure is dominant, the plasmoid is of a magnetic-island type. If magnetic pressure is dominant, the plasmoid is of a flux-rope type. In literature, there is sometimes no distinction between the two types of the plasmoids; they are commonly referred as magnetic islands. We will follow the terms in *Ieda et al.* [1998] since they are more specific on the pressure contribution.

In the dawn-side evolved KH event, there is a distinct plasma signature consis-

tent with a Flux Transfer Event (FTE). FTEs are characterised by a bipolar magnetic variation in the magnetopause normal direction (B_N) [*Russell and Elphic*, 1978]. FTEs are usually observed downstream of dayside or cusp reconnection sites and are believed to drive geomagnetic disturbances [e.g., *Russell and Elphic*, 1979; *Lockwood et al.*, 1995]. FTEs are proposed to be generated due to unsteady reconnection in the vicinity of single [e.g., *Scholer*, 1988] or multiple X-line reconnection [e.g., *Lee and Fu*, 1985; *Raeder*, 2006]. However, the formation of FTEs in the context of KH waves is not yet known. We will be applying the four-spacecraft analyses on this FTE to resolve its spatial properties.

Previous magnetic island and FTE observations have been commonly studied using the MVA technique or reconstructed using Grad-Shafranov (GS) like equations [*Sonnerup et al.*, 2006] that are applicable to any number of spacecraft. GS reconstruction was used to produce a map of the FTE cross-section and estimate the magnetic flux [e.g., *Sonnerup et al.*, 2004; *Hasegawa et al.*, 2006]. However, the method requires magnetohydrostatic and time stationary assumptions of the structure. Using four-spacecraft, multiple applications of the timing method along an FTE crossing were used to estimate the orientation of a flux rope by *Zhou et al.* [2006]. *Shen et al.* [2007] first applied the MRA technique, an adaptation of the MCA technique, on magnetotail flux ropes using Cluster observations. *Yang et al.* [2014] applied the MCA technique on magnetic flux ropes in the magnetotail observed by Cluster and found that curvature radii of the flux ropes near their axis centres are large. Multiple applications of the MVA technique were also used to sketch substructure of the FTE and the magnetopause bulging due to the FTE in *Hwang et al.* [2016]. Since the MMS mission has a very high time-resolution, it enables us to apply four-spacecraft tools which can reveal fine details of these magnetic structures. However, such studies are still limited.

The two KH events presented in this Chapter are in different stages of evolution which may shed light on the evolution of small-scale structure associated with magnetopause KH waves. We describe three closed magnetic structures with different qualitative characteristics. This Chapter includes detailed analyses of (1) local and remote reconnection in Section 6.4, (2) an isolated FTE during KH activity in Section 6.5, and (3) local reconnection and its associated magnetic island in Section 6.6. We provide detailed analyses of small-scale structures that would be useful for a better understanding of their roles in the context of magnetopause KH waves.

6.2 Instrumentation and Methodology

MMS carries multiple instruments on board. Specifically, we utilise magnetic field data from the Fluxgate Magnetometer (FGM) [*Russell et al.*, 2016] and plasma

moments from Fast Plasma Investigation (FPI) [*Pollock et al.*, 2016]. Data are retrieved and visualised using CLWeb at Institut de Recherche en Astrophysique et Planétologie (IRAP). The plasma moments include ion number density, ion and electron bulk velocity, ion and electron pitch angle distributions, ion and electron temperature, and total (ion and electron) pressure. FGM instruments have a sampling time resolution up to 1 millisecond in the burst mode. FPI instruments sample ions up to every 150 milliseconds and electrons up to 30 milliseconds. For the 5 May 2017 event, FPI from MMS3 spacecraft is not available in the burst mode (but available in the fast mode) after 20:17 UT. As a result, we cannot calculate ion flow vorticity which requires ion bulk velocities from all four-spacecraft in the burst mode after that specific time. We also obtain upstream solar wind conditions from NASA High-Resolution OMNI (HRO) data using CLWeb.

We calculate magnetic curvature and electron flow vorticity from the MCA and vorticity analysis techniques respectively (see Chapter 3). Current density is calculated from the curlometer technique that is applied to the FGM data. Note that the FPI instruments are also used to calculate the current density using the relative motion of ions and electrons bulk, $\mathbf{J} = en_e(\mathbf{V_i} - \mathbf{V_e})$. These two procedures for calculating the current density give very similar results, indicating very high accuracy of the plasma moment measurements of the FPI instruments. MMS1 is used as the reference spacecraft. Outputs of the four-spacecraft technique are calculated at the MMS tetrahedron barycentre.

6.3 Overview of Events

6.3.1 8 September 2015 Event

On 8 Sept 2015, the MMS spacecraft observed quasi-periodic variations in magnetic and plasma moments consistent with KH waves while moving across the LLBL from post-noon towards dusk terminator [*Eriksson et al.*, 2016]. Orbit and tetrahedral formation of the MMS are shown in Figure 6.3.1 in the GSE coordinates. The average MMS barycentre location during 9 and 12 UT is $[4.9, 7.4, -4.6]R_E$ in the GSM system, which is on the dayside, dusk-flank magnetopause. The inter-spacecraft separation is between 150 and 185 km. The tetrahedron quality factor is 0.93 that is indicative of tetrahedral formation close to a regular tetrahedron.

Figure 6.3.2 shows an overview of upstream solar wind conditions from HRO during 9 and 12 UT in panels (a) - (c). Panel (a) shows northward IMF clock angle with an average value of $24^o \pm 8^o$ in the GSM system. The average upstream magnetic field in panel (b) is $B_y = 6.4 \pm 1.8$ nT and $B_z = 15.1 \pm 1.7$ nT (B_x was not available) in the GSM system. The average solar wind speed in panel (c) is $|\mathbf{V}| = 509 \pm 6$ km s^{-1}. Other parameters (not shown) include average Alfvén

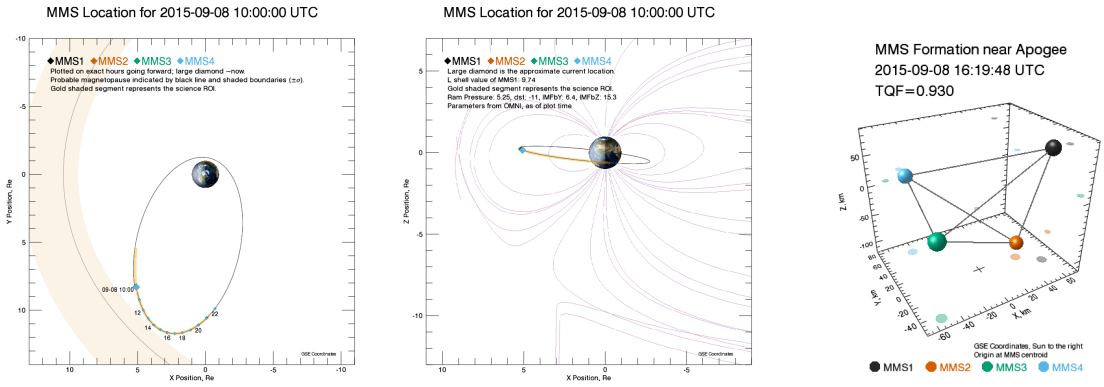

Figure 6.3.1: MMS orbit and formation on 8 September 2015. (left) and (middle): MMS orbit in XY-view and XZ-view respectively, and (right) MMS tetrahedral formation.

Mach number, $M_A = 3.9 \pm 0.3$, plasma beta, $\beta_i = 0.15 \pm 0.02$, proton density, $n_i = 10.3 \pm 1.6$ cm^{-3}, and solar wind dynamic pressure, $P_{dyn} = 5.3 \pm 0.7$ nPa. The Alfvén Mach number is obtained from the CLweb where it is automatically calculated (although B_x cannot be displayed for some reason).

Panels (d) - (i) show MMS1 observations at the average location $[5.0, 7.4, -4.6]$ R_E in the GSM coordinates. Ion and electron energies are shown in panels (d) and (e), respectively. *Eriksson et al.* [2016] characterised transition regions as follows. MMS1 entered the boundary layer (BL), characterised by the distinctive quasi-periodic variations, at around at around 9:21 UT (the first vertical dashed line) and exited at 11:27 UT (the third vertical dashed line). In the BL, there are two intervals with different levels of the activity, clearly seen in magnetic fields in panel (f) and velocity fields in panel (g). The activity is low until 10:07 UT (the second vertical dashed line), characterised here as the inner region of the BL, and higher after that, characterised here as the outer region of the BL. Ion number density in panel (h) and ion temperature in panel (i) show that MMS1 was in the magnetospheric side (hot and tenuous) before entering the BL and then exited to the magnetosheath side (cold and dense). The magnetosphere, inner region of the BL, outer region of the BL, and magnetosheath regions are marked as blue, green, yellow, and orange bars in the bottom of Figure 6.3.2.

Eriksson et al. [2016] explored the observed KH instability using the linear KH growth theory (e.g., equation 1.3) and *Vernisse et al.* [2016] discussed that the KH waves in this event are in the linear stage. Using measurements from the inner boundary layer and magnetosheath, the calculation by *Eriksson et al.* [2016] resulted in $(\gamma/k)^2 > 0$ for $\theta = \theta_0 \pm \Delta\theta$, with $\Delta\theta \sim 17^o$, where θ is the angle between **k** and the X-Y plane of the flow shear. The KH wavelength was estimated to be $\lambda_{KH} = 2.56 \pm 0.3$ R_E, using the in-plane ion speed $V = 258 \pm 35$ km s^{-1} that is in agreement with the de-Hoffman frame velocity. The KH wave period was estimated to be 63.3 s.

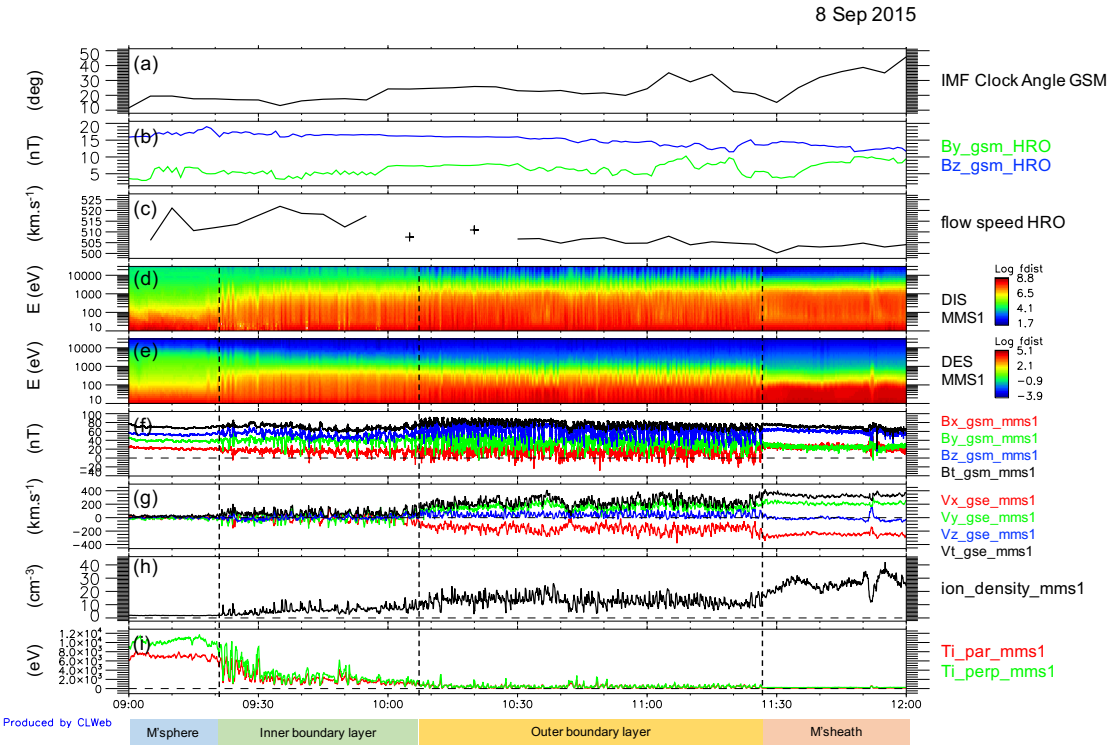

Figure 6.3.2: Overview of the 8 September 2015 event during 9:00 UT and 12:00 UT from HRO (panels (a) - (c)) and MMS 1 (panels (d) - (i)): (a) IMF clock angle, (b) upstream magnetic fields, (c) upstream ion flow speed, (d) ion energy, (e) electron energy, (f) magnetic fields, (g) ion bulk velocity, (h) ion number density, and (i) ion temperature.

6.3.2 5 May 2017 Event

On 5 May 2017, the MMS made observations of quasi-periodic variations of various plasma parameters consistent with KH waves during 19:30 and 23:30 UT beyond the post-terminator on the dawn-side flank magnetopause. Figure 6.3.3 shows orbit and formation of the MMS in the GSE coordinates. The average location of MMS barycentre is $[-13.9, -18.4, -5.2]$ R_E in the GSM system. The tetrahedron quality factor is 0.84 which is indicative of tetrahedron formation close to a regular tetrahedron. KH waves detected at such location are expected to be more developed than at the pre-dawn/dusk terminator [e.g., *Li et al.*, 2012].

Figure 6.3.4 shows upstream solar wind conditions from HRO during 16 and 24 UT in panels (a) - (c). Panel (a) shows IMF clock angle that is mostly northward throughout the duration with an average value of $-9.2^o \pm 5.5^o$ in the GSM system. The average magnetic field in panel (b) is $B_y = -1.5 \pm 1.2$ nT and $B_z = 6.9 \pm 0.3$ nT (B_x is not available) in GSM coordinates. The average flow velocity in panel (c) is $|\mathbf{V}| = 383 \pm 9$ km s^{-1}. Other parameters (not shown) include average Alfvén Mach number, $M_A = 4.8 \pm 0.7$, plasma beta, $\beta_i = 0.4 \pm 0.1$, proton density, $n_i = 3.8 \pm 0.9$ cm^{-3} and solar wind dynamic pressure, $P_{dyn} = 1.1 \pm 0.2$ nPa.

Panels (d) - (k) show MMS1 observations at the average location $[-13.9, -18.3, -5.2]$

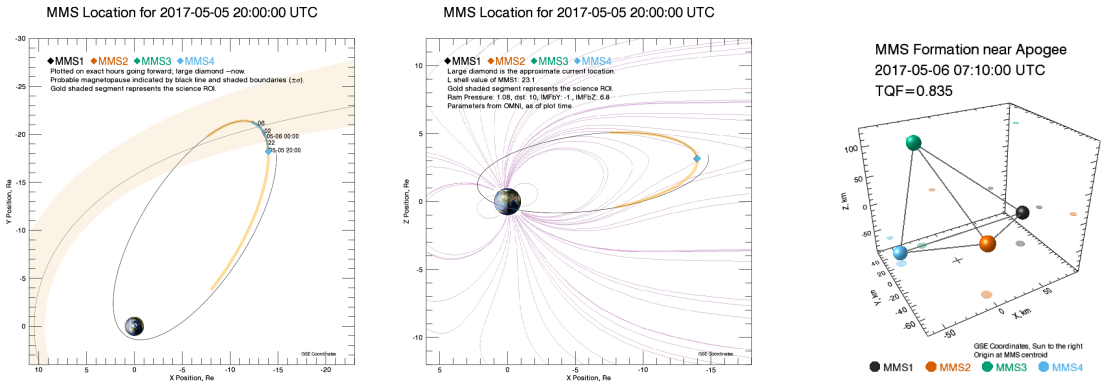

Figure 6.3.3: MMS orbit and formation on 5 May 2017. (left) and (middle): MMS orbit in XY-view and XZ view respectively, and (right) MMS tetrahedral formation.

R_E in the GSM system. Panels (d) and (e) show ion and electron energies, respectively. They show quasi-periodic fluctuations but overall decreasing high energy particle fluxes, indicating that MMS1 was transiting from the magnetosphere proper to the magnetosheath proper. The magnetosphere proper (from 16:00 to 17:05 UT) is characterised by static flow in panel (i), low ion density in panel (j), and high ion temperature in panel (k). The magnetosheath proper (from 23:20 UT to 24 UT) is characterised by faster flow (panel (i)), higher ion density (panel (j)), and lower ion temperature (panel (k)). Panel (f) shows magnetic field strength B_t which shows variable but gradually increasing strength from ~ 10 nT in the magnetosphere to ~ 16 nT in the magnetosheath. The increasing magnetic field strength is mainly contributed by the magnetic field component B_x as shown in panel (g). In the transition region, between the first and fourth vertical dashed lines, we may characterise regions of the boundary layer as follows. The component B_x (panel (g)) fluctuates around a negative value from 17:05 UT (first vertical dashed line) to around 19:40 UT (second vertical dashed line). The component B_x then fluctuates around zero until 21:50 UT (third vertical dashed line). After that, the B_x fluctuates around a positive value until exiting to the magnetosheath at 23:20 UT. These three intervals may be characterised as the magnetospheric, magnetopause, and magnetosheath boundary layers, respectively. We mark those regions with coloured bars at the bottom of Figure 6.3.4.

6.4 KH-wave associated mid-latitude reconnection

Besides the local reconnection reported by *Eriksson et al.* [2016] in the 8 September 2015 event, *Vernisse et al.* [2016] identified additional signatures indicating particles coming from reconnection at higher latitudes. A unidirectional flux of heated electrons in the magnetosheath boundary layer just outside the magnetopause was used to infer opened topology of the Earth's magnetic field due to

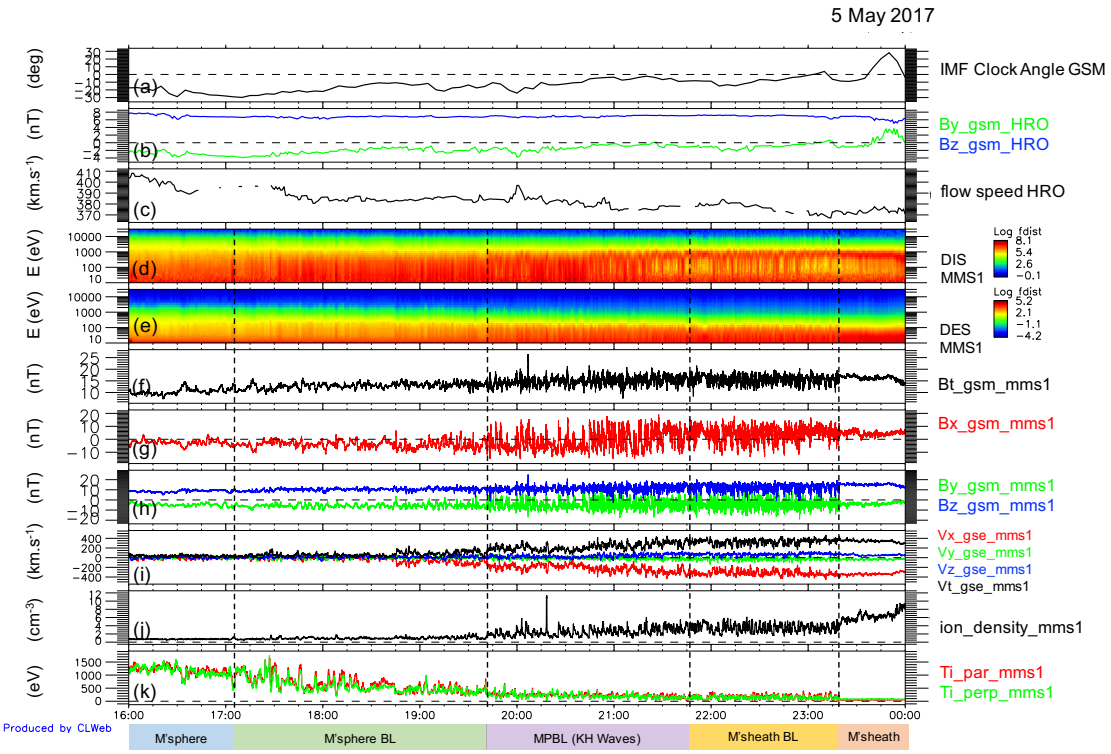

Figure 6.3.4: Overview of the 5 May 2017 event during 16 UT and 24 UT from HRO (panels (a) - (c)) and MMS 1 (panels (d) - (i)): (a) IMF clock angle, (b) upstream magnetic fields, (c) upstream ion flow speed, (d) ion energy, (e) electron energy, (f) magnetic field strength (B_t), (g) magnetic field component B_x, (h) magnetic field components B_y and B_z, (i) ion bulk velocity, (j) ion number density, and (k) ion temperature.

reconnection at high latitudes [*Onsager et al.*, 2001; *Lavraud et al.*, 2005, 2006]. Parallel and anti-parallel streaming electrons are indicative of the reconnection below (in the southern hemisphere) and above (in the northern hemisphere) the spacecraft at low latitude, respectively. *Vernisse et al.* [2016] interpreted the uni-directional flux of electrons during the KH event in the magnetosheath boundary layer to be due to mid-latitude reconnection induced by the KH waves. Magnetic curvature was resolved near magnetic reconnection sites in *Cluster* observations of the magnetotail [*Runov et al.*, 2003; *Runov et al.*, 2006]. Magnetic curvature was found to correspond to the ion jet such that the curvature magnitude is non-zero near the X-line and the curvature direction is the same as that of the ion jet. From our speculation, there is a delay in the curvature signature for about 5 seconds in the Cluster event reported by *Runov et al.* [2003]. We may explain this delay to be because the magnetic curvature is calculated at the tetrahedron barycentre while the ion jet is seen at one of the spacecraft that situates more upstream than the tetrahedron barycentre. In addition, simulations of the mid-latitude reconnection suggested magnetic field twisting in the opposite direction to the vortical flow on either side of the boundary (see Figure 6.1.1). Considering applications of the MCA on the mid-latitude reconnection interval, one should see

magnetic curvature associated with (1) the direction of the electron streams and (2) magnetic field twisting consistent with the simulations. In our work with MMS, we choose one of the remote reconnection events in *Vernisse et al.* [2016] to see if the MCA would support the remote particle signature evidence.

Between 10:20:56 UT and 10:21:02 UT, the four MMS were observed to transit from the magnetospheric side to the magnetosheath side of the magnetopause boundary layer (MPBL), crossing a trailing edge part of the KH wave [*Vernisse et al.*, 2016]. This crossing was reported for; first, a reconnection exhaust observed locally in the boundary [*Eriksson et al.*, 2016], and, second, a remote reconnection observed in the magnetosheath [*Vernisse et al.*, 2016]. We will first describe properties of this boundary layer crossing and its associated local and remote reconnection. We will then investigate the crossing using the four-spacecraft tools.

Figure 6.4.1 shows MMS1 observations between 10:20:51 UT and 10:21:07 UT when the spacecraft transits from the magnetospheric to magnetosheath sides. The average MMS1 position is at $[5.0, 8.7, 0.1]\ R_E$ in the GSE system. MMS1 was in the magnetospheric side until around 10:20:57.5 UT (marked as t_1) and in the magnetosheath side from around 10:21:00 UT (marked as t_3). The two sides of the MPBL are characterised by different ion number density (n_i) in panel (b) and ion temperature (T_i) in panel (g). The magnetospheric side is hot ($T_1 = 934 \pm 132$ eV) and tenuous ($n_1 = 12.7 \pm 1.7$ cm^{-3}) while the magnetosheath side is cold ($T_2 = 217 \pm 12$ eV) and dense ($n_2 = 19 \pm 3$ cm^{-3}). The ion inertial length ($d_i = c/\omega_{pi}$, where ω_{pi} is the ion plasma frequency) in the interval 10:20:56 - 10:21:02 UT is 56 ± 9 km. These two sides are also characterised by electron and ion pitch angle distributions in panels (e) and (f) respectively. The electron pitch angle distribution (ePAD) shows 0^o and 180^o peaks, called bidirectional fluxes, in the magnetospheric side as expected for closed magnetospheric fields. Ion pitch angle distribution (iPAD) peaks at 90^o as the flow in the magnetosheath travels tailward, directed perpendicularly to the northward magnetic fields.

Since electrons travel faster than ions, one can see the electron boundary layer (EBL) extending to the magnetosheath during 10:20:59 UT (before t_2) and 10:21:00 UT (t_3) in panel (e). In this region, we also observe, first, the strong bidirectional fluxes (also called counter-streaming electrons in literature) of ePAD in panel (e) and the strong parallel electron heating (red) in panel (h), marked as t_2. The counter-streaming electrons are indicative of a closed magnetic structure [e.g., *Gosling et al.*, 1987], such that electrons are trapped and therefore travel in parallel and anti-parallel directions. This closed structure is not a plasmoid because there is no TPE (the sum of plasma and magnetic pressures) associated with the counter-streaming electrons. In the magnetosheath (after 10:21:00 UT, t_3), MMS1 observes an extended interval of unidirectional fluxes of ePAD peaking

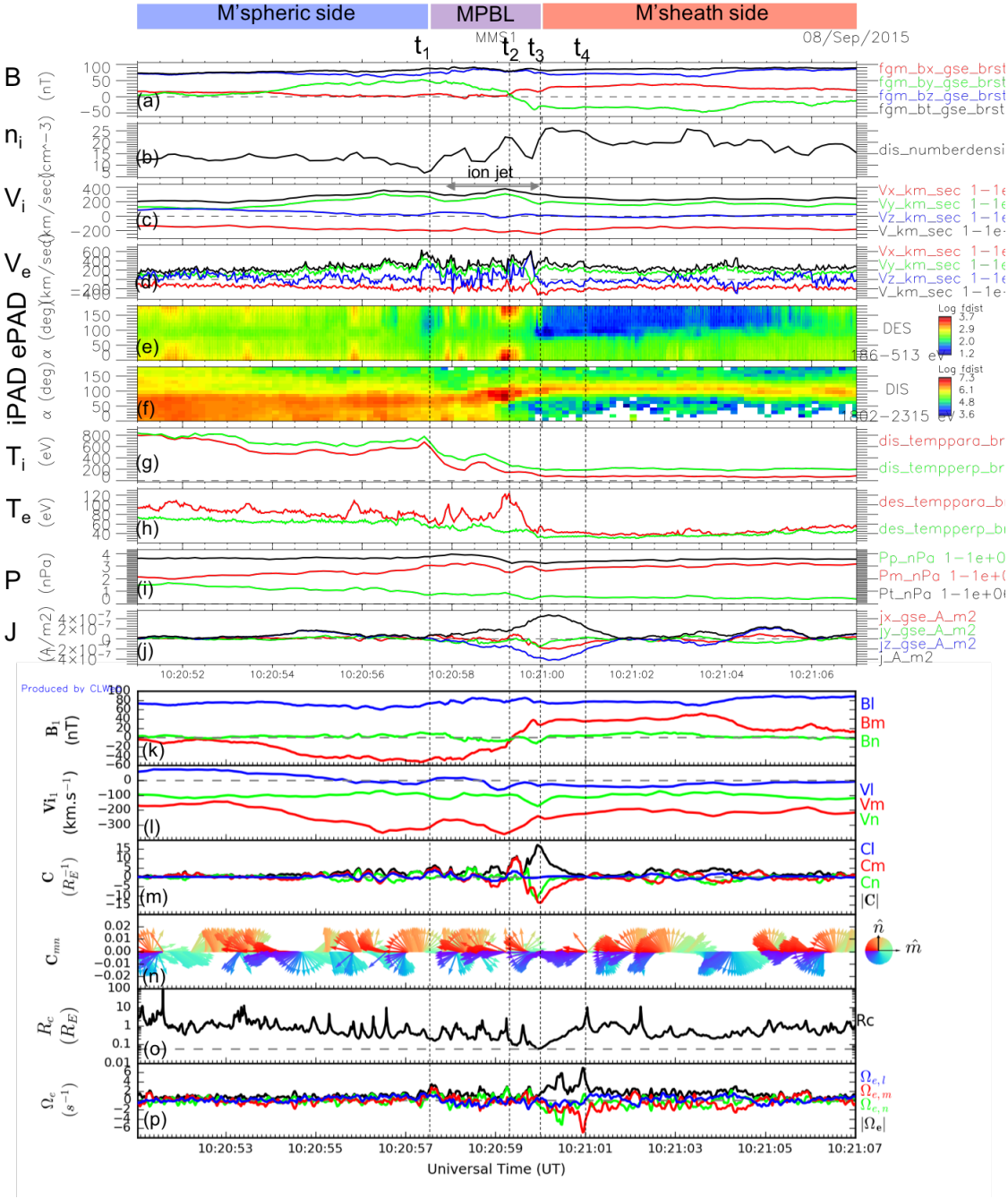

Figure 6.4.1: Overview of a magnetopause crossing during 10:20:51 UT and 10:21:07 UT on 8 September 2015: (a) magnetic fields , (b) ion number density, (c and d) ion and electron bulk velocity in GSE coordinates, (e and f) electron and ion pitch angle distributions, (g and h) parallel (green) and perpendicular (red) components of ion and electron temperatures, (i) plasma pressure (green), magnetic pressure (red), and total pressure (black), (j) current density in GSE coordinates, (k, l, m) magnetic field, ion bulk velocity, and magnetic curvature components in the LMN coordinates, respectively, (n) 2-D normalised curvature projection in the $M - N$ plane, (o) radius of curvature, and (p) electron vorticity.

towards 0^o in panel (e). *Vernisse et al.* [2016] interpret these parallel streaming electrons as the magnetospheric population that leak and stream through the open magnetosheath fields possibly due to reconnection at remote locations. We will later investigate properties of magnetic topologies, if there are any, associated with this remote reconnection.

At the MPBL between 10:20:57.5 UT (t_1) and 10:21:00 UT (t_3), a magnetic rotation is visible in panel (a) in B_y component (green) where it changes from positive to negative. In this interval, an ion jet is observed in V_y (green) in panel (c) where the ion bulk velocity is higher than the background flow ($\Delta V_y > 0$), denoted by a two-headed grey arrow. To better see the magnetic rotation and ion jet, we transform the magnetic and ion velocity fields into the local boundary LMN coordinates. In this coordinate system, **n** is perpendicular to the local magnetopause boundary obtained from a cross product of the averaged magnetic fields on either side of the boundary: $\mathbf{n} = \langle B_1 \rangle \times \langle B_2 \rangle / |\langle B_1 \rangle \times \langle B_2 \rangle|$ where $\langle B_i \rangle$, $i = 1, 2$, are the time-averaged magnetic fields. The sign of **n** is chosen such that it is directed away from the Earth. **l** is obtained from a cross product of **n** and the maximum variance direction found from the MVA technique, which is about northward ($+Z_{gse}$). **m** completes the right-hand orthogonal system which is generally along the reconnected field direction. For this boundary crossing, we choose 7 seconds time-window on either side of the boundary at 10:20:59.2 UT (marked as t_2). The transformation is found to be $L = [0.213, -0.005, 0.977]$, $M = [0.326, -0.942, -0.076]$, $N = [0.921, 0.334, -0.199]$ in the GSE coordinates. The projected magnetic and ion velocity fields in the LMN coordinate system are shown in panels (k) and (l), respectively. The magnetic rotation around the boundary is now clearly seen in B_m component (red) where it symmetrically changes from -40 nT to 40 nT. The ion jet is observed in V_m (red) component where $\Delta V_m \sim -150$ km.s^{-1}. We sketch the structure of this local reconnection with the described magnetic rotation and ion jet in Figure 6.4.2.

To illustrate this magnetopause crossing, we follow the time labels in Figure 6.4.1 from t_1 to t_4. We also mark these time labels in Figure 6.4.2 corresponding to those in Figure 6.4.1. A possible spacecraft trajectory is shown as a grey dashed arrow in Figure 6.4.2 described as the following. At t_1, MMS1 first encountered the magnetospheric field $B_m < 0$ (blue arrow). Then it crosses the ion jet $\Delta V_m < 0$ and the closed magnetic structure (the counter-streaming electrons in panel (e) of Figure 6.4.1) at t_2. At t_3, the spacecraft observed the anti-parallel ePAD in the EBL (as seen in panel (e) of Figure 6.4.1) associated with electrons travelling away from the reconnection site, opposite to the newly reconnected field line (purple). The sign of the ion jet and the direction of electrons adjacent to the EBL are indicative of the spacecraft trajectory with respect to the reconnection site, e.g., the spacecraft would observe a positive ion jet ($\Delta V_m > 0$) and parallel

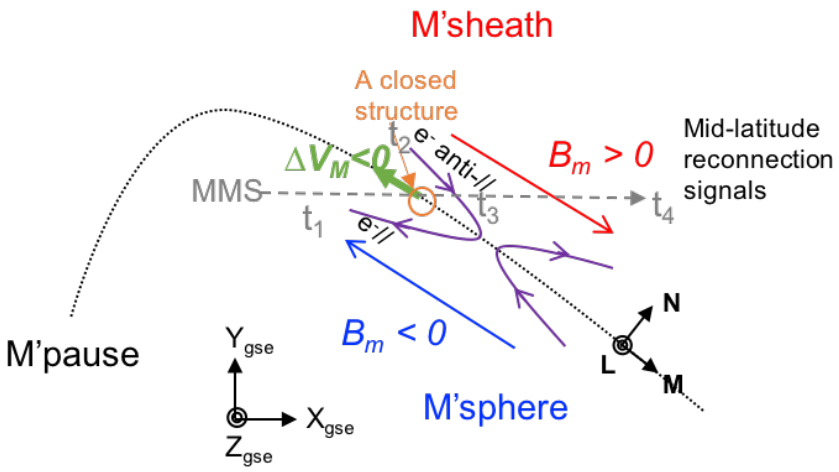

Figure 6.4.2: A schematic sketch of the magnetopause crossing in Figure 6.4.1 in the local boundary LMN coordinates, adapted from *Vernisse et al.* [2016]. Solid lines with open arrows represent magnetic field lines. Grey dashed line represents a possible MMS trajectory going from t_1 to t_4 as noted in Figure 6.4.1. The spacecraft encounters the magnetospheric magnetic field $B_m < 0$ (blue arrow) at t_1, the ion jet $\Delta V_m < 0$ (green thick arrow) at t_2, the electron boundary layer with anti-parallel ePAD (see panel (e) of Figure 6.4.1) in the magnetosheath magnetic field $B_m > 0$ (red arrow) at t_3, and the mid-latitude reconnection signals at t_4 (see Figure 6.4.3). At t_2, the spacecraft encounters a closed magnetic structure characterised by the counter-streaming electrons as seen in panel (e) of Figure 6.4.1.

ePAD adjacent to the EBL if it were travelling southward of the reconnection site (not shown). MMS1 then exits to the magnetosheath after t_3 where $B_m > 0$ (red arrow) is observed. As previously mentioned, the spacecraft observed parallel streaming electrons indicative of a remote reconnection around t_4. We further illustrate this scenario in Figure 6.4.3, adapted from *Vernisse et al.* [2016].

Figure 6.4.3 shows a schematic sketch of the remote reconnection associated with the KH waves in a global view. The KH waves detected by the MMS in the equatorial plane are shown as a slab in the $X - Y$ plane in the GSE coordinates. Blue and red thick lines represent magnetic fields threading through the KH waves in the equatorial plane in the magnetospheric (blue) and the magnetosheath (red) sides, respectively. White dashed arrow in the slab represents the assumed MMS trajectory going from t_1 to t_4 (the same as those in Figures 6.4.1 and 6.4.2). MMS1 detected the parallel streaming electrons at around t_4 after crossing the KH wave trailing edge. These parallel streaming electrons (thick green arrow) are coming from mid-latitude reconnection (green circle) in the southern hemisphere. The direction of the streaming electrons are indicative of locations of the mid-latitude reconnection, e.g., they would stream in the anti-parallel sense if the reconnection happens in the northern hemisphere. Since this remote reconnection changes the magnetic topology, we apply the MCA technique to see magnetic curvature properties that may be associated with the remote reconnection. We expect non-

zero magnetic curvature in the north-south (**l**) direction for the magnetic topologies associated with the remote reconnection.

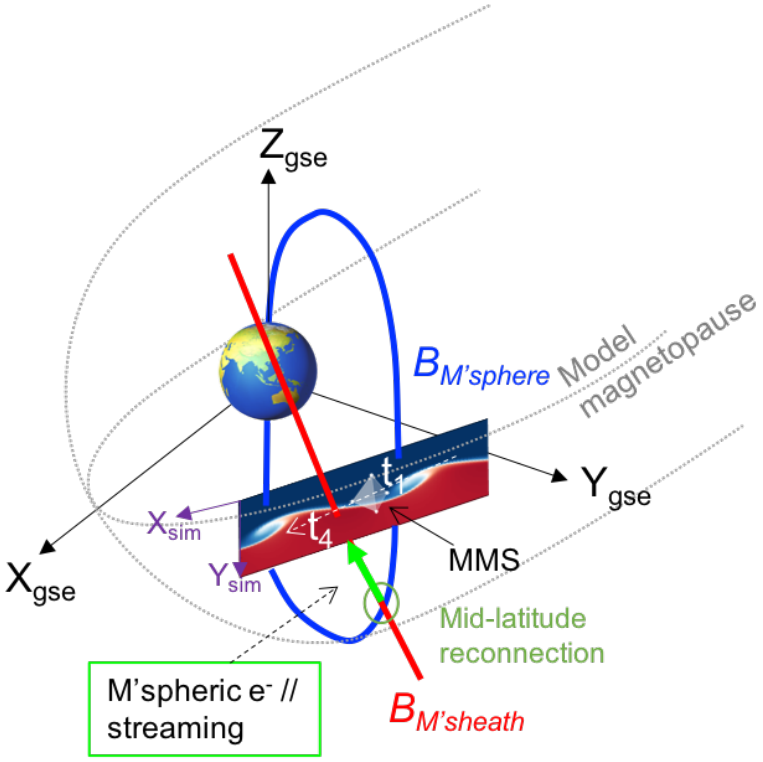

Figure 6.4.3: A schematic sketch of magnetic topologies associated with the remote reconnection in the presence of KH waves in the equatorial plane (the $X_{gse} - Y_{gse}$ plane), for the scenario in Figure 6.4.1. Figure of KH waves in the equatorial plane is from the simulation where its X_{sim}, Y_{sim} axes are shown as purple vectors. The X-Y plane of the simulation is in the same plane as $X_{gse} - Y_{gse}$. Time labels t_1 to t_4 correspond to those in Figures 6.4.1 and 6.4.2 where the MMS is crossing the wave trailing edge. Thick solid lines represent magnetic fields threading through the KH waves in the magnetosphere (blue) and magnetosheath (red). The parallel-streaming magnetospheric electrons (thick green arrow) are detected in the magnetosheath side around t_4, seen as the extended parallel ePAD in panel (e) of Figure 6.4.1, signalling the mid-latitude reconnection (green circle) happening in the southern hemisphere.

Panel (m) of Figure 6.4.1 shows magnetic curvature components in the LMN coordinates. The components C_m (red) and C_n (green) show some variations particularly around the local reconnection exhaust (around t_2). The curvature magnitude (black) is strongest at t_3 with the main contributors being C_m and C_n. The dominant negative curvature component C_m at t_3 corresponds to the ion jet with $\Delta V_m < 0$ at t_2 with ~ 1 s delay, consistent with *Runov et al.* [2003]. The component C_l shows some fluctuations, despite being small, along with other components during the parallel ePAD interval with ~ 2 s delay after the beginning of the parallel ePAD interval at t_3. This indicates that there may be some association between the mid-latitude reconnection and the magnetic curvature.

Panel (n) of Figure 6.4.1 shows a projection of the magnetic curvature on

the $M - N$ plane (roughly the equatorial plane) with the normalisation: $(\mathbf{C}_p = C_m\mathbf{m} + C_n\mathbf{n})/\sqrt{C_m^2 + C_n^2}$. In the reconnection exhaust (between t_2 and t_4), the magnetic curvature projection mostly points in the $-\mathbf{m}$ direction (red-purple vectors), consistent with the magnetic structure of the newly reconnected field line depicted in Figure 6.4.2. Note that at t_2 we observe a closed magnetic structure (orange circle in Figure 6.4.2). Panel (o) shows the radius of curvature $R_c = 1/|\sqrt{\mathbf{C}}|$ which is particularly small around t_2 and t_3 when the spacecraft were in the vicinity of the closed magnetic structure and the electron boundary layer on the magnetosheath side, respectively. The minimum curvature radius between t_2 and t_4 is found to be $0.06\ R_E$ or 382 km ($6.8\ d_i$); this could be either the scale of the closed magnetic structure or the scale of the curved, reconnected field lines. The radius of curvature is increasing after t_3, possibly due to the field straightening away from the reconnection X-line (see Figure 6.4.2). Using the MCA technique, in this case, helps to reveal the local magnetic structure and complements interpretations of the particle pitch angle distribution. However, the curvature associated with the mid-latitude reconnection is rather weak. We discuss possible explanations of this result below.

A first explanation would be the scale size of the MMS tetrahedron compared to the scale of the magnetic structure of the remote reconnection. As reported in Chapter 4, the resolved magnetic curvature is dependent on the scale size of the tetrahedron. Considering that the remote reconnection happens in a large scale, one would need a scale of the tetrahedron formation big enough to cover the change of the magnetic topology. Another explanation would be that since the KH waves were still in their linear stage, the magnetic fields were not yet bent much by the instability. Four-spacecraft observations near the mid-latitudes would help to capture this phenomenon in-situ. Moreover, coordinated observations of four-spacecraft missions at mid-latitudes and low-latitudes would be a promising way to confirm this phenomenon for both particle and magnetic curvature signatures.

Electron vorticity in panel (p) of Figure 6.4.1 is quiet in the magnetospheric side but is more active in the boundary layer and magnetosheath side. This shows that electron flows in the magnetosheath are probably more turbulent and vortical. It is also possible that the fluctuations of electron vorticity on the magnetosheath side during the parallel ePAD interval is associated with the mid-latitude reconnection. The total electron vorticity (black) is high due to the components $\Omega_{e,m}$ (red) and $\Omega_{e,n}$ (green) with a maximum value at t_4. This strong vorticity is consistent with the predicted vorticity near a (local) reconnection X-line [*Matthaeus*, 1982; *Matthaeus and Lamkin*, 1986]. Electron vorticity was also found to be associated with a crossing of ion diffusion region [*Gurgiolo et al.*, 2011].

6.5 Flux Transfer Event during the KH activity

A classical FTE in satellite data is characterised by the passage of bipolar magnetic variation in the magnetopause normal direction (B_N). The variation begins with a positive pulse and follows by a negative pulse for an FTE in the northern hemisphere and the variation is reversed in the southern hemisphere [*Rijnbeek et al.*, 1984]. Both magnetospheric and magnetosheath particle populations were detected in an FTE [*Paschmann et al.*, 1982]. In particular, the total pressure, the sum of plasma and magnetic pressure, and the magnetic field strength are expected to be strongly enhanced [*Paschmann et al.*, 1982]. The enhanced total pressure can be as twice as large or more than the background total pressure. In addition, a velocity enhancement is unexpected as the FTE is carried through with the background flow; an internal vortical flow must be present for the flux tube to travel faster than the ambient flow [*Schindler*, 1979].

The bipolar variation of B_N of an FTE crossing can resemble a passage of a rolled-up KH vortex. However, an FTE passage can be easily distinguished because of the total pressure must reach a local maximum, while for a KH vortex passage the total pressure typically reaches a local minimum (as seen in Chapter 4). Also, an FTE signature would appear isolated or separated by long periods of quiet activity [*Russell et al.*, 1996], while the KH waves appear more or less periodically. We expect to see these characteristics for an FTE passage.

Figure 6.5.1 shows the context of an FTE, characterised by the criteria as mentioned earlier, which appears (purple vectors) in the middle of the interval between 20:00 UT and 20:15 UT. Panels (a) - (e) show magnetic fields, ion number density, ion temperature, ion bulk velocity, and ion pressure respectively. Panels (a) - (c) show approximately repeated pattern which resembles KH wave passages. We mark a few waveforms in between vertical dashed lines. Panel (a) shows a peak in magnetic field magnitude (black) and a strong B_y (green) bipolar variation at around 20:06:50 UT, marked by the purple vector. This magnetic field peak occurs in waveform 2 where the density shows a transition from the magnetosheath to the magnetospheric sides. Panel (e) shows a peak in total pressure (black) that colocates with the B_y bipolar variation that is consistent with an FTE passage.

Figure 6.5.2 shows the passage of the isolated FTE at MMS1 during 20:06:41 UT and 20:07:01 UT (top; panels (a - k)) and its zoom-in (bottom; panels (l - r)) during 20:06:46 UT and 20:06:56 UT. Ion inertial length, d_i, of the interval 20:06:46 - 20:06:56 UT is 123 ± 10 km. Panel (a) shows magnetic fields in the GSE coordinates which shows enhanced magnetic field strength B_t (black) and the northward component B_z (blue). A clear rotation of the magnetic field B_y (green) can be seen around 20:06:51.2 UT marked by the vertical black dashed line (t_c), regarded here as the FTE centre. The magnetic fields are also shown in the local boundary LMN coordinates derived from a magnetopause model [*Shue et al.*, 1997] in panel (l).

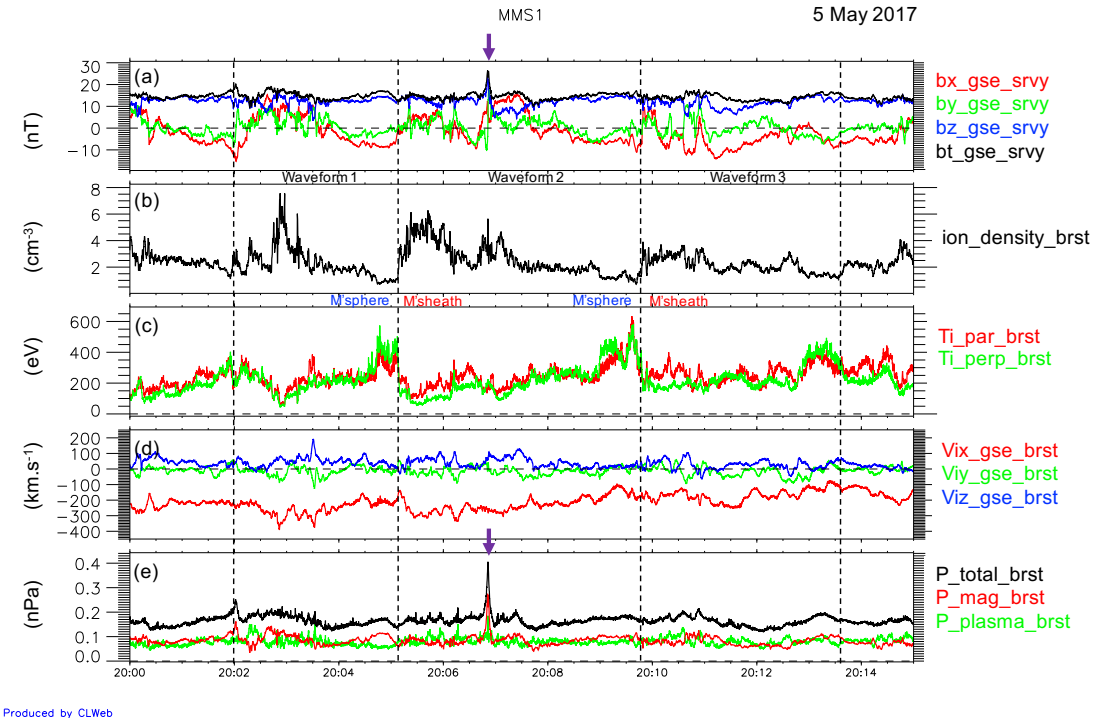

Figure 6.5.1: MMS1 observation of an FTE in the KH waves during 20:00 UT and 20:15 UT on 5 May 2017. (a) magnetic fields in GSE coordinates, (b) ion number density, (c) ion temperature, (d) ion bulk velocity in GSE coordinates, and (e) total pressure (black), magnetic pressure (red), and plasma pressure (green). Vertical dashed lines roughly mark transitions from the magnetospheric to magnetosheath sides. Purple vectors indicate the FTE passage.

In this LMN coordinates, **n** is perpendicular to the magnetopause boundary directed away from the Earth, **l** is directed along the Earth's geomagnetic north (for low-latitudes), and **m** completes the right-hand orthogonal system which points tail-ward for the dawn-side flank magnetopause. The bipolar variation of the magnetic field B_n in panel (l) (green) is consistent with characteristics of an FTE in the northern hemisphere, such that it begins with a positive pulse and then follows by a negative pulse [*Rijnbeek et al.*, 1984].

At the FTE centre t_c, ion number density shows a clear peak in panel (b), electron pitch angle distribution (ePAD) in middle energy range ($181 - 542$ eV) shows counter-streaming electrons in panel (c), and electron temperature shows strong parallel heating in panel (h). Around the FTE centre t_c, between t_1 and t_2 marked by vertical solid blue lines, total pressure shown as a black line in panel (g) is enhanced up to twice of the ambient total pressure ($\Delta P = 0.2$ nPa), consistent with *Paschmann et al.* [1982]. This TPE is dominated by the magnetic pressure (red), consistent with a flux-rope type plasmoid characteristics in *Ieda et al.* [1998]. The magnetic pressure enhancement drops to balance plasma pressure (green) at the FTE centre, t_c. Current density in panel (h) shows an increase in $J_z > 0$ (blue) surrounding the FTE centre. This positive J_z current sustain the magnetic field rotation B_y as seen in panel (a). The current density is also shown in the

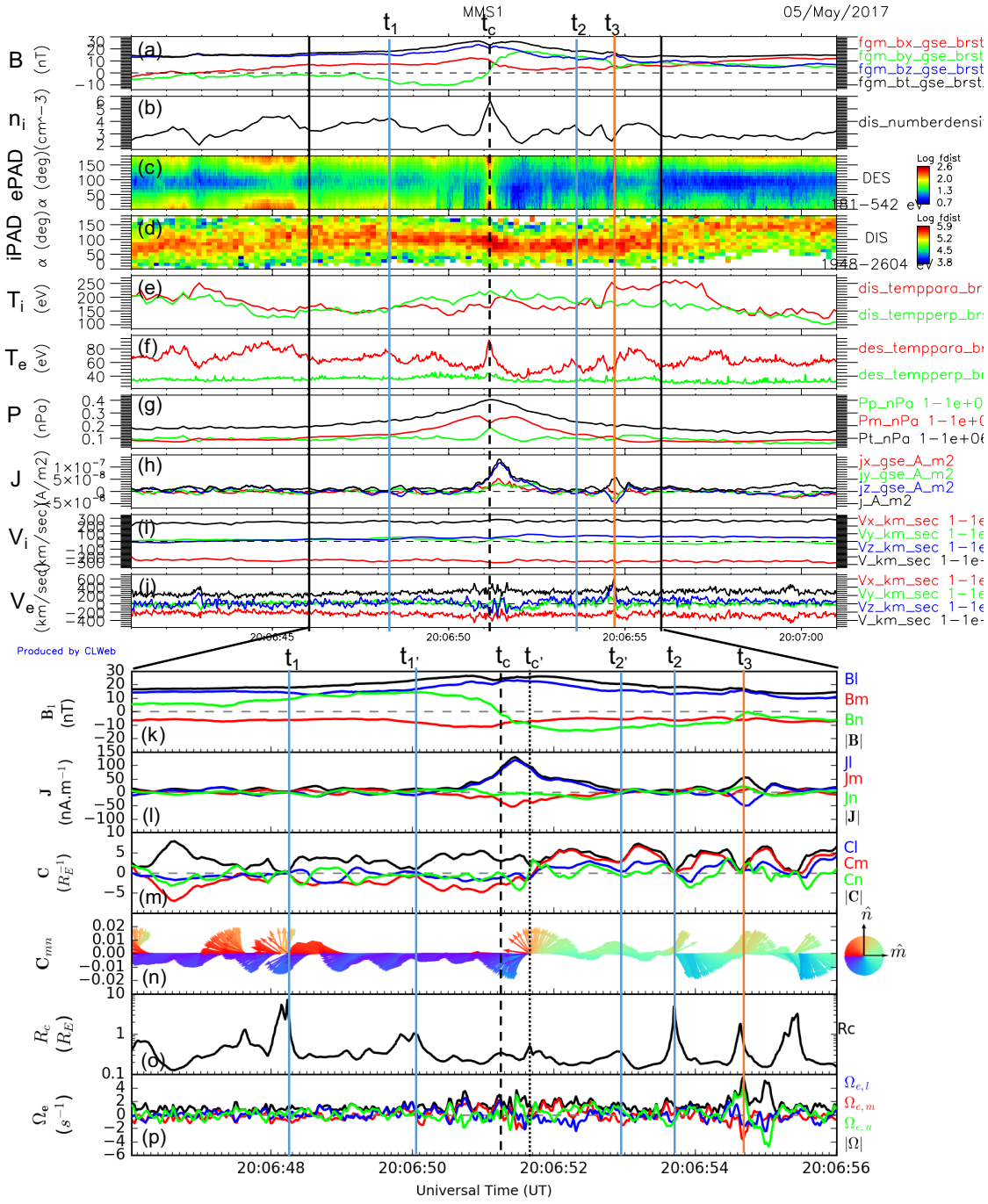

Figure 6.5.2: (top) Overview of the FTE crossing on 5 May 2017 during 20:06:41 and 20:07:01 UT in GSE coordinates: (a) magnetic fields; (b) ion number density; (c and d) ion and electron pitch angle distribution (iPAD and ePAD) for ion energy range $1.9 - 2.6$ keV and electron energy range $181 - 542$ eV; (e and f) parallel (red) and perpendicular (green) ion and electron temperatures; (g) total (black), magnetic (red), and plasma (green) pressures; (h) current density; and (i and j) ion and electron bulk velocity. (bottom) A zoom-in of the top panels during 20:06:46 UT and 20:06:56 UT in the local boundary LMN coordinates: (k) magnetic fields; (l) current density; (m) curvature vector components; (n) 2-D normalised curvature projection in the $M - N$ plane; (o) radius of curvature; and (p) electron vorticity.

LMN coordinates in panel (l) which shows strong positive J_l (blue) around the FTE centre. There is no distinct variation in ion bulk velocity as shown in panel (i), indicating that the FTE moves with the ambient flow speed as expected. Electron bulk velocity, in contrast, shows some fluctuation around the FTE centre t_c as seen in panel (j).

Panels (m) - (o) shows detailed magnetic curvature analyses in the LMN coordinates for the interval bounded by the two black solid lines in Figure 6.5.2 (top). Panel (m) shows magnetic curvature components; the component C_m (red) is dominant, indicating that the magnetic fields are mainly curved in **m** direction (sunward, tail-ward direction). A vertical black dotted line marked as $t_{c'}$ delineates a transition from $C_m < 0$ (sunward) to $C_m > 0$ (tail-ward) which is near to the FTE centre (t_c). Panel (n) shows a time series of the 2D normalised curvature vector which indicates magnetic tension force of the local magnetic field in the M-N plane (akin to the equatorial plane). The curvature vector direction is given by the curvature components in panel (m), e.g., pointing upward ($+$**n**) for $C_n > 0$ and to the right-hand side ($+$**m**) for $C_m > 0$. One can see a clear turning of the curvature direction from $-$**m** (sunward) to $+$**m** (tail-ward) at $t_{c'}$, called here as the FTE core. The radius of curvature (R_c) in panel (o) typically reaches a local maximum when $|\mathbf{C}|$ tends to 0, meaning that the magnetic field has no curvature and is therefore straight, e.g., at t_1 and t_2 (blue vertical lines). Average R_c around the FTE core, during 20:06:49 UT and 20:06:53 UT, is $\langle R_c \rangle = 2102 \pm 1147$ km, which is $\sim 15.3 d_i$ (ion inertial length). The minimum R_c in the interval surrounding the FTE core (between 20:06:50 and 20:06:53 UT) is $0.17\ R_E$ or 1078 km. This latter value may be related to the boundary of the flux-rope-type plasmoid. The diameter of the flux rope is therefore deduced to be 2158 km, which is $17.6\ d_i$. This is within the extent of the FTE crossing estimated using ion bulk speed during 20:06:46 UT and 20:06:56 UT which is ~ 2500 km. R_c at the FTE core is $1.04\ R_E$ which is larger than the surrounding. After $t_{c'}$, one can see that the R_c is decreasing away from the FTE core. This is consistent with a classical FTE model, e.g., as shown in Figure 6.5.4. Indeed, the resolved curvature is directly related through the 3-D structure of the FTE. We sketch a cross-section of this FTE structure with a possible spacecraft trajectory using this curvature information in Figure 6.5.3.

Outside of the FTE proper in the following period, at t_3 (orange vertical line) in Figure 6.5.2, one can notice a different structure from the FTE. This structure is characterised by a southward current density pulse, $\Delta J_l < 0$ (blue) in panel (l), which is reversed to that of the FTE. In panel (o), the curvature radius shows a local maximum, behind the boundary of the flux-rope-type plasmoid at t_2. In particular, the electron vorticity in panel (p) shows high fluctuations around t_3. These features may be indicative of a turbulent property behind the FTE.

Figure 6.5.3 shows a schematic illustration of the FTE structure as resolved by

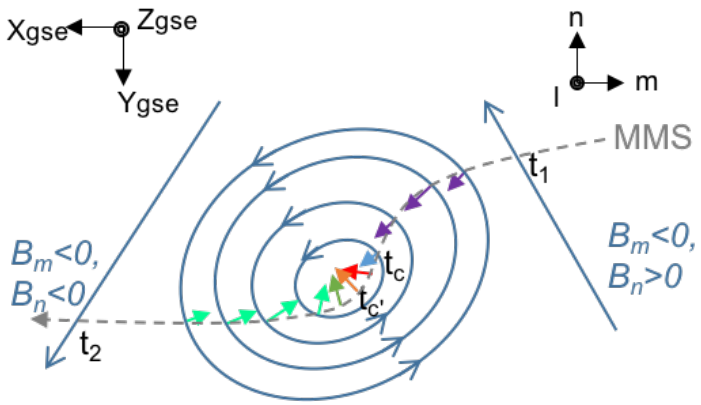

Figure 6.5.3: A schematic illustration of the FTE crossing depicted from Figure 6.5.2. Blue solid lines with unfilled arrows represent magnetic field lines and their directions, in which the blue loops represent the cross-section of the FTE. Times t_1, t_c, $t_{c'}$, and t_2 correspond to vertical dashed lines in Figure 6.5.2 panels (k - p). Grey dashed line shows a possible MMS trajectory which moves from t_1 to t_2 across the FTE. Filled arrows indicate curvature directions with the corresponding colours as shown in panel (n) of Figure 6.5.2.

the MCA tool. The spacecraft trajectory is represented by a grey dashed line. As MMS1 moves from t_1 to t_2, the magnetic curvature, represented by filled arrows, changes from sunward (purple) to tail-ward (mint-green), as resolved in panel (n) of Figure 6.5.2. These curvature directions indicate that the magnetic field curves towards the FTE core, consistent with a cross-section of the flux rope model [e.g., *Elphic and Russell*, 1983]. The magnetic field between t_1 and t_2 rotates in counter-clockwise direction as seen from above. We also show a schematic side-view ($L-M$ plane) of the FTE in Figure 6.5.4. The curvature radius, R_c, is higher at the FTE core than the periphery as resolved in panel (o) of Figure 6.5.2. Resolving the magnetic curvature in this case simultaneously gives an impression of the in-situ 3-D FTE structure without invoking data fitting into a flux-rope model. A more rigorous approach would be a real construction of the flux rope using the magnetic curvature components and the corresponding radius of curvature. This method would yield a result consistent with the multiple applications of the MVA technique to areas surrounding the FTE as done in *Hwang et al.* [2016]. There are other approaches that could be taken to fully understand this FTE event such as estimating flux content, e.g., using GS reconstruction, and determining the flux rope orientation. Nevertheless, our aim was to illustrate an application of the MCA tool. Those details are left for future studies as they are outside the scope of this study.

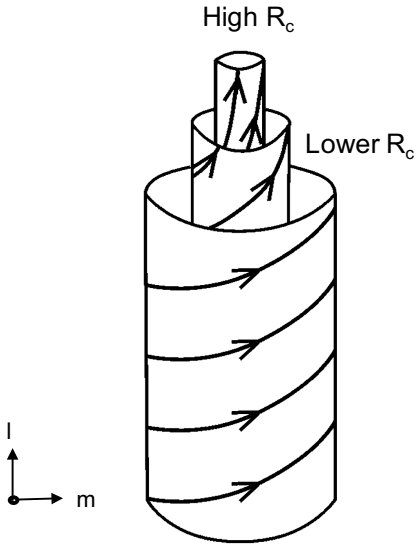

Figure 6.5.4: A cylindrical flux rope model, adapted from *Foullon et al.* [2007]. This illustration is a side view (the $L-M$ plane) of the FTE sketch in Figure 6.5.3. As seen in panel (o) of Figure 6.5.2, the radius of curvature (R_c) increases towards the core of the FTE while the magnetic curvature changes its direction (see panel (n)). Courtesy of *Bothmer and Schwenn* [1998].

6.6 Magnetic island in the KH wave trailing edge

In the same event as reported in Section 6.5, we choose a magnetopause crossing at a KH wave trailing edge that exhibits characteristics of a reconnection exhaust with an adjacent closed magnetic structure, similar to Section 6.4. It will be shown that this closed structure has characteristics consistent with a magnetic-island-type plasmoid. Magnetic islands are believed to be generated by the linear tearing mode instability [e.g, *Drake et al.*, 2006; *Cazzola et al.*, 2015]. Kinetic simulations show that the magnetic islands can be generated due to the electron KH instability induced by the differential flow in a reconnection exhaust [e.g, *Fermo et al.*, 2012; *Huang et al.*, 2015]. Magnetic islands were predicted to develop on the periphery of KH waves using 2-D kinetic simulations by *Nakamura et al.* [2011]. These magnetic islands were generated by vortex-induced-reconnection (VIR) at multiple locations in the compressed current sheets between two KH vortices. In particular, they were suggested to enhance plasma mixing while being incorporated into the KH vortices.

There are limited observational studies of magnetic islands in the magnetospheric environments. *Eriksson et al.* [2009] first identified magnetic islands in KH waves using THEMIS observations. Properties of these islands were studied using GS reconstruction [*Sonnerup et al.*, 2006; *Hasegawa et al.*, 2007] and MHD reconstruction [*Sonnerup and Teh*, 2008]. *Wang et al.* [2010a] reported first direct evidence of a magnetic island near the centre of an ion diffusion region of the reconnection site in the magnetotail using Cluster. A strong core magnetic field and

enhanced energetic electron fluxes were found inside the magnetic island [*Wang et al.*, 2010a, b]. *Vines et al.* [2017] first systematically studied the occurrence frequency and locations of magnetic islands at the dayside magnetopause using over 9 years of data of Cluster crossings near reconnection sites. However, high-resolution observations of magnetic islands in KH waves using MMS have not yet been reported.

Vines et al. [2017] characterised magnetic islands using counter-streaming electrons in the magnetosheath boundary layer. In addition, they consider electron energies that are higher than average magnetosheath electron energies (above hundreds of eV up to a few keV). Though other signatures such as an increase in magnetic field strength, bipolar B_N [e.g., *Eriksson et al.*, 2009] and possibly B_M in the LMN system, were also used in the literature, counter-streaming electrons are a signature of the closed magnetic field lines that is not affected by the spacecraft trajectory [e.g., *Wang et al.*, 2010b; *Vines et al.*, 2017]. In this Section, we adopt the counter-streaming electrons and possibly the total pressure enhancement (TPE) as the signatures of magnetic islands.

Figure 6.6.1 shows the context of KH observations between 20:35 UT and 20:55 UT at MMS1. Panels (a) - (e) show magnetic fields, ion number density, ion temperature, ion bulk velocity, and ion pressure respectively. All panels show quasi-periodic variations with a periodicity of about 5 minutes in the first half until 20:45 UT and with a periodicity of about 2.5 minutes after that. The shorter periodicity after 20:45 UT may be caused by the increase in IMF clock angle from about -20^o to -3^o in the GSM system during 20 UT to 21 UT as seen in panel (a) of Figure 6.3.4. When the IMF clock angle tends towards zero in the GSM system, KH-unstable regions (where $\mathbf{k}\cdot\mathbf{B}$ minimises in the KHI onset condition, equation 1.1), on the dayside magnetopause, shift towards the equator with broadening KH-unstable strips on both magnetopause flanks [*Farrugia et al.*, 1998; *Foullon et al.*, 2008] (see Figure 1.3.2 in Chapter 1). It is expected that the KH wavelength and amplitude become larger after 20:45 UT, and while the MMS trajectory approaches the theoretical 'unperturbed' magnetopause (from the magnetospheric side), MMS encounters the wavefronts of larger KH wave amplitudes. We believe that until 20:45 UT, the apparent periodicity represents two waveforms (i.e., periods of 2.2 mins) while after 20:45 UT when MMS detects single waveforms of longer period (2.5 mins). At around 20:44:40 UT, panels (b) and (c) of Figure 6.6.1 show a sharp transition (purple vector) from the magnetospheric side (hot and tenuous) to the magnetosheath side (cold and dense), corresponding to a passage of a wave "trailing edge". Total pressure (black) in panel (e) typically shows local maxima at the wave trailing edges. Ion bulk velocity in panel (d) shows a peak in total velocity (black), mainly contributed by V_{iz} (blue) and V_{ix} (red), at 20:44:40 UT marked by a purple vector. The value of the ion bulk velocity peak is 410 km

s^{-1} while the average ion bulk velocities from 20:35 UT to 20:44:40 UT and from 20:44:44 UT to 20:55 UT are ~ 196 km s^{-1} and ~ 268 km s^{-1}, respectively. The change in ion bulk velocity at around 20:44:40 UT is therefore $|\Delta V| = 178$ km s^{-1} compared to the average background velocity. We choose to analyse this particular magnetopause crossing which possesses the ion jet.

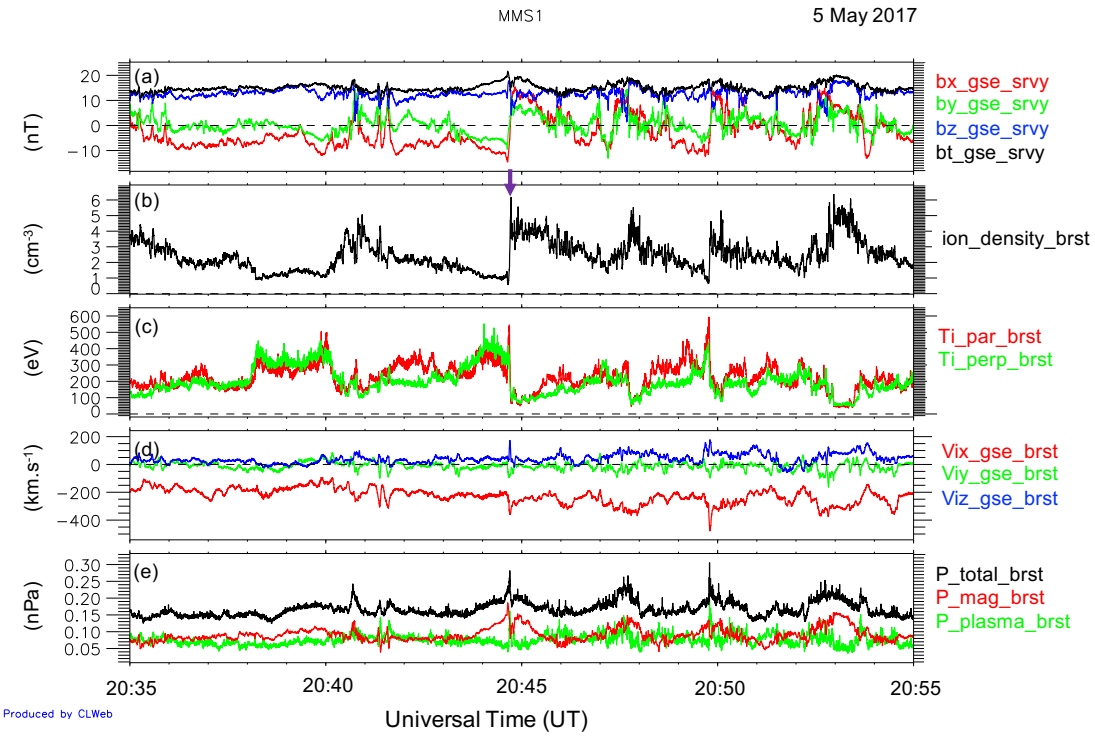

Figure 6.6.1: MMS1 observations during 20:35 UT and 20:55 UT on 5 May 2017. (a) magnetic fields in GSE coordinates, (b) ion number density, (c) ion temperature, (d) ion bulk velocity in GSE coordinates, and (e) total pressure (black), magnetic pressure (red), and plasma pressure (green). Purple vector points a passage of the wave trailing edge analysed in this Section.

Figure 6.6.2 shows MMS1 observations of the magnetopause crossing at the KH wave trailing edge between 20:44:20 UT and 20:45:00 UT in top panels (a-j). This is one of the clearest magnetopause crossings (see Figure 6.6.1). A zoom-in between 20:44:35 UT and 20:44:49 UT, marked by vertical black solid lines, are shown in bottom panels (k-p). MMS1 was in the magnetospheric side until 20:44:37.5 UT, marked as t_1, and entered the magnetosheath side from 20:44:44 UT, marked as t_2. The magnetospheric side has low ion number density ($n_1 = 1.0 \pm 0.1$ cm^{-3}) and high temperature ($T_1 = 479 \pm 50$ eV) as seen in panels (b) and (g), respectively. The magnetosheath side has higher ion number density ($n_2 = 4.1 \pm 0.5$ cm^{-3}) and lower temperature ($T_2 = 128 \pm 38$ eV). Average ion inertial length in the interval straddling the magnetopause boundary layer, between 20:44:35 and 20:44:49 UT, is $d_i = 137 \pm 41$ km. We mark the magnetospheric side, the magnetopause boundary layer (MPBL), and the magnetosheath sides as blue, purple, and red bars on top of Figure 6.6.2 respectively.

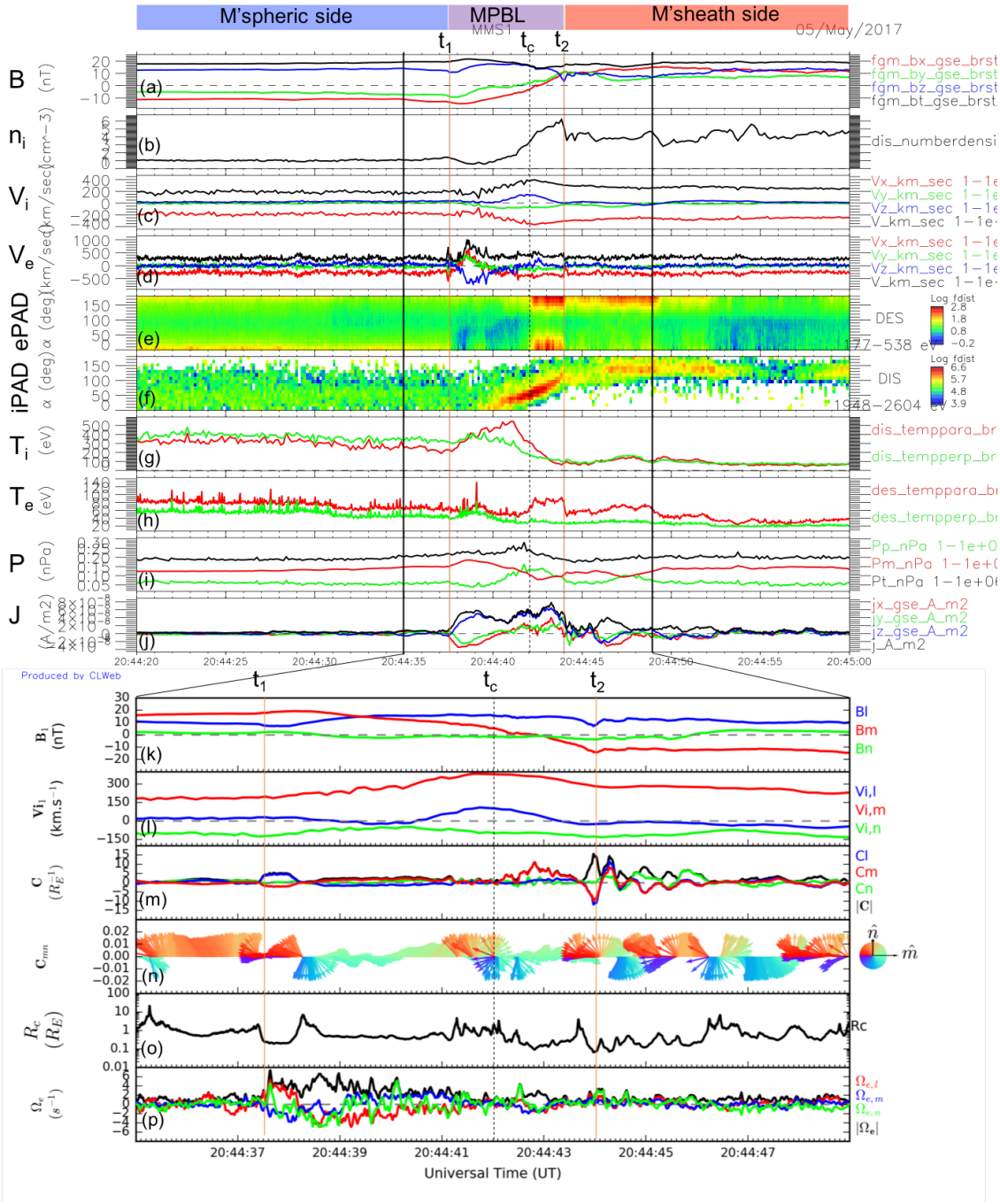

Figure 6.6.2: (top) Overview of a boundary layer crossing at the KH wave trailing edge during 20:44:20 UT and 20:45:00 UT on 5 May 2017 in GSE coordinates: (a) magnetic fields; (b) ion number density; (c and d) ion and electron bulk velocity; (e and f) electron and ion pitch angle distributions (ePAD and iPAD) in energy range $177 - 538$ eV and $1948 - 2604$ eV respectively; (g and h) ion and electron temperatures; (i) total pressure (black), magnetic pressure (red), and plasma pressure (green); (j) current density. (bottom) A zoom-in of the top panels during 20:44:35 UT and 20:44:49 UT in the local current sheet LMN coordinates: (k) magnetic fields; (l) ion bulk velocity; (m) curvature components; (n); 2-D normalised curvature projection in the $M - N$ plane; (o) radius of curvature; and (p) electron vorticity.

Panel (e) of Figure 6.6.2 shows electron pitch angle distribution (ePAD) for electron energy range $177 - 538$ eV. From left to right, one can see the bidirectional fluxes with peaks at 0^o and 180^o in the magnetospheric side, as expected for closed field lines of the magnetosphere. The ePAD then shows strong bidirectional fluxes or the counter-streaming electrons that are indicative of a closed magnetic structure in the MPBL. We will later discuss this feature. In the magnetosheath side, ePAD shows dominantly anti-parallel fluxes which correspond to Strahl population from the Sun similar to those identified in *Vernisse et al.* [2016]. However, the anti-parallel flux is particularly strong for about 5 seconds after t_2. In the same interval, panel (h) shows enhanced parallel electron heating. The strong anti-parallel ePAD in the magnetosheath BL may be consistent with reconnection in higher latitudes that causes the opened magnetic field lines in the northern hemisphere as previously identified in Section 6.4. We do not discuss this feature in this Section as our focus is on the counter-streaming electrons in the MPBL.

Panels (a) and (k) show magnetic fields in the GSE and the local boundary LMN coordinate systems, respectively. The LMN coordinate system is the same as the one in Section 6.4. The transformation is found to be $L = [0.131,\ 0.188,\ \ 0.973]$, $M = [-0.861, -0.466,\ 0.205]$, $N = [0.492, -0.865, 0.101]$ in the GSE coordinates. A magnetic field rotation can be seen in the components B_x (red) and B_y (green) in the MPBL. In the LMN coordinates, panel (k) shows a rotation of B_m (red) from 16.8 nT to -12.6 nT. The guide-field component B_l (blue) in panel (k) on both sides of the magnetopause are about the same, $B_l = 10.3$ nT, with an enhancement of about 3 nT in the MPBL. The magnetic shear angle is therefore 109^o. The current density in panel (j) is non-zero in the MPBL mainly due to the component $J_z > 0$ (blue) which supports the magnetic rotation. Panels (c) and (d) show ion and electron bulk velocities respectively. There is an ion jet in the MPBL, clearly seen in V_z (blue) and V_x (red) in the MPBL with a centre at 20:44:42, marked as t_c. The ion jet is better seen in the LMN coordinates in panel (l) where $\Delta V_{i,m} = +161$ km s^{-1} (red) and $\Delta V_{i,l} = +112$ km s^{-1} (blue). This ion jet occurs at the same time as the change of magnetic orientation in panel (a) and is therefore consistent with a reconnection jet. There is also an electron jet which precedes the ion jet seen just after t_1 (panel (d)).

In the MPBL, we observe a counter-streaming electron interval from t_c to t_2 in panel (e) that is indicative of a closed magnetic structure. This interval coincides with the strong parallel electron heating in panel (h). Panel (i) shows a TPE for about ~ 0.05 nPa between t_1 and t_2, covering the counter-streaming electron interval. This is consistent with a characteristic of a magnetic-island-type plasmoid [*Ieda et al.*, 1998] or a magnetic island identified in *Vines et al.* [2017]. However, the TPE does not exactly coincide with the interval of the counter-streaming elec-

trons. This TPE can be either from the compressed current sheet of the KH wave trailing edge (as previously seen in the MHD simulation in Chapter 4) or from the magnetic island itself. THEMIS observations showed that the TPE colocates with the bipolar B_n variation [*Eriksson et al.*, 2009]. Since the resolution of the THEMIS is not as high as MMS, it was not conclusive whether the TPE is purely due to the magnetic island. Kinetic simulation studies by *Nakamura et al.* [2011] found that clear pressure enhancement is not always present because reconnection tends to relax the TPE. Nevertheless, the plasma pressure during the counter-streaming electron is clearly dominant, in contrast to the interval that surrounds them. In addition, the total current density appears to be enhanced in this particular interval. We therefore conclude that it is a magnetic island in the MPBL and might be produced from the reconnection.

Panel (m) of Figure 6.6.2 shows magnetic curvature components which show a peak in $C_m > 0$ (red) at 20:44:42.8 UT after t_c. The curvature projections $\mathbf{C}_{mn}$ in panel (n) for this interval show that they mainly direct tailward (mint-green vectors). The curvature radius (panel (o)) at the highest curvature, which may be regarded as the radius of the magnetic island, is found to be $0.09\ R_E$ or 578 km. Its diameter is therefore 1156 km or $8.4\ d_i$. Magnetic curvature (panel (m)) in the magnetosheath side appears less ordered compared to the magnetospheric side, consistent with the turbulent nature of the magnetosheath flow. In addition, there is a peak of electron vorticity between t_c and t_2 in panel (p) of Figure 6.6.2 with $|\mathbf{\Omega}_e|_{max} = 4.5\ \mathrm{s}^{-1}$. This vorticity peak may be indicative of a vortical structure of the magnetic island. The electron vorticity peak in the vicinity of the magnetic island may be consistent with the electron vortices that are developed in a reconnection exhaust due to the differential flow, as predicted by *Fermo et al.* [2012]. Note that the high electron vorticity before t_c corresponds to the electron jet (panel (d)) that precedes the ion jet and it is a different flow structure.

Figure 6.6.3 shows a schematic illustration of the reconnection structure in the wave trailing edge. MMS 1 was in the magnetospheric side (blue) until around t_1 where $B_m > 0$ then exited to the magnetosheath side (red) from around t_2 where $B_m < 0$. In the MPBL, the positive ion jet $\Delta V_m > 0$ is shown as a filled green vector. Around this time, the magnetic island is observed between t_c and t_2, shown as an orange circle.

It is possible that the interval of counter-streaming electrons can be interpret as a Type-I VIR reconnecting current sheet with strong guide field, where the parallel and antiparallel electron flux can be due to the structure of the local parallel electric field. Similar observations were found in *Eriksson et al.* [2016] but not interpreted as an island. A counter argument for the vortical structure (the vorticity peak) of magnetic island would be a structure of the asymmetric reconnection. For this asymmetric reconnection, the exhaust is biased towards the magnetospheric side

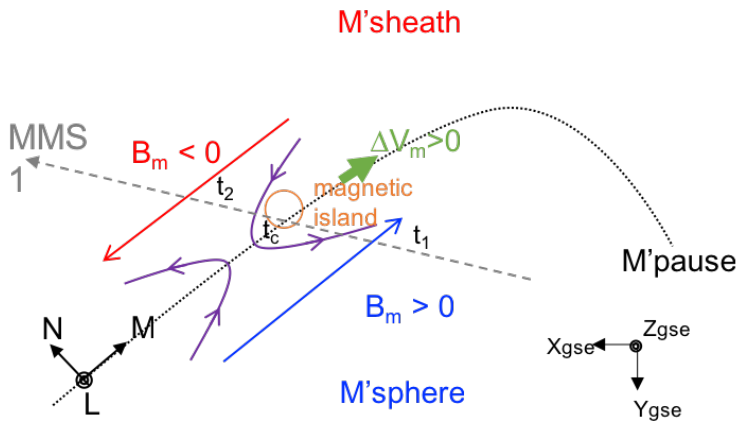

Figure 6.6.3: A schematic illustration of a crossing of the reconnection exhaust in Figure 6.6.2. Solid lines with unfilled arrows represent magnetic field lines. Times t_1, t_p, and t_2 correspond to vertical lines in Figure 6.6.2. Gray dashed line represents a likely spacecraft path explained as the following. The spacecraft first detects a fairly straight field line of $B_m > 0$ at t_1 on the magnetospheric side and later exits to the magnetosheath side where it detects another straight field line of $B_m < 0$ at t_2. In the boundary, the spacecraft detects a reconnection jet with $\Delta V_m > 0$ (big green filled arrow). At t_p, strong bidirectional ePAD fluxes are detected as seen in panel (e) of Figure 6.6.2. This population is depicted as a trapped electron population which comes from the two sides of the boundary that later becomes trapped in the magnetic island (purple circle).

of the current sheet. This explains why the large vorticity in this case is observed before 20:44:43 UT. The large vorticity between t_c and 20:44:43 is observed where the ion flow is still large and is not very different from that observed before t_c. Also, if it was an island, there should be high vorticity everywhere within the island (between t_c and t_2) and not only before 20:44:43 UT.

We did not discuss some of the features in Figure 6.6.2, as they are beyond the scope of this study. For example, we did not discuss the oscillatory magnetic curvature in panel (m) just after t_2 in the magnetosheath side in details. This feature may be associated with complex guide-field reconnection during KH activity, e.g., as those studied by *Sturner et al.* [2018]. However, further investigations are needed and they are left for future studies. In the future, we aim to characterise more magnetic islands in KH observations and investigate their properties.

6.7 Discussions and Conclusions

MMS provides unprecedented high spatiotemporal resolution observations suitable to study small-scale structures. We have applied the MCA and vorticity analysis techniques onto small-scale structures in KH waves observed on 8 September 2015 on the dayside dusk-flank magnetopause and 5 May 2017 on the post-terminator dawn-flank magnetopause. This Chapter provides examples of the

detailed analyses of the complex, small-scale structures in KH waves by utilising four-spacecraft tools to support particle signature interpretations. We conclude the analysis results of the chosen structures as follows.

In Section 6.4, we revisited the mid-latitude reconnection reported by *Vernisse et al.* [2016], adjacent to the local reconnection exhaust in the MPBL [*Eriksson et al.*, 2016], based on the remote particle signature in the magnetosheath boundary layer. The MCA technique reveals some fluctuations in all three curvature components, with 1 s delay, for the interval of the anti-parallel streaming electrons coming from the northern hemisphere, supposedly due to the mid-latitude reconnection that is induced by the KH waves. However, the fluctuations in magnetic curvature were found to be small. In this case, we suspect that the tetrahedron size has to be large enough to cover the scale size (as previously concluded in Chapter 4) of the mid-latitude reconnection or the spacecraft has to be near the reconnection site. Nevertheless, the MCA technique yields details of the local reconnection structure (with a closed magnetic structure) that are useful to understand the reconnection geometry.

In Section 6.5, we chose to analyse an FTE structure, characterised by the bipolar B_N variation and the TPE, that appears in a KH waveform. The TPE of the FTE is mainly contributed by the magnetic pressure, consistent with a flux-rope-type plasmoid. The detailed MCA analyses show the FTE structure such that the magnetic curvature curves inward while the curvature radius is increasing toward the FTE core, consistent with a classical cylindrical flux rope model. The cross-section scale size of the FTE is found to be $0.34\ R_E$ (2158 km), using the minimum curvature radius in the vicinity of the FTE core. This is within the dimension of the traverse size (2500 km) of the FTE using ion propagation velocity. The MCA analyses, in this case, readily give an impression of the in-situ structure. These show the advantage of the MCA technique over other methods that require certain assumptions such as data fitting into a flux rope model and the GS reconstruction.

In Section 6.6, we chose to analyse the magnetopause crossing at a KH wave trailing edge. This crossing was chosen because of its sharp magnetic rotation with the adjacent ion jet, consistent with a reconnection exhaust. Inside the reconnection exhaust in the MPBL, there is an interval of the counter-streaming electrons that are indicative of a closed magnetic structure. The counter-streaming electrons were found to co-locate with the plasma pressure enhancement, in spite of the absence of TPE. We interpreted this structure as a magnetic-island-type plasmoid, consistent with magnetic islands by VIR in KH wave trailing edges as predicted by *Nakamura et al.* [2011]. In particular, we found a peak in electron vorticity during the counter-streaming electron interval that indicates a vortical structure of the magnetic-island type plasmoid.

In Sections 6.4 and 6.6, the closed magnetic structures in the 8 September

2015 and 5 May 2017 events are found to be about the same size ($\sim 0.09\ R_E$) using the minimum curvature radius in the counter-streaming electron interval. Though TPE is not present in the first event, it is not clear in the second event either, consistent with properties of magnetic islands in KH waves in the kinetic simulations that do not exhibit TPEs [*Nakamura et al.*, 2011]. Nevertheless, the closed structure in the second event can be interpreted as a magnetic-island type plasmoid due to its dominant plasma pressure and enhanced total current density. We consider properties of the closed magnetic structures of both events, i.e., the closed structure in the second event has enhanced plasma pressure while that of the first event does not have it. Since KH waves in the first event were in the linear stage, while they are more developed in the second event, we may infer that the magnetic island with enhanced plasma pressure in the second event is in a more evolved stage than in the first event. In addition, for the 5 May 2017 event, we notice that both the FTE (Section 6.5) and the magnetic island (Section 6.6) have enhanced magnetic core fields (B_z). *Drake et al.* [2006] pointed out that the common presence of enhanced core fields in FTEs and magnetic islands are suggestive of FTE formation due to magnetic islands. However, more investigations are needed to conclude if they are related. In the future, we aim to analyse more magnetic islands in KH events with MMS as they appear to be common in reconnection exhausts near the wave trailing edges.

There are other things that could be done but are outside the scope of this study such as deriving other qualitative quantities of the FTE. Cross-scale, simultaneous observations, e.g., a co-formation of Cluster and MMS tetrahedrons in different scales, of KH waves would be desirable in the future as KH waves consist of multi-scale structures that involve physical mechanisms in large and small scales. This Chapter has provided structural analyses of small-scale phenomena of the KH waves complementing to Cluster observations in Chapter 5, which contribute to an overall understanding of KH mechanisms at the Earth's magnetopause.

Part IV

Conclusions

Chapter 7

Summary and Conclusions

We investigate, develop, and perform structural analyses of magnetopause KH waves using four-spacecraft. The aim is to understand applications of four-spacecraft techniques and to explore structures of the waves in multiple scales as introduced in Chapter 1. In Chapter 2, we describe the numerical MHD codes that are used to simulate magnetopause KH waves in this study. Considering curved magnetic structures and vortical flows induced by the waves, we choose the MCA and vorticity analysis techniques described in Chapter 3. Using virtual probes in MHD simulations in Chapter 4 allows us to investigate the robustness of the techniques and to interpret real observations. In particular, we consider virtual probes with varying tetrahedron sizes covering small to large scales. Cluster observations of a favourable KH event in Chapter 5 are used to validate the predicted qualitative signatures, such as the curvature direction and vorticity profile, and the idea of multi-scale applications in MHD scales. Finally, MMS observations of KH waves are presented in Chapter 6 to explore four-spacecraft applications in small scales. There, three small-scale structures, featuring (1) magnetic reconnection, (2) an FTE, and (3) a magnetic island, are presented. Summary of the work is as follows.

Four-spacecraft Applications to MHD Simulations

Chapter 4 presents four-spacecraft applications on a 2.5D MHD simulation of KH waves with typical conditions along the flank magnetopause on the dusk-side. The tetrahedron size, a, of the virtual probes is varied from $0.00625\lambda_{KH}$ to $0.3\lambda_{KH}$. A typical Cluster scale size is used to reproduced spatial (Section 4.4.1) and temporal (Section 4.4.2) profiles along the spacecraft trajectory traversing the waves. Magnetic curvature and flow vorticity at leading, inner, and trailing edges of a non-linear KH vortex are compared for the varying (regular) tetrahedron sizes in the spatial studies (Section 4.4.1). The radius of curvature is found to linearly increase with the tetrahedron size for the (middle) range $a/\lambda_{KH} \in [0.075, 0.25]$ while

it erratically varies with the tetrahedron size in the smaller and larger ranges. We attribute this complex dependence on the tetrahedron size to the non-linear spatial variations of the magnetic structure. KH vortex regions are further characterised using magnetic curvature in Section 4.4.1. The curvature radius is typically found to reach a minimum at the wave trailing edges; the curvature direction is found to rotate from sunward, earthward direction to against it at these locations. Evolution of the flow vorticity is investigated in Section 4.4.2. Negative vorticity is found to develop next to the positive vorticity of the vortex core in a rolled-up KH vortex and persists through the non-linear stage. This Chapter provides the expected KH signatures to be analysed in real data (e.g., with Cluster observations) and forms a basis for the understanding of the four-spacecraft measures in multi-scales of magnetopause KH waves.

Four-spacecraft Applications to Cluster Observations

Chapter 5 presents the four-spacecraft applications on 20 - 21 November 2001 KH event observed by Cluster inside the electron boundary layer on the dusk-side magnetopause. The interval of rolled-up KH waves reported in the literature allows us to validate the rolled-up vortex signatures as resolved in the simulation such as the curvature direction and vorticity profile. Moreover, the five 2-hour intervals of different IMF clock angles characterised by *Foullon et al.* [2008] allow us to compare four-spacecraft outputs in five different scales of KH waves with a relatively constant Cluster tetrahedron size. In Section 5.3.1, the predicted magnetic curvature signatures at the wave trailing edges are confirmed. In Section 5.3.2, the flow vorticity profile of rolled-up KH waves, a negative vorticity layer in between positive vorticity of the vortex core and the shear layer, is confirmed. The magnetic curvature is additionally found to point against the vortical flow at the vortex centre. We further characterise the curvature radius and vorticity extrema with the solar wind conditions in Section 5.3.3. The minimum curvature radius is found to linearly increase with the IMF clock angle while the maximum vorticity is found to decrease with the IMF clock angle linearly. The strength of the negative vorticity is found to linearly increase with the solar wind proton density and proton bulk speed. We further compare the minimum curvature radius for different ratios of the tetrahedron size to the KH wavelength, a/λ_{KH}, of the five intervals. The minimum curvature radius measurement is found to increase with the ratios, consistent with the simulation fit of the linear dependence in the middle range, $a/\lambda_{KH} \in [0.05, 0.025]$, (at the wave trailing edge) found in Chapter 4. We conclude three effects in the parametric survey (Section 5.3.3) that cause the linear relationships to be (1) the scale size of the KH waves and (2) the physical parameters that control excitations of the waves (e.g., density and velocity jumps), and

cause the lack of linear relationship to be (3) the non-linear KH evolution. Observational results in this Chapter have provided a validation of the four-spacecraft techniques to characterise in-situ KH waves, as initially revealed in the simulation. This work provides observational evidence of the multi-scale four-spacecraft measures that are consistent with the predicted non-linear spatial variations of the magnetic structures.

Four-spacecraft Applications to MMS Observations

Chapter 6 presents the four-spacecraft applications on small-scale structures in KH waves observed by MMS. MMS observations of KH waves provide high-resolution data in which fine scale structures of the waves can be resolved. In Section 6.4, we revisit a KH event on 8 September 2015 that was reported for local and mid-latitude magnetic reconnection at the trailing edges of the waves. Magnetic structures near the reported mid-latitude reconnection are analysed using the MCA to find, if any, related signatures. The associated magnetic curvature component is found to be relatively small for the interval of the mid-latitude reconnection. We conclude the weak correlation to be due to the scale size of the MMS being too small compared to the scale size of the process. An isolated FTE and a closed magnetic structure during the KH activity on 5 May 2017 are chosen for detailed four-spacecraft analyses. We analyse the FTE in the KH waveform using the MCA in Section 6.5. The in-situ magnetic curvature directions and radii near the FTE core are found to be consistent with a cylindrical flux rope model. In Section 6.6, we choose a sharp wave trailing edge with an ion jet and the adjacent interval of counter-streaming electrons indicative of a closed magnetic structure. We identify this closed structure as a magnetic-island-type plasmoid. The structure may be interpreted as the predicted magnetic islands developed in wave trailing edges which could enhance plasma mixing. The vorticity peak in electron vorticity is found and interpreted as a vortical structure of the plasmoid. The minimum curvature radii are obtained for all of the structures and used to estimate their scale sizes. Results in this Chapter provide examples of small-scale structural analyses with MMS observations and are helpful for interpretations of particle signatures.

Combining simulation, Cluster, and MMS results

We have analysed the structures of the magnetopause KH waves using the four-spacecraft tools with varying tetrahedron sizes in the simulation. The analyses result in the dependence of the MCA measures on the a/λ_{KH} ratio that can be understood in three scale ranges (e.g., (1) small, $a/\lambda_{KH} < 0.075$; (2) medium,

$a/\lambda_{KH} \in [0.075, 0.25]$; and (3) large, $a/\lambda_{KH} > 0.25$). The Cluster observations of a special KH event allow us to validate the dependence on the a/λ_{KH} ratio in the medium range, though other effects that can be linked to KHI excitation and non-linear evolution were also identified. Looking for confirmation of the a/λ_{KH} dependence in other scale ranges, we may consider the MMS observations on 8 September 2015 detected on the dayside, dusk-flank magnetopause which is almost the same configuration as in the simulation. Considering the interval of the trailing edge crossing, we obtain the a/λ_{KH} ratio to be 0.01 using the KH wavelength reported in the literature [*Eriksson et al.*, 2016]. We may use the minimum curvature radius during this interval to represent the $R_{c,min}/\lambda_{KH}$ ratio in the small range. Figure 7.0.1 shows the $R_{c,min}/\lambda_{KH}$ versus the a/λ_{KH} ratios from the simulation (dashed line) and Cluster observations (coloured symbols) in the medium range and MMS observations (purple star) in the small range. Despite the different solar-wind conditions, this plot illustrates the non-linear spatial variations of the KH structures in small and medium scale ranges. This result has a useful implication for interpretations of structural analyses of in-situ observations from a future cross-scale mission.

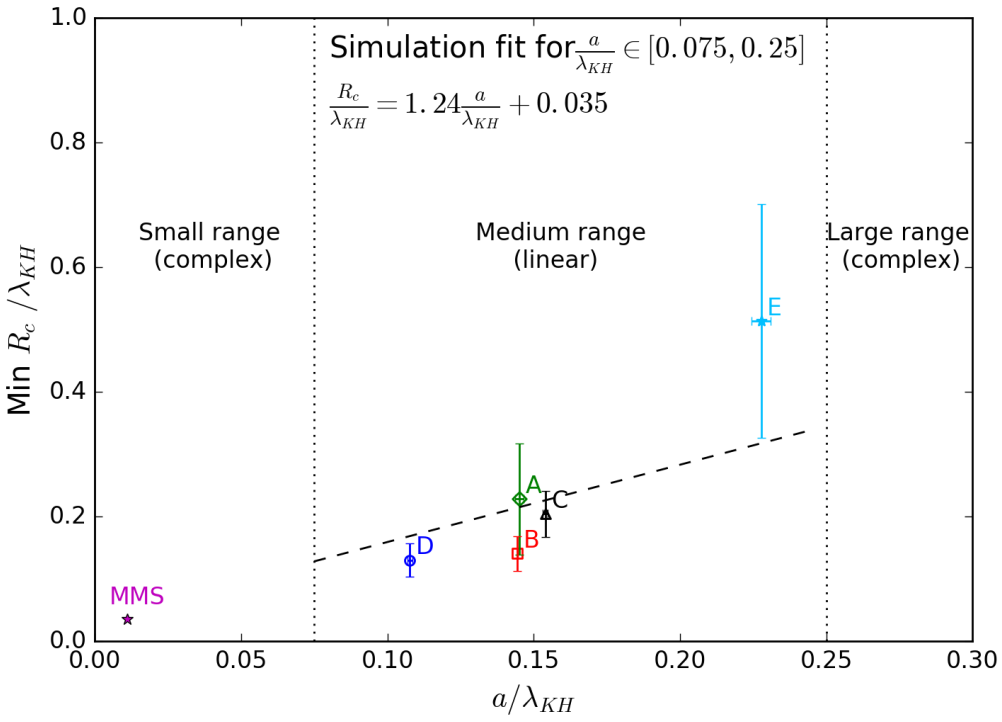

Figure 7.0.1: Plot of the $R_{c,min}/\lambda_{KH}$ versus the a/λ_{KH} ratios, shown for the small and medium ranges where the observational data is available, to illustrate the non-linear spatial variations of the magnetopause KH wave structures. The dashed line represents the simulation fit in the medium range (panel (c) of Figure 4.4.3). The coloured symbols in the medium range represent data from Cluster (panel (b) of Figure 5.4.1). The purple star in the small range represents data from MMS (panel (o) of Figure 6.4.1).

Applications of this thesis are not limited to magnetopause KH waves, but are available to any four-spacecraft observations of curved magnetic and vortical flow structures in the Earth's magnetospheric environments. Simultaneous, multi-scale observations have been attempted at the time of writing by a synergy between Cluster and MMS [e.g., *Escoubet et al.*, 2015]. The multi-scale four-spacecraft structural analyses in this thesis would be helpful to understand spatial variations of plasma structures in such observations as they are proved to provide new insights complementary to particle signatures in MHD and kinetic scales.

Future Works and Outlook

The four-spacecraft tools are shown to provide detailed structures of the magnetopause plasmas. We can use such details, e.g., magnetic curvature radii and directions, to construct an in-situ structure without any prior assumptions about the structure, unlike other single and multi-spacecraft techniques such as model fitting and Grad-Shafranov reconstruction. We aim to construct a magnetic structure such as an FTE using the MCA outputs in future observations.

In the KH events observed by MMS, magnetic-island-type plasmoids seem to be common in the wave trailing edges. We aim to characterise more magnetic islands and statistically study their properties in the future to understand their roles in the solar-wind mixing mediated by KH waves.

Provided availability of future missions or serendipitous cases of the current missions, such that small and large tetrahedron scales simultaneously observe a KH event with the same barycentre, we would aim to resolve variations of the plasma structures in multi-scales to understand the cross-scale coupling of the KH mechanism at the Earth's magnetopause.

Appendix

A Minimum Variance Analysis

Minimum Variance Analysis (MVA) [*Sonnerup and Scheible*, 1998] is a single-spacecraft method for finding the normal direction of a 1-D structure based on magnetic field data. Since the solenoidal condition of magnetic fields is always enforced, $\nabla \cdot \mathbf{B} = 0$, the normal direction is found from $\mathbf{B} \cdot \mathbf{n} = 0$. Given a magnetic field data set, $\{\mathbf{B}^{(m)} \cdot \mathbf{n}\}, (m = 1, 2, ..., M)$, must be zero in an ideal case. Since in real situation there may be noise or any non-systematic errors that can deviate the result, we aim to minimise $\{\mathbf{B}^{(m)} \cdot \mathbf{n}\}$ as much as possible.

The normal direction can be estimated from the minimisation of the variance

$$\sigma^2 = \frac{1}{M} \sum_{m=1}^{M} |(\mathbf{B}^{(m)} - \langle \mathbf{B} \rangle) \cdot \mathbf{n}|^2 \tag{7.1}$$

where the average $\langle \mathbf{B} \rangle$ is defined by

$$\langle \mathbf{B} \rangle \equiv \frac{1}{M} \sum_{m=1}^{M} \mathbf{B}^{(m)}. \tag{7.2}$$

With the normalisation constraint $|\mathbf{n}|^2 = 1$, we make use of a Lagrange multiplier λ. Then we seek the solution of three homogeneous linear equations

$$\frac{\partial}{\partial n_i} \left(\sigma^2 - \lambda(|\mathbf{n}|^2 - 1) \right) = 0, \quad i = x, y, z. \tag{7.3}$$

On differentiation, the resulting equations can be writtend in matrix form as

$$\sum_{\nu=1}^{3} M^B_{\mu\nu} n_\nu = \lambda n_\mu, \tag{7.4}$$

where $\mu, \nu = 1, 2, 3$ label Cartesian components along x, y, z system. The matrix variance is given by

$$M^B_{\mu\nu} \equiv \langle B_\mu B_\nu \rangle - \langle B_\mu \rangle \langle B_\nu \rangle. \tag{7.5}$$

It can be seen from equation 7.4 that allowed eigenvalues λ of $M^B_{\mu\nu}$ are $\lambda_1, \lambda_2, \lambda_3$ (given here from biggest to smallest ones), corresponding to eigenvectors $\mathbf{x}_1, \mathbf{x}_2, \mathbf{x}_3$.

The variance matrix $M^B_{\mu\nu}$ is symmetric ($M^B_{\mu\nu} = M^B_{\nu\mu}$). The eigenvalues $\lambda_1, \lambda_2, \lambda_3$ are all real. The eigenvectors $\mathbf{x}_1, \mathbf{x}_2, \mathbf{x}_3$ are orthogonal, corresponding to the directions of maximum, intermediate, and minimum variance of the field component along each vector. We look for the eigenvector $\mathbf{x}_3$ as the estimated normal direction, where the eigenvalue λ_3 is the minimum variance of the magnetic field component along $\mathbf{x}_3$.

The following aspects should be considered for good results,

- A value of λ_3 should be small compared to λ_1, λ_2 ,i.e., $\lambda_2/\lambda_3 \geq 10$ is a rule of thumb for a relatively small data set ($M \leq 50$).
- Nested sets of data intervals should be centred at or near the middle of the structure being measured.
- The discontinuity should be stationary. The stationary assumption can be tested by changing the nested data segments. Different nested segments should give the same result.

Bibliography

Adamson, E., K. Nykyri, and A. Otto, The Kelvin-Helmholtz instability under Parker-Spiral Interplanetary Magnetic Field conditions at the magnetospheric flanks, *Adv. Sp. Res.*, *58*, 218--230, doi:10.1016/j.asr.2015.09.013, 2016.

Arber, T. D., A. W. Longbottom, C. L. Gerrard, and A. M. Milne, A Staggered Grid, Lagrangian-Eulerian Remap Code for 3-D MHD Simulations, *J. Comput. Phys.*, *171*, 151--181, 2001.

Axford, W. I., Viscous interaction between the solar wind and the Earth's magnetosphere, *Planet. Space Sci.*, *12*, 45--53, doi:10.1016/0032-0633(64)90067-4, 1964.

Axford, W. I., and C. O. Hines, A unifying theory of high-latitude geophysical phenomena and geomagnetic storms, *Can. J. Phys.*, *39*, 1433, doi:10.1139/p61-172, 1961.

Bavassano Cattaneo, M. B., M. F. Marcucci, Y. V. Bogdanova, H. Rème, I. Dandouras, L. M. Kistler, and E. Lucek, Global reconnection topology as inferred from plasma observations inside Kelvin-Helmholtz vortices, *Ann. Geophys.*, *28*(4), 893--906, doi:10.5194/angeo-28-893-2010, 2010.

Belmont, G., and G. Chanteur, Advances in magnetopause Kelvin-Helmholtz instability studies, *Phys. Scripta*, *40*(40), 124--128, 1989.

Berchem, J., and C. T. Russell, The thickness of the magnetopause current layer: ISEE 1 and 2 observations, *J. Geophys. Res.*, *87*, 2108--2114, doi:10.1029/JA087iA04p02108, 1982.

Borgogno, D., F. Califano, M. Faganello, and F. Pegoraro, Double-reconnected magnetic structures driven by Kelvin-Helmholtz vortices at the Earth's magnetosphere, *Phys. Plasmas*, *22*, 032301, doi:10.1063/1.4913578, 2015.

Borovikov, S. N., and N. V. Pogorelov, Voyager 1 near the Heliopause, *Astrophys. J.*, *783*, L16, doi:10.1088/2041-8205/783/1/L16, 2014.

Bothmer, V., and R. Schwenn, The structure and origin of magnetic clouds in the solar wind, *Ann. Geophys.*, *16*, 1--24, doi:10.1007/s00585-997-0001-x, 1998.

Burch, J., T. E. Moore, R. Torbert, and B. L. Giles, Magnetospheric Multiscale Overview and Science Objectives, *Sp. Sci. Rev.*, *199*, 5--21, doi:10.1007/s11214-015-0164-9, 2015.

Cahill, L. J., and P. G. Amazeen, The Boundary of the Geomagnetic Field, *J. Geophys. Res.*, *68*, 1835--1843, doi:10.1029/JZ068i007p01835, 1963.

Cao, D., et al., MMS observations of whistler waves in electron diffusion region, *Geophys. Res. Lett.*, *44*, 3954--3962, doi:10.1002/2017GL072703, 2017.

Cazzola, E., M. E. Innocenti, S. Markidis, M. V. Goldman, D. L. Newman, and G. Lapenta, On the electron dynamics during island coalescence in asymmetric magnetic reconnection, *Phys. Plasmas*, *22*, 092901, doi:10.1063/1.4929847, 2015.

Chandrasekhar, S., *Hydrodynamic and hydromagnetic stability*, Clarendon Press, 1961.

Chanteur, G., Spatial Interpolation for Four Spacecraft: Theory, *ISSI Sci. Reports Ser.*, *1*, 349--370, 1998.

Chanteur, G., and C. Harvey, Spatial Interpolation for Four Spacecraft: Application to Magnetic Gradients, *ISSI Sci. Reports Ser.*, *1*, 371--394, 1998.

Chapman, S., and V. C. A. Ferraro, A new theory of magnetic storms, *J. Geophys. Res.*, *36*, 77, doi:10.1029/TE036i002p00077, 1931.

Chaston, C. C., M. Wilber, F. S. Mozer, M. Fujimoto, M. L. Goldstein, M. Acuna, H. Reme, and A. Fazakerley, Mode conversion and anomalous transport in Kelvin-Helmholtz vortices and kinetic Alfvén waves at the earth's magnetopause, *Phys. Rev. Lett.*, *99*(17), 1--4, doi:10.1103/PhysRevLett.99.175004, 2007.

Chen, S.-H., M. G. Kivelson, J. T. Gosling, R. J. Walker, and A. J. Lazarus, Anomalous aspects of magnetosheath flow and of the shape and oscillations of the magnetopause during an interval of strongly northward interplanetary magnetic field, *J. Geophys. Res.*, *98*, 5727--5742, doi:10.1029/92JA02263, 1993.

Collado-Vega, Y. M., R. L. Kessel, D. G. Sibeck, V. L. Kalb, R. A. Boller, and L. Rastaetter, Comparison between vortices created and evolving during

fixed and dynamic solar wind conditions, *Ann. Geophys.*, *31*(8), 1463--1483, doi:10.5194/angeo-31-1463-2013, 2013.

Consolini, G., M. Materassi, M. Federica Marcucci, and G. Pallocchia, Statistics of the Velocity Gradient Tensor in Space Plasma Turbulent Flows, *Astrophys. J.*, *812*, 84, doi:10.1088/0004-637X/812/1/84, 2015.

Cowee, M. M., D. Winske, and S. P. Gary, Two-dimensional hybrid simulations of superdiffusion at the magnetopause driven by Kelvin-Helmholtz instability, *J. Geophys. Res.*, *114*(A10), 1--8, doi:10.1029/2009JA014222, 2009.

Cowee, M. M., D. Winske, and S. P. Gary, Hybrid simulations of plasma transport by Kelvin-Helmholtz instability at the magnetopause: Density variations and magnetic shear, *J. Geophys. Res.*, *115*, A06214, doi:10.1029/2009JA015011, 2010.

De Keyser, J., and M. Roth, Structural analysis of periodic surface waves on the magnetospheric boundary, *Planet. Space Sci.*, *51*(12), 757--768, doi:10.1016/S0032-0633(03)00112-0, 2003.

Denton, R. E., B. U. Ö. Sonnerup, J. Birn, W. L. Teh, J. F. Drake, M. Swisdak, M. Hesse, and W. Baumjohann, Test of methods to infer the magnetic reconnection geometry from spacecraft data, *J. Geophys. Res.*, *115*, A10242, doi:10.1029/2010JA015420, 2010.

Denton, R. E., B. U. Ö. Sonnerup, M. Swisdak, J. Birn, J. F. Drake, and M. Hesse, Test of Shi et al. method to infer the magnetic reconnection geometry from spacecraft data: MHD simulation with guide field and antiparallel kinetic simulation, *J. Geophys. Res.*, *117*, A09201, doi:10.1029/2012JA017877, 2012.

Drake, J. F., M. Swisdak, K. M. Schoeffler, B. N. Rogers, and S. Kobayashi, Formation of secondary islands during magnetic reconnection, *Geophys. Res. Lett.*, *33*(13), 10--13, doi:10.1029/2006GL025957, 2006.

Dungey, J. W., Interplanetary Magnetic Field and the Auroral Zones, *Phys. Rev. Lett.*, *6*, 47--48, doi:10.1103/PhysRevLett.6.47, 1961.

Dungey, J. W., The structure of the exosphere, or adventures in velocity space, *Geophysics, The Earth's Environment*, 1963.

Dungey, J. W., and D. J. Southwood, Ultra Low Frequency Waves in the Magnetosphere, *Space Sci. Rev.*, *10*, 672--688, doi:10.1007/BF00171551, 1970.

Dunlop, M., S. Haaland, C. Escoubet, and X. Dong, Commentary on accessing 3-D currents in space: Experiences from Cluster, *J. Geophys. Res.*, *121*, 7881--7886, doi:10.1002/2016JA023362, 2016.

Dunlop, M. W., and J. P. Eastwood, The Curlometer and Other Gradient Based Methods, *ISSI Sci. Reports Ser.*, *8*, 17--26, 2008.

Dunlop, M. W., and T. I. Woodward, Multi-Spacecraft Discontinuity Analysis: Orientation and Motion, *ISSI Sci. Reports Ser.*, *1*, 271--306, 1998.

Dunlop, M. W., D. J. Southwood, K. H. Glassmeier, and F. M. Neubauer, Analysis of multipoint magnetometer data, *Adv. Sp. Res.*, *8*(9-10), 273--277, doi:10.1016/0273-1177(88)90141-X, 1988.

Dunlop, M. W., A. Balogh, K. H. Glassmeier, and P. Robert, Four-point Cluster application of magnetic field analysis tools: The Curlometer, *J. Geophys. Res.*, *107*(A11), 1--14, doi:10.1029/2001JA005088, 2002.

Eastman, T. E., J. Hones, E. W., S. J. Bame, and J. R. Asbridge, The magnetospheric boundary layer: Site of plasma, momentum and energy transfer from the magnetosheath into the magnetosphere, *Geophys. Res. Lett.*, *3*, 685--688, doi:10.1029/GL003i011p00685, 1976.

Elphic, R., and C. Russell, Magnetic flux ropes in the Venus ionosphere - Observations and models, *J. Geophys. Res.*, *88*, 58--72, doi:10.1029/JA088iA01p00058, 1983.

Eriksson, S., et al., Magnetic island formation between large-scale flow vortices at an undulating postnoon magnetopause for northward interplanetary magnetic field, *J. Geophys. Res.*, *114*(A1), doi:10.1029/2008JA013505, 2009.

Eriksson, S., et al., Magnetospheric Multiscale Observations of the Electron Diffusion Region of Large Guide Field Magnetic Reconnection, *Phys. Rev. Lett.*, *117*(1), 015001, doi:10.1103/PhysRevLett.117.015001, 2016.

Eriksson, S., et al., Magnetospheric Multiscale observations of magnetic reconnection associated with Kelvin-Helmholtz waves, *Geophys. Res. Lett.*, *43*(11), 5606--5615, doi:10.1002/2016GL068783, 2016.

Escoubet, C., M. Fehringer, and M. Goldstein, Introduction The Cluster mission, *Ann. Geophys.*, *19*, 1197--1200, 2001.

Escoubet, C. P., A. Masson, H. Laakso, and M. L. Goldstein, Recent highlights from Cluster, the first 3-D magnetospheric mission, *Ann. Geophys.*, *33*, 1221--1235, doi:10.5194/angeo-33-1221-2015, 2015.

Evans, C. R., and J. F. Hawley, Simulation of Magnetohydrodynamic Flows: A Constrained Transport Model, *Astrophys. J.*, *332*, 659, doi:10.1086/166684, 1988.

Faganello, M., F. Califano, F. Pegoraro, and T. Andreussi, Double mid-latitude dynamical reconnection at the magnetopause: An efficient mechanism allowing solar wind to enter the Earth's magnetosphere, *Europhys. Lett.*, *100*(6), doi:10.1209/0295-5075/100/69001, 2012a.

Faganello, M., F. Califano, F. Pegoraro, T. Andreussi, and S. Benkadda, Magnetic reconnection and Kelvin-Helmholtz instabilities at the Earth's magnetopause, *Plasma Phys. Control. Fusion*, *54*(12), doi:10.1088/0741-3335/54/12/124037, 2012b.

Faganello, M., F. Califano, F. Pegoraro, and A. Retinò, Kelvin-Helmholtz vortices and double mid-latitude reconnection at the Earth's magnetopause: Comparison between observations and simulations, *Europhys. Lett.*, *107*, 19001, doi:10.1209/0295-5075/107/19001, 2014.

Fairfield, D. H., A. Otto, T. Mukai, S. Kokubun, R. P. Lepping, J. T. Steinberg, a. J. Lazarus, and T. Yamamoto, Geotail observations of the Kelvin-Helmholtz instability at the equatorial magnetotail boundary for parallel northward fields, *J. Geophys. Res.*, *105*(A9), 21,159--21,173, doi:10.1029/1999JA000316, 2000.

Farrugia, C. J., F. T. Gratton, L. Bender, H. K. Biernat, N. V. Erkaev, J. M. Quinn, R. B. Torbert, and V. Dennisenko, Charts of joint Kelvin-Helmholtz and Rayleigh-Taylor instabilites at the dayside magnetopause for strongly northward interplanetary magnetic field, *J. Geophys. Res.*, *103*(A4), 6703, doi:10.1029/97JA03248, 1998.

Farrugia, C. J., F. T. Gratton, G. Gnavi, R. B. Torbert, and L. B. Wilson, A vortical dawn flank boundary layer for near-radial IMF: Wind observations on 24 October 2001, *J. Geophys. Res.*, *119*(6), 4572--4590, doi:10.1002/2013JA019578, 2014.

Fermo, R., J. Drake, and M. Swisdak, Secondary Magnetic Islands Generated by the Kelvin-Helmholtz Instability in a Reconnecting Current Sheet, *Phys. Rev. Lett.*, *108*(25), 255,005, doi:10.1103/PhysRevLett.108.255005, 2012.

Forsyth, C., M. Lester, A. N. Fazakerley, C. J. Owen, and A. P. Walsh, On the effect of line current width and relative position on the multi-spacecraft curlometer technique, *Planet. Space Sci.*, *59*, 598--605, doi:10.1016/j.pss.2009.12.007, 2011.

Foullon, C., C. J. Owen, S. Dasso, L. M. Green, I. Dandouras, H. A. Elliott, A. N. Fazakerley, Y. V. Bogdanova, and N. U. Crooker, Multi-spacecraft study of the 21 January 2005 ICME : Evidence of current sheet substructure near the periphery of a strongly expanding, fast magnetic cloud, *Sol. Phys.*, *244*(1-2), 139--165, doi:10.1007/s11207-007-0355-y, 2007.

Foullon, C., C. Farrugia, A. Fazakerley, C. Owen, F. Gratton, and R. Torbert, Evolution of Kelvin-Helmholtz activity on the dusk flank magnetopause, *J. Geophys. Res.*, *113*, A11,203, doi:10.1029/2008JA013175, 2008.

Foullon, C., C. Farrugia, A. Fazakerley, C. Owen, F. Gratton, and R. Torbert, On the multispacecraft determination of periodic surface wave phase speeds and wavelengths, *J. Geophys. Res.*, *115*, 9203, doi:10.1029/2009JA015189, 2010.

Foullon, C., E. Verwichte, V. M. Nakariakov, K. Nykyri, and C. J. Farrugia, Magnetic Kelvin-Helmholtz instability at the sun, *Astrophys. J. Lett.*, *729*(1 PART II), 2--5, doi:10.1088/2041-8205/729/1/L8, 2011.

Frank, A., T. W. Jones, D. Ryu, and J. B. Gaalaas, The Magnetohydrodynamic Kelvin-Helmholtz Instability: A Two-dimensional Numerical Study, *Astrophys. J.*, *460*, 777, doi:10.1086/177009, 1996.

Fu, H. S., A. Vaivads, Y. V. Khotyaintsev, V. Olshevsky, M. André, J. B. Cao, S. Y. Huang, A. Retinò, and G. Lapenta, How to find magnetic nulls and reconstruct field topology with MMS data?, *J. Geophys. Res.*, *120*(5), 3758--3782, doi:10.1002/2015JA021082, 2015.

Fujimoto, M., and T. Terasawa, Ion inertia effect on the Kelvin-Helmholtz instability, *J. Geophys. Res.*, *96*(A9), 15,725--15,734, doi:10.1029/91JA01312, 1991.

Fujimoto, M., and T. Terasawa, Anomalous ion mixing within an MHD scale Kelvin-Helmholtz vortex, *J. Geophys. Res.*, *100*(A7), 12,025--12,033, doi:10.1029/93JA02722, 1995.

Fuselier, S. A., B. J. Anderson, and T. G. Onsager, Electron and ion signatures of field line topology at the low-shear magnetopause, *J. Geophys. Res.*, *102*, 4847--4864, doi:10.1029/96JA03635, 1997.

Gosling, J. T., D. N. Baker, S. J. Bame, W. C. Feldman, R. D. Zwickl, and E. J. Smith, Bidirectional solar wind electron heat flux events, *J. Geophys. Res.*, *92*(A8), 8519, doi:10.1029/JA092iA08p08519, 1987.

Gratton, F. T., L. E. Bilbao, C. J. Farrugia, and G. Gnavi, Large eddy simulations in MHD: The rise of counter-rotating vortices at the magnetopause, *J. Phys. Conf. Ser.*, *166*, 12,023, doi:10.1088/1742-6596/166/1/012023, 2009.

Grygorov, K., Z. Němeček, J. Šafránková, L. Přech, G. Pi, and J. H. Shue, Kelvin-Helmholtz wave at the subsolar magnetopause boundary layer under radial IMF, *J. Geophys. Res.*, *121*, 9863--9879, doi:10.1002/2016JA023068, 2016.

Guo, X. C., C. Wang, and Y. Q. Hu, Global MHD simulation of the Kelvin-Helmholtz instability at the magnetopause for northward interplanetary magnetic field, *J. Geophys. Res.*, *115*, A10,218, doi:10.1029/2009JA015193, 2010.

Gurgiolo, C., M. Goldstein, A.-F. Viñas, and A. Fazakerley, First measurements of electron vorticity in the foreshock and solar wind, *Ann. Geophys.*, *28*, 2187--2200, doi:10.5194/angeo-28-2187-2010, 2010.

Gurgiolo, C., M. L. Goldstein, A. F. Viñas, W. H. Matthaeus, and A. N. Fazakerley, Observations of electron vorticity in the inner plasma sheet, *Ann. Geophys.*, *29*, 1517--1527, doi:10.5194/angeo-29-1517-2011, 2011.

Haaland, S., et al., Four-spacecraft determination of magnetopause orientation, motion and thickness: comparison with results from single-spacecraft methods, *Ann. Geophys.*, *22*, 1347--1365, doi:10.5194/angeo-22-1347-2004, 2004.

Harvey, C., Spatial Gradients and the Volumetric Tensor, *ISSI Sci. Reports Ser.*, *1*, 307--322, 1998.

Hasegawa, A., *Plasma instabilities and nonlinear effects*, Springer, 1975.

Hasegawa, H., M. Fujimoto, T.-D. Phan, H. Rème, A. Balogh, M. W. Dunlop, C. Hashimoto, and R. TanDokoro, Transport of solar wind into Earth's magnetosphere through rolled-up Kelvin-Helmholtz vortices, *Nature*, *430*, 755--758, 2004.

Hasegawa, H., M. Fujimoto, K. Takagi, Y. Saito, T. Mukai, and H. Rème, Single-spacecraft detection of rolled-up Kelvin-Helmholtz vortices at the flank magnetopause, *J. Geophys. Res.*, *111*(9), 1--10, doi:10.1029/2006JA011728, 2006.

Hasegawa, H., B. U. Ö. Sonnerup, C. J. Owen, B. Klecker, G. Paschmann, A. Balogh, and H. Rème, The structure of flux transfer events recovered from Cluster data, *Ann. Geophys.*, *24*, 603--618, doi:10.5194/angeo-24-603-2006, 2006.

Hasegawa, H., B. U. Ö. Sonnerup, M. Fujimoto, Y. Saito, and T. Mukai, Recovery of streamlines in the flank low-latitude boundary layer, *J. Geophys. Res.*, *112*(A4), doi:10.1029/2006JA012101, 2007.

Hasegawa, H., et al., Kelvin-Helmholtz waves at the Earth's magnetopause: Multiscale development and associated reconnection, *J. Geophys. Res.*, *114*, 12,207, 2009.

Hillier, A., and V. Polito, Observations of the Kelvin–Helmholtz Instability Driven by Dynamic Motions in a Solar Prominence, *Astrophys. J. Lett.*, *864*, L10, doi:10.3847/2041-8213/aad9a5, 2018.

Hones, E. W., J. Birn, S. J. Bame, J. R. Asbridge, G. Paschmann, N. Sckopke, and G. Haerendel, Further determination of the characteristics of magnetospheric plasma vortices with Isee 1 and 2, *J. Geophys. Res.*, *86*, 814--820, doi:10.1029/JA086iA02p00814, 1981.

Horton, W., J. C. Perez, T. Carter, and R. Bengtson, Vorticity probes and the characterization of vortices in the Kelvin--Helmholtz instability in the large plasma device experiment, *Phys. Plasmas*, *12*(2), 22,303--22,308, doi:10.1063/1.1830489, 2005.

Huang, C., Q. Lu, F. Guo, M. Wu, A. Du, and S. Wang, Magnetic islands formed due to the Kelvin-Helmholtz instability in the outflow region of collisionless magnetic reconnection, *Geophys. Res. Lett.*, *42*, 7282--7286, doi:10.1002/2015GL065690, 2015.

Huba, J. D., Hall dynamics of the Kelvin-Helmholtz instability, *Phys. Rev. Lett.*, *72*(13), 2033--2036, 1994.

Huba, J. D., The Kelvin-Helmholtz instability: Finite Larmor radius magnetohydrodynamics, *Geophys. Res. Lett.*, *23*(21), 2907--2910, doi:10.1029/96GL02767, 1996.

Hughes, D. W., and S. M. Tobias, On the instability of magnetohydrodynamic shear flows, *Proceedings of the Royal Society of London Series A*, *457*(2010), 1365, doi:10.1098/rspa.2000.0725, 2001.

Hwang, K. J., M. M. Kuznetsova, F. Sahraoui, M. L. Goldstein, E. Lee, and G. K. Parks, Kelvin-Helmholtz waves under southward interplanetary magnetic field, *J. Geophys. Res.*, *116*, A08210, doi:10.1029/2011JA016596, 2011.

Hwang, K. J., M. L. Goldstein, M. M. Kuznetsova, Y. Wang, A. F. ViñAs, and D. G. Sibeck, The first in situ observation of Kelvin-Helmholtz waves

at high-latitude magnetopause during strongly dawnward interplanetary magnetic field conditions, *J. Geophys. Res.*, *117*, A08233, doi: 10.1029/2011JA017256, 2012.

Hwang, K. J., et al., The substructure of a flux transfer event observed by the MMS spacecraft, *Geophys. Res. Lett.*, *43*(18), 9434--9443, doi:10.1002/2016GL070934, 2016.

Ieda, A., S. Machida, T. Mukai, Y. Saito, T. Yamamoto, A. Nishida, and T. Terasawa, Statistical analysis of the plasmoid evolution with Geotail observations, *J. Geophys. Res.*, *103*, 4453--4465, doi:10.1029/9, 1998.

Jacobs, J. A., Y. Kato, S. Matsushita, and V. A. Troitskaya, Classification of Geomagnetic Micropulsations, *Journal of Geophysical Research*, *69*(1), 180--181, doi:10.1029/JZ069i001p00180, 1964.

Jones, T. W., J. B. Gaalaas, D. Ryu, and A. Frank, The MHD Kelvin□Helmholtz Instability. II. The Roles of Weak and Oblique Fields in Planar Flows, *The Astrophysical Journal*, *482*(1), 230--244, doi:10.1086/304145, 1997.

Karimabadi, H., et al., Coherent structures, intermittent turbulence, and dissipation in high-temperature plasmas, *Physics of Plasmas*, *20*(1), 012303, doi:10.1063/1.4773205, 2013.

Kavosi, S., and J. Raeder, Ubiquity of Kelvin-Helmholtz waves at Earth's magnetopause, *Nat. Commun.*, *6*, 7019, doi:10.1038/ncomms8019, 2015.

Kieokaew, R., and C. Foullon, Kelvin-helmholtz waves magnetic curvature and vorticity: Four-spacecraft cluster observations, *Journal of Geophysical Research (Space Physics)*, *124*, 3347-- 3359, 2019.

Kieokaew, R., C. Foullon, and B. Lavraud, Four-Spacecraft Magnetic Curvature and Vorticity Analyses on Kelvin-Helmholtz Waves in MHD Simulations, *J. Geophys. Res.*, *123*, 513--529, doi:10.1002/2017JA024424, 2018a.

Kieokaew, R., C. Foullon, and B. Lavraud, Four-Spacecraft Magnetic Curvature Analysis on Kelvin-Helmholtz Waves in MHD Simulations, in *Space Weather of the Heliosphere: Processes and Forecasts*, *IAU Symposium*, vol. 335, edited by C. Foullon and O. E. Malandraki, pp. 132--134, doi: 10.1017/S1743921318000522, 2018b.

Knetter, T., F. M. Neubauer, T. Horbury, and A. Balogh, Four-point discontinuity observations using Cluster magnetic field data: A statistical survey, *J. Geophys. Res.*, *109*(A6), 1--12, doi:10.1029/2003JA010099, 2004.

Knoll, D. A., and L. Chacón, Magnetic Reconnection in the Two-Dimensional Kelvin-Helmholtz Instability, *Phys. Rev. Lett.*, *88*, 215003, doi:10.1103/PhysRevLett.88.215003, 2002.

Lavraud, B., M. F. Thomsen, M. G. G. T. Taylor, Y. L. Wang, T. D. Phan, S. J. Schwartz, R. C. Elphic, A. Fazakerley, and H. Re, Characteristics of the magnetosheath electron boundary layer under northward interplanetary magnetic field : Implications for high-latitude reconnection, *J. Geophys. Res.*, *110*, 1--9, doi:10.1029/2004JA010808, 2005.

Lavraud, B., M. F. Thomsen, B. Lefebvre, S. J. Schwartz, K. Seki, T. D. Phan, Y. L. Wang, A. Fazakerley, and H. Re, Evidence for newly closed magnetosheath field lines at the dayside magnetopause under northward IMF, *J. Geophys. Res.*, *111*, A05,211, doi:10.1029/2005JA011266, 2006.

Lavraud, B., et al., Currents and associated electron scattering and bouncing near the diffusion region at Earth's magnetopause, *Geophys. Res. Lett.*, *43*(7), 3042--3050, doi:10.1002/2016GL068359, 2016.

Lee, L. C., and Z. F. Fu, A theory of magnetic flux transfer at the Earth's magnetopause, *Geophys. Res. Lett.*, *12*, 105--108, doi:10.1029/GL012i002p00105, 1985.

Leroy, M. H. J., and R. Keppens, On the influence of environmental parameters on mixing and reconnection caused by the Kelvin-Helmholtz instability at the magnetopause, *Phys. Plasmas*, *24*, 012,906, doi:10.1063/1.4974758, 2017.

Li, W. Y., X. C. Guo, and C. Wang, Spatial distribution of Kelvin-Helmholtz instability at low-latitude boundary layer under different solar wind speed conditions, *J. Geophys. Res.*, *117*(8), 1--11, doi:10.1029/2012JA017780, 2012.

Lin, D., C. Wang, W. Li, B. Tang, X. Guo, and Z. Peng, Properties of Kelvin-Helmholtz waves at the magnetopause under northward interplanetary magnetic field: Statistical study, *J. Geophys. Res.*, *119*, 7485--7494, 2014.

Lockwood, M., S. W. H. Cowley, M. F. Smith, R. P. Rijnbeek, and R. C. Elphic, The contribution of flux transfer events to convection, *Geophys. Res. Lett.*, *22*, 1185--1188, doi:10.1029/95GL01008, 1995.

Ma, X., P. Delamere, A. Otto, and B. Burkholder, Plasma transport driven by the three-dimensional Kelvin-Helmholtz instability, *J. Geophys. Res.*, *122*(10), 10,382--10,395, doi:10.1002/2017JA024394, 2017.

Malagoli, A., G. Bodo, and R. Rosner, On the nonlinear evolution of magneto-hydrodynamic Kelvin-Helmholtz instabilities, *The Astrophysical Journal*, *456*, 708--716, 1996.

Masson, A., and K. Nykyri, Kelvin-Helmholtz Instability: Lessons Learned and Ways Forward, *Sp. Sci. Rev.*, pp. 1--18, doi: 10.1007/s11214-018-0505-6, 2018.

Masters, A., et al., Cassini observations of a Kelvin-Helmholtz vortex in Saturn's outer magnetosphere, *J. Geophys. Res.*, *115*, A07225, doi:10.1029/2010JA015351, 2010.

Matsumoto, Y., and M. Hoshino, Onset of turbulence induced by a Kelvin-Helmholtz vortex, *Geophys. Res. Lett.*, *31*(2), 1--4, doi:10.1029/2003GL018195, 2004.

Matthaeus, W. H., Reconnection in two dimensions: localization of vorticity and current near magnetic X-points, *Geophys. Res. Lett.*, *9*(6), 660--663, 1982.

Matthaeus, W. H., and S. L. Lamkin, Turbulent magnetic reconnection, *The Physics of Fluids*, *29*(8), 2513--2534, doi:10.1063/1.866004, 1986.

Mills, K. J., A. W. Longbottom, A. N. Wright, and M. S. Ruderman, Kelvin-Helmholtz instability on the magnetospheric flanks: An absolute and convective instability approach, *Journal of Geophysical Research*, *105*(A12), 27,685--27,700, doi:10.1029/1999JA000289, 2000.

Mitchell, D. G., F. Kutchko, D. J. Williams, T. E. Eastman, L. A. Frank, and C. T. Russell, An extended study of the low-latitude boundary layer on the dawn and dusk flanks of the magnetosphere, *J. Geophys. Res.*, *92*, 7394--7404, doi:10.1029/JA092iA07p07394, 1987.

Miura, A., Anomalous transport by magnetohydrodynamic Kelvin-Helmholtz instabilities in the solar wind-magnetosphere interaction, *J. Geophys. Res.*, *89*(A2), 801, doi:10.1029/JA089iA02p00801, 1984.

Miura, A., Simulation of Kelvin-Helmholtz instability at the magnetopsheric boundary, *J. Geophys. Res.*, *92*(A4), 3195--3206, doi:10.1029/JA089iA02p00801, 1987.

Miura, A., Self-organization in the two-dimensional magnetohydrodynamic transverse Kelvin-Helmholtz instability, *J. Geophys. Res.*, *104*(A1), 395, doi: 10.1029/98JA02530, 1999.

Miura, A., and P. L. Pritchett, Nonlocal stability analysis of the MHD Kelvin-Helmholtz instability in a compressible plasma, *J. Geophys. Res.*, *87*(A9), 7431, doi:10.1029/JA087iA09p07431, 1982.

Moore, T. W., K. Nykyri, and A. P. Dimmock, Cross-scale energy transport in space plasmas, *Nat. Phys.*, *12*, 1164--1169, doi:10.1038/NPHYS3869, 2016.

Mottez, F., and G. Chanteur, Surface crossing by a group of satellites: A theoretical study, *J. Geophys. Res.*, *99*, 13,499--13,508, doi:10.1029/93JA03326, 1994.

Nakamura, T. K., M. Fujimoto, and A. Otto, Structure of an MHD-scale Kelvin-Helmholtz vortex: Two-dimensional two-fluid simulations including finite electron inertial effects, *J. Geophys. Res.*, *113*(9), 1--16, doi:10.1029/2007JA012803, 2008.

Nakamura, T. K. M., and W. Daughton, Turbulent plasma transport across the Earth' s low-latitude boundary layer, *Geophys. Res. Lett.*, *41*, 8704--8712, doi:10.1002/2014GL061952.The, 2014.

Nakamura, T. K. M., and M. Fujimoto, Magnetic effects on the coalescence of Kelvin-Helmholtz vortices, *Phys. Rev. Lett.*, *101*(16), 1--4, doi:10.1103/PhysRevLett.101.165002, 2008.

Nakamura, T. K. M., D. Hayashi, M. Fujimoto, and I. Shinohara, Decay of MHD-scale Kelvin-Helmholtz vortices mediated by parasitic electron dynamics, *Phys. Rev. Lett.*, *92*(14), 145,001--1, doi:10.1103/PhysRevLett.92.145001, 2004.

Nakamura, T. K. M., M. Fujimoto, and A. Otto, Magnetic reconnection induced by weak Kelvin-Helmholtz instability and the formation of the low-latitude boundary layer, *Geophys. Res. Lett.*, *33*, L14106, doi:10.1029/2006GL026318, 2006.

Nakamura, T. K. M., I. Hasegawa, H. Shinohara, and M. Fujimoto, Evolution of an MHD-scale Kelvin-Helmholtz vortex accompanied by magnetic reconnection: Two-dimensional particle simulations, *J. Geophys. Res.*, *116*(3), 1--18, doi:10.1029/2010JA016046, 2011.

Nakamura, T. K. M., W. Daughton, H. Karimabadi, and S. Eriksson, Three-dimensional dynamics of vortex-induced reconnection and comparison with THEMIS observations, *J. Geophys. Res.*, *118*, 5742--5757, doi:10.1002/jgra.50547, 2013.

Nakamura, T. K. M., S. Eriksson, H. Hasegawa, S. Zenitani, W. Y. Li, K. J. Genestreti, R. Nakamura, and W. Daughton, Mass and Energy Transfer Across the Earth's Magnetopause Caused by Vortex-Induced Reconnection, *J. Geophys. Res.*, *122*(11), 11,505--11,522, doi:10.1002/2017JA024346, 2017.

National Research Council, *The Sun to the Earth -- and Beyond: A Decadal Research Strategy in Solar and Space Physics*, The National Academies Press, Washington, DC, doi:10.17226/10477, 2003.

Nishino, M. N., M. Fujimoto, G. Ueno, T. Mukai, and Y. Saito, Origin of temperature anisotropies in the cold plasma sheet: Geotail observations around the Kelvin-Helmholtz vortices, *Ann. Geophys.*, *25*(9), 2069--2086, doi:10.5194/angeo-25-2069-2007, 2007.

Nykyri, K., and A. Otto, Plasma transport at the magnetospheric boundary due to reconnection in Kelvin-Helmholtz vortices, *Geophys. Res. Lett.*, *28*, 3565--3568, doi:10.1029/2001GL013239, 2001.

Nykyri, K., and A. Otto, Plasma transport at the magnetospheric boundary due to reconnection in Kelvin-Helmholtz vortices, *Geophys. Res. Lett.*, *28*(18), 3565--3568, 2001.

Nykyri, K., A. Otto, B. Lavraud, C. Mouikis, L. M. Kistler, A. Balogh, and H. Rème, Cluster observations of reconnection due to the Kelvin-Helmholtz instability at the dawnside magnetospheric flank, *Ann. Geophys.*, *24*, 2619--2643, 2006.

Ogilvie, K. W., R. J. Fitzenreiter, and J. D. Scudder, Observations of electron beams in the low-latitude boundary layer, *J. Geophys. Res.*, *89*, 10,723--10,732, doi:10.1029/JA089iA12p10723, 1984.

Ong, R. S. B., and N. Roderick, On the Kelvin-Helmholtz instability of the Earth's magnetopause, *Planet. Space Sci.*, *20*, 1--10, doi:10.1016/0032-0633(72)90135-3, 1972.

Onsager, T. G., J. D. Scudder, M. Lockwood, and C. T. Russell, Reconnection at the high-latitude magnetopause during northward interplanetary magnetic field conditions, *J. Geophys. Res.*, *106*(A11), 25,467--25,488, doi:10.1029/2000JA000444, 2001.

Otto, A., and D. H. Fairfield, Kelvin-Helmholtz instability at the magnetotail boundary: MHD simulation and comparison with Geotail observations, *J. Geophys. Res.*, *105*, 21, doi:10.1029/1999JA000312, 2000.

Owen, C. J., M. Taylor, I. C. Krauklis, A. N. Fazakerley, M. W. Dunlop, and J. M. Bosqued, Cluster observations of surface waves on the dawn flank magnetopause, *Ann. Geophys.*, *22*(3), 971--983, doi:10.5194/angeo-22-971-2004, 2004.

Owen, C. J., et al., Cluster PEACE observations of electrons during magnetospheric flux transfer events, *Ann. Geophys.*, *19*, 1509--1522, doi:10.5194/angeo-19-1509-2001, 2001.

Parashar, T. N., and W. H. Matthaeus, Propinquity of Current and Vortex Structures: Effects on Collisionless Plasma Heating, *Astrophys. J.*, *832*(1), 57, doi:10.3847/0004-637X/832/1/57, 2016.

Paschmann, G., G. Haerendel, I. Papamastorakis, N. Sckopke, S. J. Bame, J. T. Gosling, and C. T. Russell, Plasma and magnetic field characteristics of magnetic flux transfer events, *J. Geophys. Res.*, *87*(A4), 2159, doi:10.1029/JA087iA04p02159, 1982.

Paschmann, G., A. N. Fazakerley, and S. J. Schwartz, Moments of Plasma Velocity Distributions, *ISSI Scientific Reports Series*, *1*, 125--158, 1998.

Phan, T. D., et al., MMS observations of electron-scale filamentary currents in the reconnection exhaust and near the X line, *Geophys. Res. Lett.*, *43*(12), 6060--6069, doi:10.1002/2016GL069212, 2016.

Plaschke, F., M. G. G. T. Taylor, and R. Nakamura, Alternative interpretation of results from Kelvin-Helmholtz, *Geophys. Res. Lett.*, pp. 244--250, doi:10.1002/2013GL058948.Abstract, 2014.

Plaschke, F., et al., Steepening of waves at the duskside magnetopause, *Geophys. Res. Lett.*, *43*(14), 7373--7380, doi:10.1002/2016GL070003, 2016.

Pollock, C., et al., Fast Plasma Investigation for Magnetospheric Multiscale, *Space Sci. Rev.*, *199*, 331--406, doi:10.1007/s11214-016-0245-4, 2016.

Pu, Z.-Y., and M. G. Kivelson, Kelvin-Helmholtz Instability at the magnetopause: Solution for compressible plasmas, *J. Geophys. Res.*, *88*(A2), 841, doi:10.1029/JA088iA02p00841, 1983.

Pu, Z. Y., M. Yei, and Z. X. Liu, Generation of vortex-induced tearing mode instability at the magnetopause, *J. Geophys. Res.*, *95*, 10,559--10,566, doi:10.1029/JA095iA07p10559, 1990.

Raeder, J., Flux Transfer Events: 1. generation mechanism for strong southward IMF, *Ann. Geophys.*, *24*, 381--392, doi:10.5194/angeo-24-381-2006, 2006.

Retinò, A., Space plasmas: A journey through scales, *Nat. Phys.*, *12*(12), 1092--1093, doi:10.1038/nphys3976, 2016.

Rijnbeek, R. P., S. W. H. Cowley, D. J. Southwood, and C. T. Russell, A survey of dayside transfer events observed by ISEE 1 and 2 magnetometers, *J. Geophys. Res.*, *89*, 786--800, doi:10.1029/JA089iA02p00786, 1984.

Robert, P., M. W. Dunlop, A. Roux, and G. Chanteur, Accuracy of Current Density Determination, *ISSI Sci. Reports Ser.*, *1*, 395--418, 1998.

Robert, P., A. Roux, C. C. Harvey, M. W. Dunlop, P. W. Daly, and K.-H. Glassmeier, Tetrahedron Geometric Factors, *ISSI Sci. Reports Ser.*, *001*, 323--328, 1998.

Roelof, E. C., and D. G. Sibeck, Magnetopause shape as a bivariate function of interplanetary magnetic field B_z and solar wind dynamic pressure, *J. Geophys. Res.*, *98*, 21,421--21,450, doi:10.1029/93JA02362, 1993.

Rossi, C., Kelvin-Helmholtz Instability at the Magnetopause: Theory and Observations, Ph.D. thesis, Université Pierre et Marie Curie - Paris VI and Universitá Degli Studi Di Pisa, 2015.

Runov, A., R. Nakamura, and W. Baumjohann, Multi-point study of the magnetotail current sheet, *Adv. Sp. Res.*, *38*(1), 85--92, doi:10.1016/j.asr.2004.09.024, 2006.

Runov, A., et al., Current sheet structure near magnetic X-line observed by Cluster, *Geophys. Res. Lett.*, *30*(11), 10--13, doi:10.1029/2002GL016730, 2003.

Runov, A., et al., Electric current and magnetic field geometry in flapping magnetotail current sheets, *Ann. Geophys.*, *23*, 1391--1403, doi:10.5194/angeo-23-1391-2005, 2005.

Russell, C., and R. Elphic, Initial ISEE Magnetometer Results: Magnetopause Observations, *Space Sci. Rev.*, *22*, 681--715, 1978.

Russell, C. T., The dynamics of planetary magnetospheres, *Planet. Space Sci.*, *49*(10-11), 1005--1030, doi:10.1016/S0032-0633(01)00017-4, 2001.

Russell, C. T., and R. C. Elphic, ISEE observations of flux transfer events at the dayside magnetopause, *Geophys. Res. Lett.*, *6*, 33--36, doi:10.1029/GL006i001p00033, 1979.

Russell, C. T., M. M. Mellott, E. J. Smith, and J. H. King, Multiple spacecraft observations of interplanetary shocks: Four spacecraft determination of shock normals, *J. Geophys. Res.*, *88*, 4739--4748, doi:10.1029/JA088iA06p04739, 1983.

Russell, C. T., M. M. Mellott, E. J. Smith, and J. H. King, Multiple spacecraft observations of interplanetary shocks: Four spacecraft determination of shock normals, *J. Geophys. Res.*, *88*(A6), 4739--4748, doi:10.1029/JA088iA06p04739, 1983.

Russell, C. T., G. Le, and H. Kuo, The occurrence rate of flux transfer events, *Adv. Sp. Res.*, *18*(8), 197--205, doi:10.1016/0273-1177(95)00965-5, 1996.

Russell, C. T., et al., The Magnetospheric Multiscale Magnetometers, *Space Sci. Rev.*, *199*, 189--256, doi:10.1007/s11214-014-0057-3, 2016.

Ryu, D., T. W. Jones, and A. Frank, The Magnetohydrodynamic Kelvin-Helmholtz Instability: A Three-Dimensional Study of Nonlinear Evolution, *Astrophys. J.*, *10*(1996), 11, doi:10.1086/317789, 2000.

Sahraoui, F., G. Belmont, M. Goldstein, and L. Rezeau, Limitations of multispacecraft data techniques in measuring wave number spectra of space plasma turbulence, *J. Geophys. Res.*, *115*, A04,206, doi:10.1029/2009JA014724, 2010.

Schindler, K., On the role of irregularities in plasma entry into the magnetosphere, *J. Geophys. Res.*, *84*, 7257--7266, doi:10.1029/JA084iA12p07257, 1979.

Scholer, M., Magnetic flux transfer at the magnetopause based on single X line bursty reconnection, *Geophys. Res. Lett.*, *15*, 291--294, doi:10.1029/GL015i004p00291, 1988.

Schwartz, S. J., Shock and Discontinuity Normals, Mach Numbers, and Related Parameters, *ISSI Sci. Reports Ser.*, *1*, 249--270, 1998.

Sckopke, N., G. Paschmann, G. Haerendel, B. U. O. Sonnerup, S. J. Bame, T. G. Forbes, J. Hones, E. W., and C. T. Russell, Structure of the low-latitude boundary layer, *J. Geophys. Res.*, *86*, 2099--2110, doi:10.1029/JA086iA04p02099, 1981.

Shen, C., X. Li, M. Dunlop, Z. X. Liu, A. Balogh, D. N. Baker, M. Hapgood, and X. Wang, Analyses on the geometrical structure of magnetic field in the current sheet based on cluster measurements, *J. Geophys. Res.*, *108*(A5), doi:10.1029/2002JA009612, 2003.

Shen, C., X. Li, M. Dunlop, Q. Q. Shi, Z. X. Liu, E. Lucek, and Z. Q. Chen, Magnetic field rotation analysis and the applications, *J. Geophys. Res.*, *112*, A06,211, doi:10.1029/2005JA011584, 2007.

Shen, C., et al., Flattened current sheet and its evolution in substorms, *J. Geophys. Res.*, *113*(7), doi:10.1029/2007JA012812, 2008.

Shen, C., et al., Spatial gradients from irregular, multiple-point spacecraft configurations, *J. Geophys. Res.*, *117*(A11), n/a--n/a, doi:10.1029/2012JA018075, 2012.

Shen, C., et al., Direct calculation of the ring current distribution and magnetic structure seen by Cluster during geomagnetic storms, *J. Geophys. Res.*, *119*, 2458--2465, doi:10.1002/2013JA019460, 2014.

Shi, Q., C. Shen, Z. Pu, M. Dunlop, Q.-G. Zong, H. Zhang, C. Xiao, Z. Liu, and A. Balogh, Dimensional analysis of observed structures using multipoint magnetic field measurements: Application to Cluster, *Geophys. Res. Lett.*, *32*, L12,105, doi:10.1029/2005GL022454, 2005.

Shue, J.-H., J. K. Chao, H. C. Fu, C. T. Russell, P. Song, K. K. Khurana, and H. J. Singer, A new functional form to study the solar wind control of the magnetopause size and shape, *J. Geophys. Res.*, *102*(A5), 9497--9511, doi:10.1029/97JA00196, 1997.

Slavin, J. A., et al., Mercury's Magnetosphere After MESSENGER's First Flyby, *Science*, *321*, 85, doi:10.1126/science.1159040, 2008.

Song, P., and C. T. Russell, Model of the Formation of the Low-latitude Boundary Layer for Strongly Northward Interplanetary Magnetic Field, *J. Geophys. Res.*, *97*, 1411--1420, doi:10.1029/91JA02377, 1992.

Sonnerup, B. U. Ö. ., and W.-L. Teh, Reconstruction of two-dimensional coherent MHD structures in a space plasma: The theory, *J. Geophys. Res.*, *113*, A05202, doi:10.1029/2007JA012718, 2008.

Sonnerup, B. U. Ö., and L. J. Cahill, Magnetopause structure and attitude from Explorer 12 observations, *J. Geophys. Res.*, *72*(1), 171, doi:10.1029/JZ072i001p00171, 1967.

Sonnerup, B. U. Ö., and M. Scheible, Minimum and Maximum Variance Analysis, *ISSI Sci. Reports Ser.*, *1*, 185--220, 1998.

Sonnerup, B. U. Ö., H. Hasegawa, and G. Paschmann, Anatomy of a flux transfer event seen by Cluster, *Geophys. Res. Lett.*, *31*, L11803, doi:10.1029/2004GL020134, 2004.

Sonnerup, B. U. Ö., H. Hasegawa, W. L. Teh, and L. N. Hau, Grad-Shafranov reconstruction: An overview, *J. Geophys. Res.*, *111*(9), doi:10.1029/2006JA011717, 2006.

Sturner, A. P., et al., On Multiple Hall-Like Electron Currents and Tripolar Guide Magnetic Field Perturbations During Kelvin-Helmholtz Waves, *J. Geophys. Res.*, *123*(2), 1305--1324, doi:10.1002/2017JA024155, 2018.

Takagi, K., C. Hashimoto, H. Hasegawa, M. Fujimoto, and R. TanDokoro, Kelvin-Helmholtz instability in a magnetotail flank-like geometry: Three-dimensional MHD simulations, *J. Geophys. Res.*, *111*(8), 1--10, doi:10.1029/2006JA011631, 2006.

Talwar, S. P., Hydromagnetic Stability of the Magnetospheric Boundary, *J. Geophys. Res.*, *69*(13), 2707--2713, 1964.

Taylor, M., et al., Spatial distribution of rolled up Kelvin-Helmholtz vortices at Earth's dayside and flank magnetopause, *Ann. Geophys.*, *30*, 1025--1035, doi:10.5194/angeo-30-1025-2012, 2012.

Taylor, M. G. G. T., and B. Lavraud, Observation of three distinct ion populations at the Kelvin-Helmholtz-unstable magnetopause, *Ann. Geophys.*, *26*(6), 1559--1566, doi:10.5194/angeo-26-1559-2008, 2008.

Terasawa, T., M. Fujimoto, H. Karimabadi, and N. Omidi, Anomalous Ion Mixing within a Kelvin-Helmholtz Vortex in a Collisionless Plasma, *Phys. Rev. Lett.*, *68*(18), 2778--2781, 1992.

Terasawa, T., et al., Solar wind control of density and temperature in the near-Earth plasma sheet: WIND/GEOTAIL collaboration, *Geophys. Res. Lett.*, *24*, 935--938, doi:10.1029/96GL04018, 1997.

Thomas, V. A., and D. Winske, Kinetic Simulations of the Kelvin-Helmholtz Instability at the Magnetopause, *J. Geophys. Res.*, *98*(A7), 11,425--11,438, doi:Doi10.1029/93ja00604, 1993.

Treumann, R. A., J. Labelle, and T. M. Bauer, Diffusion Processes: An Observational Perspective, *Washington DC American Geophysical Union Geophysical Monograph Series*, *90*, 331, doi:10.1029/GM090p0331, 1995.

Vernisse, Y., et al., Signatures of complex magnetic topologies from multiple reconnection sites induced by Kelvin-Helmholtz instability, *J. Geophys. Res.*, *121*(10), 9926--9939, doi:10.1002/2016JA023051, 2016.

Vines, S. K., S. A. Fuselier, S. M. Petrinec, K. J. Trattner, and R. C. Allen, Occurrence frequency and location of magnetic islands at the dayside

magnetopause, *J. Geophys. Res.*, *122*(4), 4138--4155, doi:10.1002/2016JA023524, 2017.

Vogt, J., and G. Paschmann, Accuracy of Plasma Moment Derivatives, *ISSI Sci. Reports Ser.*, *001*, 419--448, 1998.

Vogt, J., G. Paschmann, and G. Chanteur, Reciprocal Vectors, *ISSI Sci. Reports Ser.*, *8*, 33--46, 2008.

Vogt, J., S. Haaland, and G. Paschmann, Accuracy of multi-point boundary crossing time analysis, *Ann. Geophys.*, *29*(12), 2239--2252, doi:10.5194/angeo-29-2239-2011, 2011.

Volpp, J., and D. Sieg, ESOC Data Products in the CAA, *Astrophysics and Space Science Proceedings*, *11*, 209--222, doi:10.1007/978-90-481-3499-1_13, 2010.

Wang, R., Q. Lu, A. Du, and S. Wang, In situ observations of a secondary magnetic island in an ion diffusion region and associated energetic electrons, *Phys. Rev. Lett.*, *104*(17), 2--5, doi:10.1103/PhysRevLett.104.175003, 2010a.

Wang, R., Q. Lu, X. Li, C. Huang, and S. Wang, Observations of energetic electrons up to 200 keV associated with a secondary island near the center of an ion diffusion region: A Cluster case study, *J. Geophys. Res.*, *115*(11), 1--10, doi:10.1029/2010JA015473, 2010b.

Wu, C. C., Kelvin-Helmholtz Instability at the Magnetopause Boundary, *J. Geophys. Res.*, *91*(A3), 3042--3060, doi:10.1029/JA091iA03p03042, 1986.

Yang, Y. Y., et al., The force-free configuration of flux ropes in geomagnetotail: Cluster observations, *J. Geophys. Res.*, *119*(8), 6327--6341, doi:10.1002/2013JA019642, 2014.

Zhang, Y. C., et al., Two different types of plasmoids in the plasma sheet: Cluster multisatellite analysis application, *J. Geophys. Res.*, *118*(9), 5437--5444, doi:10.1002/jgra.50542, 2013.

Zhang, Y. C., et al., First in situ evidence of electron pitch angle scattering due to magnetic field line curvature in the ion diffusion region, *J. Geophys. Res.*, pp. 4103--4110, doi:10.1002/2016JA022409.Received, 2016.

Zhou, X.-Z., Q.-G. Zong, J. Wang, Z. Y. Pu, X. G. Zhang, Q. Q. Shi, and J. B. Cao, Multiple triangulation analysis: application to determine the velocity of 2-D structures, *Ann. Geophys.*, *24*, 3173--3177, doi:10.5194/angeo-24-3173-2006, 2006.